Effect of trailing edge shape on the flow characteristics around an airfoil at low Reynolds number

Nikitas Thomareis

Department of Aeronautics
Imperial College London

November 2017

Supervised by:
Dr. George Papadakis
Prof. Christos Vassilicos

This thesis is submitted for the degree of Doctor of Philosophy and the Diploma of Imperial College London

Abstract

DNS of the flow field around a NACA 0012 airfoil at $Re_C = 50,000$ and angle of attack 5^o with 3 different trailing edge shapes (straight, blunt and serrated) have been performed. Initially the time-averaged flow characteristics of the 3 trailing edges are studied. The presence of serrations in the trailing edge is found to create a spanwise pressure gradient, which is responsible for the development of a secondary flow pattern in the spanwise direction, and for the reduction of the wake deficit downstream of the troughs. The dominant flow structures and their frequencies are investigated for the straight and blunt trailing edges, using the Dynamic Mode Decomposition method (DMD) and resolvent analysis. Using these techniques we are able to identify and analyse the interactions between the modes which characterize the dynamic behaviour of the flow field. It is shown that for the straight trailing edge airfoil, the DMD can capture the fundamental as well as the subharmonic of the Kelvin-Helmholtz instability that develops naturally in the separating shear layer. The blunt trailing edge results in periodic vortex shedding, with frequency close to the subharmonic of the natural shear layer frequency, which is found to have an upstream effect and force the separating shear layer into a lock-in state. A set of optimal responses, calculated to maximize the energy of the response, were used to accurately estimate the spectra in the most energetic points in the flow field. Lastly, a tripping method is applied which keeps the boundary layer attached. The pressure and skin-friction coefficients as well as the boundary layer profiles were significantly modified. Furthermore, the selection of the domain used to optimise the response, used in the resolvent analysis, was found to have an important effect on the determination of the optimal modes.

Acknowledgements

I would like to thank my supervisors Dr. George Papadakis and Prof. Christos Vassilicos for their supervision and guidance provided throughout the course of my work.

I would also like to gratefully acknowledge the support of the EU Commission for the funding of this project under the ITN Marie Curie framework (MULTISOLVE Project, Grant Agreement No. 317269) as well as the UK Turbulence Consortium for their support in providing precious simulation time in the high performance computing facility Archer (UKTC Grant No. EP/L000261/1).

On a personal level I would like to thank my friends and my colleagues for their help and support during the years of my PhD studies. Lastly, I want to wholeheartedly thank my parents without the support of whom it would not have been possible to even start this endeavour.

Declaration

I hereby declare that all the work in this thesis is my own. All other sources of information used in this work have been fully acknowledged.

The copy right of this thesis rests with the author and is made available under a Creative Commons Attribution Non-Commercial No Derivatives licence. Researchers are free to copy, distribute or transmit the thesis on the condition that they attribute it, that they do not use it for commercial purposes and that they do not alter, transform or build upon it. For any reuse or redistribution, researchers must make clear to others the licence terms of this work

.

Nikitas Thomareis

Contents

1 Introduction **18**

1.1 Trailing edge modifications 18

1.2 Numerical studies 20

1.3 Stability studies of the laminar separation bubble 23

1.4 Dynamic mode decomposition 26

1.5 Resolvent analysis 30

1.6 Current Study 32

2 Numerical methodology and validation **35**

2.1 Introduction 35

2.2 Governing equations and their solution 35

2.2.1 Discretisation of the generic transport equation 36

2.2.2 Treatment of the pressure term 41

2.2.3 Pressure-velocity coupling 43

2.2.4 Boundary conditions 46

2.3 Numerical methods for the computation of eigenvalues 48

2.4 Meshing and validation 51

2.4.1 Geometrical details of the simulations 51

2.4.2 Computational domain and discretisation 52

2.4.3 Mesh convergence and validation study 53

3 Interaction between the flow field and the trailing edges 61

3.1 Introduction . . . 61

3.1.1 Derivation of the Dynamic Mode Decomposition formulas . . . 62

3.2 Results and discussion . . . 65

3.2.1 Airfoil with straight trailing edge . . . 65

3.2.2 Airfoil with blunt trailing edge . . . 70

3.2.3 Airfoil with serrated trailing edge . . . 78

3.3 Conclusions . . . 90

4 Resolvent analysis of the flow around the airfoil 91

4.1 Introduction . . . 91

4.2 Straight trailing edge airfoil results . . . 98

4.2.1 Spectrum of the resolvent operator . . . 98

4.2.2 Optimal modes . . . 101

4.3 Blunt trailing edge airfoil results . . . 109

4.3.1 Spectrum of the resolvent operator . . . 109

4.3.2 Optimal modes . . . 110

4.4 Estimation of velocity spectra based on point measurements. . . . 115

4.5 Conclusions . . . 124

5 Analysis of the attached boundary layer on the airfoil. 126

5.1 Introduction . . . 126

5.1.1 Numerical details of the tripping method . . . 127

5.2 Time-averaged velocity fields . . . 129

5.3 Resolvent analysis - Straight Trailing Edge . . . 144

5.3.1 Resolvent modes . . . 145

5.4 Resolvent analysis - Blunt Trailing Edge . . . 150

5.4.1 Resolvent modes . . . 152

5.5 Conclusions . . . 154

6 Conclusions **156**

6.1 Major findings 157

6.1.1 The flow-field around the airfoils 157

6.1.2 Frequency content of the flow fields 158

6.1.3 Spatial behaviour of the dominant modes 159

6.1.4 Resolvent analysis 160

6.1.5 Analysis of the attached boundary layer 161

6.2 Suggestions for future studies 162

List of Figures

2.1 Geometry of two cells adjacent to face f. 38

2.2 Topology of two adjacent non-orthogonal cells. 39

2.3 A uniform 1D CV arrangement. 42

2.4 Example of the treatment of periodic boundaries. 48

2.5 Serrated trailing edge airfoil geometry (2.5a) and characteristic dimensions (2.5b). 51

2.6 Domain topology used in the simulations. 52

2.7 Close up of the mesh at the vincinity of the leading edge). 53

2.8 Contour plots of the the ratio of the characteristic grid size to the local Kolmogorov scale. 55

2.9 Spanwise autocorrelation functions for the straight and blunt trailing edge airfoils. The first point is in the separation bubble, the 2^{nd} and 3^{rd} points are in the reattached turbulent boundary layer and the last points is in the very near wake. The cross stream coordinates of the points are for clarity mentioned here: for Figure 2.9a $Y/C = 0.038, 0.00037, -0.031, -0.075$ and for Figure 2.9b $Y/C = 0.025, -0.019, -0.041, -0.062$ going from the first to last point. 57

2.10 Comparison between the current results for C_p and C_f coefficients and the DNS results from Lehmkuhl et al.Lehmkuhl et al. (2013a) . 57

2.11 Comparison of profiles across the boundary layer. 59

2.12 Q contours in the range $[20, 100] \times (U_\infty/C)^2$ for the straight trailing edge case. The colorscale values are based on the streamwise velocity. 60

3.1 Amplitude distribution of the eigenvalues calculated from the DMD algorithm. 66

3.2 Power spectral density of the cross stream velocity component V at two different locations, $X/C = 0.53C, Y/C = 0.032$ (a) and $X/C = 2.0C, Y/C = -0.17$ (b). 67

3.3 Time-averaged streamwise velocity field (Figure 3.3a) and two most dominant DMD modes for a straight trailing edge (Figures 3.3b and 3.3c). 67

3.4 Streamwise, cross-stream and spanwise Reynolds stress distributions for the straight and blunt trailing edge airfoils. 69

3.5 DMD spectrum of the flow field around the blunt trailing edge airfoil. 71

3.6 Contour plots of the time-averaged velocity field U/U_∞ (3.6a) and the most dominant flow mode (3.6b) at $f_{bl,1}$. 71

3.7 Comparison of the pressure coefficients for the straight and blunt trailing edge cases. 72

3.8 Spectra for the blunt trailing edge airfoil for different cross stream ($Y/C\big[-0.3, 0.1\big]$) and streamwise ($X/C = 1.05,\ 1.4,\ 2.0$) locations. 74

3.9 Cross stream velocity spectra for 6 different locations (indicated with black dots in Figure 3.10b)at the suction side boundary layer, starting from $X/C = 0.47$ up to $X/C = 0.87$. 75

3.10 DMD spectrum (3.10a) and spatial structure of the mode at $f_{bl,1}$ (3.10b) at the plane capturing the shear layer transition and reattachment. The cross-stream component of the mode is plotted. 76

3.11 Time-average streamwise flow fields through the peak and trough planes. 78

3.12 Streamwise velocity profile at 4 different positions located at distance ΔX downstream of the trailing edge (ΔX is measured locally along the X direction from the trough and the peak spanwise locations). . . 80

3.13 Pressure distributions on the airfoil surface and inside the troughs. . . 81

3.14 (a) Spanwise velocity component (W) along the span (pressure side of the airfoil, at distance $0.05C$ upstream of the trailing edge trough). The dashed lines indicate the positions where $W = 0$. (b) Time-averaged streamlines at the pressure side of the airfoil. 82

3.15 Drawing of the flow behaviour inside a serration. The red blob corresponds to the low pressure core forming directly downstream of the trough. 83

3.16 Time averaged streamlines, color-coded with the streamwise velocity U/U_∞. 84

3.17 Probing lines and their corresponding spanwise locations after the trough (a), the mid point (b) and the peak (c). 84

3.18 Power spectra of V velocity component for different cross-stream locations, extending from $Y = -0.3C$ to $Y = 0.1C$. Left column data are probed very close to the trailing edge peak ($X = 1.05C$), while right column data are probed at $X = 1.40C$. From top to bottom, the probing lines are aligned with the trough, the mid-point and the peak of the serrations. 85

3.19 PSD of the cross velocity component at four streamwise locations at the suction side of the airfoil at $Z/C = 0.266$ (plane through the peak). Figure 3.19b has zoomed in the region $E_{vv} \leq 0.01$ for better illustration of the signals at $X/C = 0.47$ and $X/C = 0.858$. 86

3.20 Streamwise, cross-stream and spanwise Reynolds stress distributions for the serrated trailing edge airfoil at a spanwise plane through a peak (Figures 3.20a, 3.20c and 3.20e) and through a trough (Figures 3.20b, 3.20d and 3.20f). 89

4.1 Schematic of the resolvent operator system. 93

4.2 Singular values plot of the resolvent operator. The first 5 singular values ($s.v.$) of the operator are plotted against the angular frequency ω. 98

4.3 Spectrum of the linearized Navier-Stokes operator for the straight trailing edge case. 102

4.4 Streamwise component of the optimal forcing $\hat{f}_x$ and response $\hat{u}_x$ at the frequency ω_P with the highest amplification rate. The inset in Figure 4.4a shows in detail the structure of the mode close to the leading edge of the airfoil. 103

4.5 Cross-stream component of the optimal forcing $\hat{f}_y$ and response $\hat{u}_y$ at the frequency ω_P with the highest amplification rate. The inset in Figure 4.5a shows in detail the structure of the mode close to the leading edge of the airfoil. 104

4.6 Streamwise component of the optimal forcing $\hat{f}_x$ at the leading edge with the displacement thickness of the boundary layer overlapped. . . 104

4.7 Spatial structure of the eigenmode corresponding to the most unstable eigenvalue in Figure 4.3 at $\omega = 48.46$. 105

4.8 Cross-stream component of the optimal response at the suction side of the airfoil. The solid black lines shows the displacement thickness of the boundary layer while the solid brown line is the zero-streamwise mean velocity contour. 107

4.9 Absolute value of the maximum reverse flow (blue line-left axis) and velocities ratio R (red line-right axis), over the airfoil's suction side. . 107

4.10 Streamwise component of the optimal forcing $\hat{f}_x$ and response $\hat{u}_x$ at the wake shedding frequency that was calculated in chapter 3.3b. The inset in Figure 4.10a shows in detail the structure of the mode close to the leading edge of the airfoil. 108

4.11 Streamwise component of the optimal forcing $\hat{f}_x$ and response $\hat{u}_x$ at the low frequency peak shown in Figure 4.2. 109

4.12 Singular values plot of the resolvent operator for the blunt trailing edge airfoil. The first 5 singular values ($s.v.$) of the operator are shown. 110

4.13 Streamwise component of the optimal forcing $\hat{f}_x$ and response $\hat{u}_x$ at the frequency showing the vortex shedding frequency. 112

4.14 Cross-stream component of the optimal forcing $\hat{f}_y$ and response $\hat{u}_y$ at the frequency showing the vortex shedding frequency. 112

4.15 Cross-stream component of the optimal response at the suction side of the airfoil. The solid black lines shows the displacement thickness of the boundary layer while the solid brown line shows the zero streamwise velocity contour. 113

4.16 Absolute value of the maximum reverse flow and the velocities ratio over the airfoil's suction side. 113

4.17 Cross-stream component of the optimal response at the two annotated peaks P_L 4.17a and P_H 4.17b. 115

4.18 Resolvent spectra of the straight and blunt trailing edge cases. 116

4.19 PSD spectrum as calculated from the model (calibration at $X/C = 0.62, Y/C = 0.022$). 118

4.20 Spectrum estimate in the wake using two points for the estimation of the values of $\Psi(\omega)$. 120

4.21 Velocity fluctuations estimates for the straight trailing edge airfoil. . 121

4.22 PSD spectrum as calculated from the model (calibration at $X/C = 0.62, Y/C = 0.022$). 122

4.23 Velocity fluctuations estimates for the blunt trailing edge airfoil. . . 123

5.1 Temporal spectrum of the tripping forcing. The frequencies are normalized by the sampling frequency of the simulation (i.e. the inverse of the time-step). As can be seen the spectrum is constant until the user specified cut-off frequency $f_c = 0.2f_s$, which means that no additional/artifical modes are introduced in the flow field. 128

5.2 Ratio of the local characteristic cell size to the Kolmogorov length scale. 129

5.3 Mean streamwise velocity field for the untripped and tripped boundary layers for the straight and blunt trailing edge airfoils. 131

5.4 Boundary layer profiles at 5 different locations. The profiles have been normalized by the local maximum velocity at the edge of each profile U_0. 132

5.5 Lift and drag coefficients time series covering a period before and after the moment tripping is applied (red dashed line). 132

5.6 Streamwise (1^{st} row of figures) and cross-stream (2^{nd} row) fluctuations for the tripped (1^{st} column) and untripped (2^{nd} column) for the straight trailing edge airfoil. 133

5.7 Streamwise (1^{st} row of figures) and cross-stream (2^{nd} row) fluctuations for the tripped (1^{st} column) and untripped (2^{nd} column) for the blunt trailing edge airfoil. 134

5.8 Probability density function of C_f for the untripped (5.8a and 5.8c) and tripped (5.8b and 5.8d) airfoils. The solid line in each plot shows the mean value, while the dashed lines show the $\pm 1\sigma$ and $\pm 2\sigma$ ranges around the mean. The vertical dashed lines in Figures 5.8b and 5.8d indicate the range where the tripping was applied. 136

5.9 Tangential velocity profiles at the airfoil's surface (shown up to $Y/C = 0.01$) for the straight trailing edge case. The darker colours indicate a smaller X/C with $0.01 \leq X/C \leq 0.32$. The dashed blue arrow indicates increasing X/C. The exact locations are $X/C = 0.01, 0.02, 0.05, 0.1, 0.12, 0.14, 0.16, 0.18, 0.22, 0.24, 0.26, 0.28, 0.32$. 137

5.10 Tangential velocity profiles at the airfoil's surface (shown up to $Y/C = 0.01$) for the straight trailing edge case. The darker colours indicate a smaller X/C with $0.40 \leq X/C \leq 0.62$. The dashed blue arrow indicates increasing X/C. The exact locations are $X/C = 0.40, 0.44, 0.48, 0.50, 0.52, 0.54, 0.56, 0.58, 0.62$. 138

5.11 Probability density function of the pressure coefficient fluctuations for the untripped (5.11a and 5.11c) and tripped (5.11b and 5.11d) airfoils. 139

5.12 Instantaneous streamwise velocity field. The red curves delineate large scale structures. 141

5.13 Spanwise averaged spectrum of pressure on the suction side. 141

5.14 Spanwise averaged cross-correlation of the wall pressure on the airfoil's suction side. The reference signal is located at $X/C = 0.37$. . . 142

5.15 Cross-stream velocity spectra at two locations on the suction' side boundary layer. 143

5.16 Singular value plot of the resolvent operator for the tripped straight trailing edge airfoil. 145

5.17 Streamwise component of the optimal forcing and response at the frequency $\omega_{P,Trip}$ showing the highest amplification rate. 146

5.18 Cross-stream component of the optimal forcing and response at the frequency $\omega_{P,Trip}$ showing the highest amplification rate. 147

5.19 Streamwise (5.19a) and cross-stream (5.19b) components of the optimal response at the frequency $\omega_{2,Trip}$. 148

5.20 Streamwise (5.20a) and cross-stream (5.20b) components of the response at the frequency $\omega_{2,Trip}$ corresponding to the second singular value. 149
5.21 Optimization domain for the resolvent analysis focused on the suction side. 149
5.22 Resolvent spectra with different optimization domains Q_u. The grey lines correspond to the previous case where the optimisation was performed on the whole domain, while the coloured lines correspond to the current case where the optimisation covers only the suction side of the airfoil. 150
5.23 Cross-stream component of the optimal response at the frequency $\omega_{2,Trip}$ when the domain shown in Figure 5.21 is used in the optimization process. 150
5.24 Singular value plot of the resolvent operator for the blunt trailing edge airfoil. 151
5.25 Streamwise component of the optimal forcing $\hat{f}_x$ and response $\hat{u}_x$ at the frequency $\omega_{P,Blunt}$ showing the highest amplification rate. 152
5.26 Cross-stream component of the optimal forcing $\hat{f}_y$ and response $\hat{u}_y$ at the frequency $\omega_{P,Blunt}$ showing the highest amplification rate. 153
5.27 Streamwise 5.27a and cross-stream 5.27b components of the response $\hat{\boldsymbol{u}}$ at the peak frequency $\omega_{2,Blunt}$ corresponding to the second singular value. 154

Chapter 1

Introduction

1.1 Trailing edge modifications

Performance improvement of lifting devices has always been a challenge for the aerospace industry. Geometric modification of the wing section is one of the most common methods used to attain this goal. The absence of a complicated actuation mechanism has made passive control methods attractive, the most well known and widely used being the extendable flaps and slats employed since the first days of aviation. Since 1950s other methods have been studied, for example the truncation of the rear part of the wing to create a blunt trailing edge (Smith and Schaefer, 1950), leading to what is known as flatback profile. These early investigations showed the potential improvement of the maximum lift coefficient for the same flow conditions. More recent investigations have demonstrated additional benefits of the flatback airfoil, both experimentally and numerically (Standish and Van Dam, 2003; Baker et al., 2006; Xu et al., 2014), such as increased lift curve slope, optimized structural characteristics and decreased sensitivity to leading-edge transition. There benefits are important for low to medium Reynolds numbers applications, such as unmanned air vehicles or small wind turbines.

For small wind turbines in particular, blunt trailing edge airfoils offer significant advantages (Standish and Van Dam, 2003). The cyclic gravitational and aerody-

namic load results in large bending moments in the inboard region of the blades. This necessitates thick and structurally robust airfoil sections close to the hub, with thickeness to chord ratio larger than 25%. Thick airfoils with sharp trailing edges however have poor aerodynamic characteristics, while blunt trailing edges offer structural benefits without sacrificing the aerodynamic performance (Standish and Van Dam, 2003; Chow and van Dam, 2013).

The exposed blunt part of the airfoil however leads to increased pressure drag due to shedding. For wind turbines, increased drag is not such an important issue for the inboard region of the blade (Standish and Van Dam, 2003). Nevertheless, the benefits of blunt airfoils will increase if the penalty of increased drag can be mitigated. Biomimetics inspired several investigators to imitate the serrated geometries observed in animals such as whales or owls. Tanner (1970) used M-shaped serrations at the trailing edge of a blunt profile and found a decrease in the base pressure of up to 64% compared to the simple blunt trailing edge. Gai and Sharma (1981) found similar results with Tanner, and studied the effect of triangular serrations with angles of 60^o and 120^o, which were also shown to have positive effects. Rodriguez (1991) investigated the effect of squared serrations on a 2D body and found a reduction of up to 40% of the total drag, with an additional study of the longitudinal vortices in the near-wake of the body and their effect on the aerodynamics characteristics. A more recent work by Krentel and Nitsche (2013) on a truncated NACA 0012 airfoil using various geometrical patterns, showed a decrease in the drag by 29% for a specific Reynolds number (44,000). Another recent (experimental) study in this area by Nedić and Vassilicos (2015), has shown that the effect of serrated trailing edges can be further improved by adding a self-similar repeating (i.e. fractal) pattern in smaller scales. It was shown that the single scale triangular serrations reduced vortex shedding and improved the lift-to-drag ratio for higher angles of attack, and that the addition of a fractal multiscale pattern reduced even more the shedding energy without affecting the improved aerodynamic characteristics.

A thorough study on the flow physics behind a bluff body with a sinusoidal

trailing edge of constant thickness was made by Tombazis (1993). He found that the three-dimensional effects in the wake can reduce the correlation length of the base pressure, causing a decrease in the pressure drag. Further investigation of the wake of bodies with spanwise undulation (Bearman and Tombazis, 1993; Tombazis and Bearman, 1997) showed that the base pressure downstream of the blunt trailing edge, can be correlated with the frequencies of the vortex dislocations arising due to the spanwise inhomogeneity of the body. The aforementioned cases of bluff bodies with wavy trailing edges were also studied numerically with similar conclusions (Cai et al., 2008).

1.2 Numerical studies

Most of the investigations mentioned in the previous section are experimental. As already mentioned, airfoils with modified trailing edges are suitable for low to medium Reynolds number applications (approximately up to $200,000$ based on the airfoil's chord), for which DNS is feasible. An important characteristic in the aerodynamic behavior of airfoils at moderate Reynolds numbers is the laminar separation, which occurs shortly after the leading edge of the airfoil, giving rise to a highly complex and dynamic field (Lissaman, 1983). Most of the DNS studies of separating and transitional flows however have been performed on planar geometries (Alam and Sandham, 2000; Kotapati et al., 2010; Marxen and Rist, 2010; Rist and Augustin, 2006; Marxen et al., 2013; Marxen and Henningson, 2011; Postl et al., 2011; Spalart and Strelets, 2000). The adverse pressure gradient required for the formation of a laminar separation bubble (encountered in real airfoils) is reproduced by a suitable boundary condition at the upper boundary of the computational domain. Several of these studies are concerned with the control of the laminar separation.

Simulations with an actual airfoil geometry are more challenging and require curvilinear (or unstructured grids), but are more realistic as the pressure gradient that results from the interaction of the separation bubble with the potential flow

around the airfoil and the Kutta condition is part of the solution and not imposed externally. Until several years ago the number of DNS on airfoils was mostly limited to two-dimensional simulations or very low Reynolds numbers (and very often both). As we will see though, advances in computing have enabled the recent study of the full 3D flow field in the low to moderate Reynolds number regime. In the next paragraphs a brief overview of the past numerical studies on airfoils is given.

Bouhadji and Braza (2003) studied the two-dimensional flow field around a NACA 0012 airfoil at 0^o angle of attack. They used a compressible solver for simulations for constant $Re_C = 10000$ and variable Mach number up to $M = 0.98$, and constant Mach number $M = 0.85$ and variable Reynolds in the range $Re_C = 500$ to $Re_C = 10000$. The effect of varying the two numbers on the wake characteristics was studied, and the onset of the Kárman shedding was found to occur at $Re = 2070$. Bourdet et al. (2003) extended this study in three dimensions by introducing a spanwise perturbation, which led to the detection of oscillations in the spanwise velocity component, albeit without transition to turbulence. Similar flow configurations but at a higher angle of attack of 20^o were studied by Hoarau et al. (2003a) and Hoarau et al. (2003b). The range of Reynolds numbers again did not exceed $Re = 10000$. For $Re = 800$ a 3D case was studied with externally applied random perturbations and a spanwise undulation was observed similar to bluff body wakes, again though without full transition to turbulence. Tam and Ju (2006) increased the Reynolds number to $Re = 2 \times 10^5$ and investigated the flow around a NACA 0012, placed at 2^o incidence. A 2D compressible solver was also used in this case and the separated boundary layer on the suction side of the airfoil was studied in the context of acoustic noise generation.

Kitsios et al. (2006) studied the flow field of a NACA 0015 airfoil at Reynolds $Re = 3 \times 10^5$ and 18^o incidence. Both 2D DNS and 3D LES were performed, with the results showing a very good agreement with experimental PIV data. The objective of their paper was to study the effect of a zero-net-mass-flux actuator on the boundary layer and assess whether this actuation method can delay separation,

which indeed was found to be the case. Another study which also investigated the effect of separation control, was performed by You and Moin (2006). The airfoil used was again the NACA 0015, placed at 16.6^o angle of attack at the, unusually high, Reynolds number $Re_C = 8.96 \times 10^5$. A relatively small domain size ($6C \times 2.44C \times 0.2C$) and an implicit time scheme allowed for a simulation at reduced computational cost. Similarly to the results of Kitsios et al. (2006), You and Moin (2006) also showed that separation can be delayed using the appropriate control method, leading to an increase in the lift coefficient and to an overall improvement of the airfoil's performance.

Kotapati et al. (2010) performed two-dimensional simulations around a plate with an elliptic leading edge and a blunt trailing edge at 0^o angle of attack. The separation in this case was induced artificially by a blowing-suction boundary condition at the top boundary of the domain which caused a laminar separation bubble on the top surface of the airfoil. Various dynamic characteristics of the flow field were studied, such as the dominant frequencies in the different regions of the domain (the separated shear layer, the transitional region and the wake). Kotapati et al. (2010) distinguished 3 different flow scenarios based on the angle of attack and Reyonlds number of an airfoil. These are: attached flow at small angles of attack (case A), laminar separation, transition and reattachment (case B) and massively separated post-stall flow at high angles of attack (case C).

Shan et al. (2005a) performed DNS around a NACA 0012 at 4^o and chord based Reynolds number equal to 10^5. The authors captured the laminar separation, transition and reattachment of the shear layer (case B scenario according to Kotapati et al. (2010)). The shedding from the separated shear layer was attributed to the Kelvin-Helmholtz instability but no characteristic frequency was mentioned. Jones et al. (2008) investigated the effect of forcing on the behaviour of a laminar separation bubble for a NACA 0012 at Re=50,000 and Mach 0.4. This was a single frequency volume forcing term applied in a predefined region, with a spanwise variation. They found that forcing improves the aerodynamic performance, requiring

little energy input. Lehmkuhl et al. (2013a) investigated the capabilities of two sub-grid scale models (suitable for unstructured grids) for predicting the incompressible flow in transitional separating bubbles. A NACA 0012 airfoil with straight trailing edge was examined. DNS studies at $Re = 50,000$ were performed at two angles of attack, 5^o and 8^o, and used as reference to assess the performance of the sub-grid scale models. The DNS results are also used in the present thesis for comparison and validation purposes. Recently, implicit high-order LES at $Re_C = 270,000$ (Park et al., 2017) and DNS at $Re_C = 400,000$ (Hosseini et al., 2016) have been reported.

Simulations around airfoils with modified trailing edges are even more rare. Jones and Sandberg (2012) performed DNS simulations for a NACA 0012 with serrated trailing edge at the same Reynolds and Mach number as their previous investigation for a straight trailing edge (Jones et al., 2008). A serrated plate with very small and uniform bluntness (equal to 1.2×10^{-3} times the airfoil chord) was appended to the straight trailing edge. Although the main focus of their paper was the study of the acoustic behavior of the airfoil, the analysis of the flow field close to the trailing edge revealed the breakup of the large structures from the boundary layer as well as the creation of horseshoe vortices from the serrations. The same authors in another paper (Sandberg and Jones, 2011) found that the presence of this type of serrations does not change significantly the hydrodynamic field on the airfoil upstream of the trailing edge, including the behaviour of the laminar separation bubble.

1.3 Stability studies of the laminar separation bubble

As evidenced in the previous section, several numerical studies for airfoils at a range of Reynolds numbers and angles of attack have been performed. Such studies, thanks to the continuous improvement of the computational infrastructure available, have become increasingly detailed and realistic. Simulations can now be performed which can yield detailed information on the inherent dynamics of the flow field. A highly

potent field is the stability analysis of the flow field, which can give physical insight on the processes that dictate the evolution of perturbations and the subsequent transition to turbulence.

In the context of stability analysis, two fundamental concepts exist, which were introduced by Gaster (1963, 1968), namely the absolute and convective instability. In both cases a perturbation introduced at time $t = 0$ at location $x = 0$, will amplify as it propagates in the flow field. In the former type of instability, the perturbation will grow in both space and time, i.e. the perturbation signals both at $x = 0$ and in the upstream and downstream directions will experience an exponential growth after time T. In the latter type, the perturbation at $x = 0$ will eventually decay while it convects downstream (see Huerre and Monkewitz (1990) and references therein for an extensive review).

The shear layer, which forms an intrinsic part of any separation bubble, has been found to exhibit both types of instability depending on the flow conditions (see Huerre and Monkewitz (1985)). More specifically, it was shown that, depending on the velocity ratio $R = \frac{U_1 - U_2}{U_1 + U_2}$, where U_1 and U_2 are the velocities of the 2 streams that form the shear layer, it can either exhibit a convective or an absolute instability.

Stability studies of laminar separation bubbles in flat plate boundary layers have indeed corroborated this behaviour. Hammond and Redekopp (1998) and Rist and Maucher (2002) performed 1D local stability analysis using analytical profiles (the former used the Falker-Skan profile while the latter used modified hyperbolic tangent profiles) and both where able to observe an absolute instability depending on certain parameters such as the strength of the reversed flow in the bubble and the thickness of the separated region. In both studies a reverse flow of the order of approximately 30% was required in order to sustain an absolute instability. One of the most complete studies in the stability characteristics of separation bubbles is reported in the review paper by Dovgal et al. (1994). The separation bubbles forming in various different flow configurations are studied using 1D stability equations. A mechanism for the amplification of instabilities by the separation bubble is proposed, accord-

ing to which disturbances which are amplified by the shear layer are recirculated upstream,by the reverse flow, resulting in an inherent feedback mechanism.

Many of the studies mentioned in section 1.2 were also concerned in one way or another with linear stability analysis. More specifically, Alam and Sandham (2000) used profiles extracted from their DNS simulations to perform local stability analysis of the separation bubble. They found that a reverse flow of approximately $15 - 20\%$ is required for absolute instability to occur. In their simulations they observed reverse flow values of less than 8% and thus concluded that a convective instability was driving the turbulent transition. Similar results were reported by Spalart and Strelets (2000) and Allen and Riley (1995), who also suggested the presence of a convective instability mechanism due to the absence of a strong reverse flow. Rodríguez et al. (2013) found the minimum threshold for absolute instability to be 12%, identifying however that even at reverse flow levels of approximately 7% 3D effects can occur inside the separated region.

The response of a laminar separation bubble to imposed disturbances was studied by Marxen and Henningson (2011) and Marxen et al. (2013). The first paper focused on the sensitivity of the separation bubble to external perturbations, and on how several flow characteristics such as the mean flow and transition and reattachment locations can be significantly altered by externally imposed disturbances. The second paper went one step further and analysed the development of two-dimensional disturbances as these propagate through the separation bubble. Other studies such as these performed by Rist and Augustin (2006) and by Postl et al. (2011) focused more on the control aspects of the flow field and on how the length of the separation bubble can be modified using an external control strategy. In the paper by Rist and Augustin (2006), control was exerted in the form of a numerically simulated suction and blowing device located upstream of the separation point, while in the latter paper in the form of a pulsed vortex generator jet. Postl et al. (2011) found that when the flow was forced at the natural frequency of the shear layer the small-scale forcing developed into large scale coherent structures, which supplied the necessary

high-momentum fluid to re-energize and re-attach the separated boundary layer. In both cases the unsteady forcing can indeed affect significantly the length of the separation bubble and, consequently, the behaviour of the underlying device.

Stability studies on naturally occurring separation bubbles in airfoils at an angle of attack are far more limited than for flows with artificially induced separation. Boutilier and Yarusevych (2012) studied the development of the shear layer on a NACA 0018 at $Re_C = 10^5$. They found very good agreement between local linear stability analysis results and disturbance growth rates results, obtained experimentally both for pressure and velocity measurements. They suggested that the inviscid mechanism of the shear layer inflectional profile was responsible for the amplification of disturbances. Marxen et al. (2015) extended the aforementioned work of Kotapati et al. (2010) by using the same data to perform stability analysis in the flow field. It is worth pointing out, that this is the only work (at least to the author's knowledge) that an absolute instability was identified in the separation bubble.[1] This was attributed to the magnitude of the reverse flow which was approximately 16%, and thus, according to previous studies, sufficient to cause an absolute instability.

Perhaps the most pertinent to the present study is the stability analysis performed by Jones (2008), referred to earlier in the introduction. The laminar separation bubble over the NACA 0012 was extensively studied and a self-sustaining mechanism for the occurring turbulent flow field was suggested. Furthermore, an interaction was found between the trailing edge and the boundary layer structures via an acoustic feedback mechanism. This mechanism was later corroborated experimentally by Pröbsting and Yarusevych (2015).

1.4 Dynamic mode decomposition

The linear stability analysis has been one of the earliest attempts to delve into the complexity of the infinite-dimensional flow fields and describe them with a finite

[1] That is excluding the works referred earlier by Hammond and Redekopp (1998) and Rist and Maucher (2002) who as we mentioned used analytically derived profiles.

number of modes which manage to capture the fundamental behaviour of the flow. As mentioned in the previous section such attempts date back to the 1960s (see Gaster (1963, 1968)). Another approach which was firstly introduced by Lumley (1970) and reappeared during the late 1980s by Sirovich (1987) is the Proper Orthogonal Decomposition (POD). If at time i we have, either from experimental or from simulation data, a snapshot u_i of the velocity field, the POD extracts the most energetic features of the ensemble of all snapshots u_i for $i = 1, .., N$ (N is the total number of snapshots). This is done by calculating the basis functions ϕ_k which are the result of the maximization of the ensemble average of the inner product between the velocity field snapshots u_i and ϕ_k (see Berkooz et al. (1993)). This practically means that, when the velocity field is projected along the aforementioned basis functions, the projected field will have the largest kinetic energy when compared to its projection using any other basis functions. Since its inception, the POD has been used in a wide variety of flows such as channel flows, free shear flows, jets and boundary layers (for an extensive review on the mathematical properties and applications of POD see Berkooz et al. (1993) and references therein).

The most important drawback of the proper orthogonal decomposition is that it provides a kinetic energy based ranking, that is, it does not, directly, provide any information about the frequency content of the calculated modes. An alternative to the POD proposed by Schmid (2010) is the Dynamic Mode Decomposition (DMD). The DMD provides a numerical approximation to the Koopman operator (see Rowley et al. (2009) and references therein) and it allows the calculation of modes distinguished not on the basis of their energy ranking but on their frequency (a discrete equivalent of the Koopman modes). This allows the user to extract information regarding the frequency content of the various dominant structures of the flow field, and it has been proved to be a very useful tool especially in flows where various modes can be present (e.g. two cylinders with different diameters).

The DMD method lies in the assumption that a linear mapping exists between consecutive time snapshots of the datasets, and thus the spectrum of this mapping

can by analysed to extract information about the dynamic features of the flow. The linear mapping assumption is satisfied for the linearised equations and indeed it can be shown that linear stability analysis and DMD give similar results (Schmid, 2010). The advantage of the dynamic mode decomposition compared to the stability analysis though, is that, like the POD, it can be applied directly to the experimental or simulated data, i.e. without the need of calculating a base or time-averaged flow. DMD exploits the much smaller number of time snapshots, compared to grid points (which usually are orders of magnitude more), thus reducing the computational cost. As an example: for a 2D grid of size M, the global stability analysis would require calculating the eigenvalues of an approximately $3M \times 3M$ matrix (for velocity and pressure), whereas the DMD will work on the basis of a $3M \times N$ matrix, where N is the number of time snap-shots and $N \ll M$. A recap of the methods used will be presented in chapter 3.

In his original paper, Schmid (2010) applied the method in the data from three different configurations. The first was the simulation of a square cavity flow, where the DMD was able to capture the sustained oscillations formed on the separated shear layer. The second was on the PIV data from from the wake forming downstream of a flexible oscillating membrane. In the latter example an important feature of the DMD was also illustrated which is its ability to work both on spatial and temporal data (i.e. it can be used to identify both spatial modes with a given temporal frequency or spatio-temporal modes with a given wavenumber). In the last example by Schmid (2010), DMD was applied in PIV data of the flow field around two identical cylinders. The method was again able to capture the dominant modes in the downstream area. This last example makes a very good case of the ability of the method to be applied in flows with different dominant modes (in the example, the jet originating from the area between the cylinders and the two wakes) and is the reason that it was selected as a major tool in this thesis.

More recently Wan et al. (2015) applied the method in a compressible jet flow at $Re = 9 \times 10^4$. The calculated modes were found to capture the dominant process

in the flow field and their corresponding frequencies agreed well with LES data. A useful comparison between POD and DMD was also done in this study. In another recent study by Baj et al. (2015), the DMD method was applied in the PIV data of the flow downstream of a multiscale bar array. This allowed the capturing of the different shedding modes behind each bar. The data where then used to successfully decompose the flow field in three components: mean, fluctuating and "phase dependent", where the latter term was based on the shedding modes extracted using the DMD.

The method has also been applied in flows around airfoils, pertinent to the present thesis. Dunne and McKeon (2015) studied the pitching motions of wind turbine blades, motivated by the variation of the angle of attack that these blades experience due to the turbine's rotation. The so-called dynamic stall phenomenon was experimentally modelled by a sinusoidal motion of a NACA-0018 airfoil at $Re = 10^5$, with the angle of attack varying between -30^o and 30^o degrees. This resulted in a highly dynamic flow field with repeated separations and reattachments of the boundary layer as the angle varied. The authors were not only able to accurately describe the mechanisms of the occurring dynamic stall, using the modes extracted from the DMD, but they also used the phase information of the modes to identify the presence of hysteresis effects between the different cycles of the pitching motion of the airfoil. In a similar study, Mariappan et al. (2014) studied both numerically and experimentally the flow around a pitching OA209 airfoil. Motivated by the difficulty of measuring the flow velocity in the near-wall area in experiments, they studied the effect of its exclusion from the data when calculating the DMD modes. Their results showed that for attached flows there can be important differences in the DMD results when the near-wall area is excluded, but when the flow separates the differences are rendered minuscule. Furthermore, they used the DMD data to calculate a reduced order model managing to capture 90% of the flow field.

1.5 Resolvent analysis

Both the POD and the DMD, seen in the previous section, belong to the so-called data-driven methods since the analysis is applied directly to the results of an experiment or a simulation. The linear stability analysis on the other hand, is an operator-driven method since the properties of the linearised Navier-Stokes operator are studied rather than the actual flow data. Approximately at the same period with DMD another similar, but operator-driven, method, based on the resolvent operator, was proposed by McKeon and Sharma (2010). The resolvent operator has long been studied in the context of the spectral theory of linear operators (see for example the book by Kato (2013)). In the context of fluid-dynamics, the resolvent analysis was motivated, in the work of McKeon and Sharma (2010), by the usage of the mean flow field (as opposed to the base flow) as a starting point to perform a reduced order analysis of the flow field. Its novelty lies in the fact that, unlike the global stability analysis which assumes a perturbation field aroung a fixed-point solution, the resolvent analysis takes the fluctuations field around the mean, which can be readily obtained. The applicability of the resolvent lies in the application of the non-linear part of the Navier-Stokes equations as an input to their linear dynamics. This is done by writing the Reynolds decomposed Navier-Stokes equations in an input-output form (similar to a linear system), where the input of the system (which is the non-linear part of the Navier-Stokes equations) is connected to its output via the aforementioned resolvent operator. More details on the relevant mathematical formulation will be given in chapter 4. The work by Sharma et al. (2016) provides the mathematical links between the dynamic mode decomposition and the resolvent operator.

The analysis of the resolvent operator, by means of its singular value decomposition, allows one to calculate the set of those turbulent forcings that will yield the largest response on the flow field. Such results have been used until now in various different contexts and flow configurations. In the original paper by McKeon and

Sharma (2010) the resolvent operator was used in a turbulent pipe flow to study those modes with the most energetic response for a given frequency and wavenumber (azimuthal and streamwise) of forcing. Depending on the overall effect of the modes on the flow field and their spatial structures, the authors identified regions along the radial direction of the pipe where different scaling laws apply. Similar results but for a turbulent channel flow were presented by Moarref et al. (2013).

Sipp et al. (2010) used the resolvent operator to capture the Tollmien-Schlichting waves in a Blasius boundary layer. A more thorough analysis of a similar flow field was performed by Sipp and Marquet (2013), where they also managed to identify the Orr and TS mechanisms using the resolvent operator analysis. Furthermore, in their work they found the results of the resolvent analysis to be in very good agreement with results from the e^N method. The latter method uses the linear stability analysis to predict the location of the onset of transition for locally parallel flows. This location was found to match very well with the location where the response, calculated from the resolvent analysis, starts to amplify. Sartor et al. (2014) used the resolvent operator to study the shock wave - boundary layer interaction on a OAT15 airfoil. While the global stability analysis they performed captured the major source of instability (the shock buffeting), they managed, using the response modes of the resolvent operator, to also capture secondary pseudoresonance phenomena, attributed to convective instabilities in the flow field, which can have an important effect in the overall response.

Beneddine et al. (2016) used the resolvent analysis to study the extent to which the mean flow can be used in stability analysis. Similarly to the work of McKeon and Sharma (2010), they wanted to study under which conditions the mean flow field can be used as a meaningful proxy for the base flow, which is the mathematically appropriate solution around which the perturbation field is studied in the context of linear stability analysis. They concluded that in cases where a strong convective instability is present and the first singular value of the resolvent operator is several orders of magnitude larger than the rest, then the corresponding resolvent mode will

approximate well the spectral mode (i.e. the result of a stability analysis). Thus, in such cases, the eigenspectrum of the linearised flow field around the mean will indeed yield a good approximation of the mathematically correct eigenspectrum around the base flow.

Another important feature of the resolvent operator is its usage in the reconstruction of the flow-field using just the mean flow and the signal from a single probe (although usage of more probes can improve the estimation), which is used to calibrate a weight function.Gómez et al. (2016a) used the mean flow field and the data from a probe to estimate the actual flow velocities on a cavity flow, with a 5% accuracy. A study of the probe's location was also included in the work by Gómez et al. (2016a), which was found to have an important effect on the estimation, depending on the energy content of the flow field at the specific location. Gómez et al. (2016b) extended the previous work on a square cylinder flow, including the pressure signal in the calculations. They were then able to calculate estimates, not only for the velocity signal, but also for the lift and drag coefficients of the forces acting on the cylinder, which were in very good agreement with DNS data. Last but not least, in the work by Beneddine et al. (2016), the authors used the results from the resolvent analysis, to estimate the energy spectra of the flow field of a backward facing step using again a single probing point.

1.6 Current Study

As was demonstrated, the numerical studies investigating the spectral characteristics of flows over airfoils with naturally developing laminar separation bubbles are limited. The vast majority of numerical studies have focused on artificially induced separation bubbles on flat plates, with very few attempts to simulate an aerodynamic flow configuration realistically. To this extent, the present work builds on the existing knowledge of low Reynolds number flows over airfoils, while at same time applying methods to study their spectral behaviour, in an attempt to identify

potential interactions between different trailing edge geometries and the laminar separation bubble, which forms on its suction side. Two questions that naturally arise, and which this study attempts to answer are: *how is the hydrodynamic field affected by the different trailing edges?* and *is there any effect or interaction between the trailing edge and the separated boundary layer and separation bubble?*.

More specifically the aims of this study are:

- To provide DNS quality data of an airfoil for the specific flow configuration.
- To study the hydrodynamic field formed by the different trailing edges.
- To study the role and importance of the separation bubble in these flow conditions.
- To assess the effect of the different trailing edges and, consequently, the different shedding characteristics of the wake, on the dynamic behaviour of the laminar separation bubble.
- To investigate the response characteristics and the sensitivity of the flow field.

The thesis is organized as follows:

- In chapter 2 details are provided regarding the solver which was used in this work, along with details on the airfoil geometries simulated and their meshing. This chapter also includes the validation against other DNS data from literature and meshing convergence studies.
- In chapter 3 the results of the simulations for three trailing edges are presented. The dynamic features of the flow fields are investigated using the dynamic mode decomposition method.
- In chapter 4 the resolvent analysis is applied and the effect of the trailing edges on the response and sensitivity characteristics is studied.

– In chapter 5 a numerical tripping method is applied in order to suppress the laminar separation bubble. This is done in an attempt to isolate the effect of the trailing edge from that of the separation bubble, and assess the importance of the former in the dynamic characteristics of the flow field.

Chapter 2

Numerical methodology and validation

2.1 Introduction

The discretisation and solution methods used throughout the thesis, as well as validation studies are presented in this chapter. The first part of the chapter considers the DNS solver, while the second part the solver used for the calculation of the eigenvalues.

2.2 Governing equations and their solution

The incompressible Navier-Stokes equations

$$\frac{\partial \boldsymbol{u}}{\partial t} + \boldsymbol{u} \cdot \nabla \boldsymbol{u} = -\frac{1}{\rho}\nabla p + \nu \nabla^2 \boldsymbol{u}, \tag{2.1}$$

$$\nabla \cdot \boldsymbol{u} = 0, \tag{2.2}$$

are discretised and solved in a non-orthogonal, unstructured mesh using the Finite Volume Method (FVM). The method is implemented in an in-house code called PantaRhei. For the simulations presented in the thesis, the meshes comprise only

of hexahedral cells. The 4 flow variables (3 velocity components and pressure) are all stored at the centroid of each cell (collocated arrangement). In the following sections details are provided on the dicretisation of each term of the Navier-Stokes equations. For a more thorough analysis of the methods used the reader is referred to the books of Ferziger and Peric (1996) and Versteeg and Malalasekera (2007).

2.2.1 Discretisation of the generic transport equation

The generic transport equation for a scalar ϕ advected by a velocity field $\mathbf{u}$ is given by:

$$\underbrace{\frac{\partial(\rho\phi)}{\partial t}}_{\text{transient term}} + \underbrace{\nabla\cdot(\rho\phi\mathbf{u})}_{\text{convective term}} = \underbrace{\nabla\cdot(D_\phi\nabla\phi)}_{\text{diffusive term}} + \underbrace{S_\phi}_{\text{source term}}, \tag{2.3}$$

where D_ϕ is the diffusivity of scalar ϕ. In the context of the Navier-Stokes equations, ϕ can be any of the 3 velocity components. Integration of equation (2.3) over a control volume CV gives

$$\int_{CV}\frac{\partial(\rho\phi)}{\partial t}dV + \int_{CV}\nabla\cdot(\rho\phi\mathbf{u})dV = \int_{CV}\nabla\cdot(D_\phi\nabla\phi)dV + \int_{CV}S_\phi dV. \tag{2.4}$$

Each term in equation (2.4) is discretised and treated separately, this process is presented next for each term.

Convective term

The volume integral of the convection term is first transformed into a surface integral by invoking the Gauss divergence theorem. The surface integral is then written as a finite sum over the faces of the control volume. The convective term is written as:

$$\int_{CV}\nabla\cdot(\rho\phi\mathbf{u})dV = \oint_{S_{CV}}\rho\phi\mathbf{u}\cdot\mathbf{n}dS, \tag{2.5}$$

where S is the boundary of the control volume and $\mathbf{n}$ is the unit vector normal to S pointing outside the control volume. The surface integral is written as a finite sum

over all the faces of the control volume, i.e.:

$$\oint_{S_{CV}} \rho\phi\mathbf{u}\cdot\mathbf{n}dS_{CV} \approx \sum_{i=1}^{6} \rho\phi_i\mathbf{u}_i\cdot\mathbf{n}_i S_i. \tag{2.6}$$

Each face i is associated with its unit normal vector $\boldsymbol{n}_i$ and its area S_i. The quantity $F_i^{conv} = \rho\phi_i\mathbf{u}_i\cdot\mathbf{n}_i S_i$ inside the sum in equation (2.6), is the convective flux of the flow variable ϕ and it represents the rate at which ϕ flows across each face i.

Variable ϕ must be approximated at each face i. As already mentioned, all the flow variables are stored in the cell centroids, so an interpolation is performed in order to compute the values at each face. In the present thesis, we use the central difference scheme which is second order accurate in space (Ferziger and Peric (1996)) for uniform meshes. The flow variable ϕ_i at face i is approximated according to:

$$\phi_i \approx w\phi_P + (1-w)\phi_N, \tag{2.7}$$

where ϕ_P and ϕ_N are the values of ϕ at the centroids of the cells P and N, adjacent to face i (refer to Figure 2.1). The value of the weight w is given by

$$w = \frac{d_f}{d_c}, \tag{2.8}$$

where d_f is the distance between the centroid of cell P and face f, and d_c is the distance between the centroids of the two cells. For non-orthogonal cells, such as those shown in Figure 2.2, and non-uniform grid, the accuracy of the scheme is reduced and the approximation is no longer second order accurate (see Chapter 11 in the book of Ferziger and Peric (1996)).

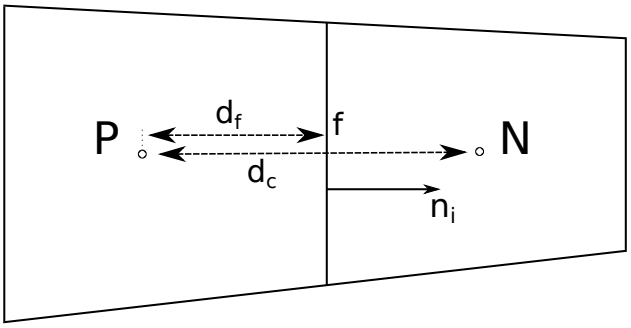


Figure 2.1: Geometry of two cells adjacent to face f.

Diffusive term

Using the divergence theorem again we get

$$\int_{CV} \nabla \cdot (D_\phi \nabla \phi) dV = \oint_{S_{CV}} D_\phi \nabla \phi \cdot \mathbf{n} dS. \tag{2.9}$$

Discretisation of the surface integral gives

$$\oint_{S_{CV}} D_\phi \nabla \phi \cdot \mathbf{n} dS \approx \sum_{i=1}^{6} D_\phi \left(\nabla \phi_i\right) \cdot \mathbf{n}_i S_i. \tag{2.10}$$

The dot product $\nabla \phi_i \cdot \mathbf{n}_i$ represents the directional derivative $\frac{\partial \phi}{\partial \mathbf{n}}$ of the flow variable ϕ at face i, along the direction of the face normal $\mathbf{n}_i$. For orthogonal meshes $\frac{\partial \phi}{\partial \mathbf{n}}$ can be easily approximated using a second order central scheme between the cells P and N (refer to Figure 2.1). In this case, the diffusive flux through each face i becomes

$$F_i^{diff} = D_\phi \left(\frac{\partial \phi}{\partial \mathbf{n}_i}\right) S_i \approx D_\phi \frac{\phi_N - \phi_P}{d_c} S_i. \tag{2.11}$$

Equation (2.11) is valid for orthogonal meshes only. Misalignment between the unit normal vector at face i and the vector connecting the adjacent cell centroids (vectors $\mathbf{n}$ and $\boldsymbol{\xi}$ respectively in Figure 2.2), will introduce an error in the calculation of $\frac{\partial \phi}{\partial \mathbf{n}_i}$ because it can no longer be computed by taking the difference between ϕ_P and ϕ_N. In order to compute correctly $\frac{\partial \phi}{\partial \mathbf{n}_i}$ the deferred correction approach is used

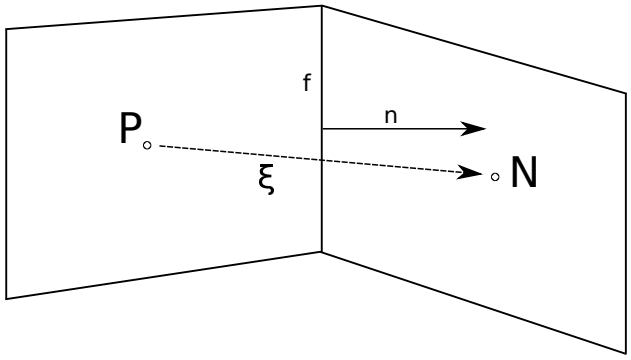


Figure 2.2: Topology of two adjacent non-orthogonal cells.

introduced by Muzaferija (1994). According to this method, a correction term is added to equation (2.11), which now becomes

$$F_i^{diff} = D_\phi \frac{\phi_P - \phi_N}{d_c} S_{CV,i} + D_\phi \overline{\left.\frac{\partial \phi_i}{\partial \boldsymbol{n}_i}\right|_{old}} \cdot (\mathbf{n}_i - \boldsymbol{\xi}_i). \tag{2.12}$$

The second term in equation (2.12) is the correction term and it is calculated from the gradients of the previous iteration. The term $\overline{\left.\frac{\partial \phi_i}{\partial \boldsymbol{n}_i}\right|_{old}}$ is computed using linear interpolation of the gradients computed at the centroids of the two control volumes P and N. If the unit vectors $\boldsymbol{n}$ and $\boldsymbol{\xi}$ are aligned the second term vanishes and we revert back to equation (2.11). When building the mesh, care is taken in order to minimise non-orthogonality and mesh skewness. Strong skewness can also reduce the accuracy of the convective term approximation.

Transient term

In the current work the transient term was discretised using a second-order backward Euler implicit scheme. The derivative $\frac{\partial \phi}{\partial t}$ at time instant n+1 is approximated as:

$$\left.\frac{\partial \phi}{\partial t}\right|_{n+1} \approx \frac{1}{2\Delta t}(3\phi^{n+1} - 4\phi^n + \phi^{n-1}). \tag{2.13}$$

Source term

The source term S_ϕ in the generic transport equation contains any additional forces exerted on the fluid, such as gravity, buoyancy, centrifugal forces (i.e. in a rotational flow) and pressure. The generic discretisation of a source term gives:

$$\int_{CV} S_\phi dV \approx S_\phi\left(P\right) V. \tag{2.14}$$

where $S_\phi\left(P\right)$ is the value of the variable ϕ at the centroid P and V is the volume of the control volume under consideration.

The pressure gradient term in the momentum equations is treated as a source term, giving:

$$-\int_{CV} \nabla p \; dV \approx -\frac{\delta p}{\delta \boldsymbol{x}} V. \tag{2.15}$$

The operator $\frac{\delta}{\delta \boldsymbol{x}}$ denotes the spatial discretisation scheme used for the pressure gradient and will be discussed later in this chapter.

Final form of the discretised transport equation

Putting together the various terms discussed in the previous paragraphs, the discretised generic transport equation (2.3) becomes:

$$\frac{\rho}{2\Delta t}(3\phi^{n+1} - 4\phi^n + \phi^{n-1}) + \left(\sum_{i=1}^{6} \rho\phi_i \mathbf{u}_i \cdot \mathbf{n}_i S_i\right)^{n+1} = \left(\sum_{i=1}^{6} D_\phi \nabla\phi_i \cdot \mathbf{n}_i S_i\right)^{n+1} + \\ + \left(S_\phi V\right)^{n+1}, \tag{2.16}$$

where the superscript $(n+1)$ indicates the time instant. Equation (2.16) has the following general form:

$$A_P^\phi \phi_P^{n+1} = \sum_{l=1}^{6} A_l^\phi \phi_l^{n+1} + S_\phi^{n+1} V. \tag{2.17}$$

The index P corresponds to the control volume for which the discrete equation is written, and the index l is a counter of the neighbouring cells. The coefficients A^{ϕ} in equation (2.17) contain the contributions from the convective and diffusive fluxes as well as the transient term. The convective flux term F_i^{conv} is treated using a semi-implicit approach according to which the velocity product at time step n is written as:

$$u_j^{n+1}u_i^{n+1} = \tilde{u}_j^{n+1}u_i^{n+1}, \tag{2.18}$$

where $\tilde{u}_j^{n+1}$ is an extrapolation from the velocity fields from the previous two time steps. This approximation makes the algebraic system (2.17) linear and allows the application of the pre-conditioned conjugate gradient method for the solution. The extrapolation is 2^{nd} order accurate in time, i.e. the same order as the discretisation of the transient term.

2.2.2 Treatment of the pressure term

It has already been mentioned that all velocity components and pressure are stored in cell centroids (collocated grid). The obvious advantage of this storage pattern is that all equations are treated similarly, which facilitates the coding implementation. This also reduces the number of coefficients that need to be calculated and stored. This arrangement however, results in oscillations in the pressure field between adjacent cells (see the book of Ferziger and Peric (1996)).

A simplified explanation of this problem can be given by studying the discretised equations in the uniform grid shown in Figure 2.3. The pressure gradient forcing term in the momentum equation at cell i would in this case be:

$$\left.\frac{\partial p}{\partial x}\right|_i = \frac{p_e - p_w}{\Delta_i} = \frac{p_{i+1} - p_{i-1}}{2\Delta_i}, \tag{2.19}$$

where Δ_i is the distance between the east and west faces of cell i. In the 2^{nd} equality, the face values were computed using linear interpolation from the adjacent centroid

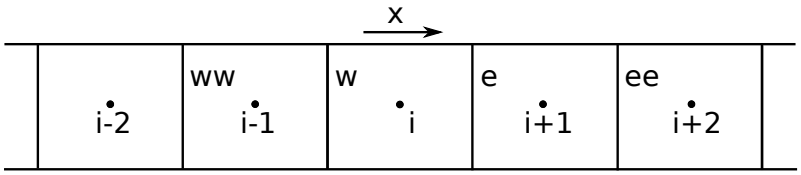


Figure 2.3: A uniform 1D CV arrangement.

values and, for uniform meshes, p_i cancels out resulting in equation (2.19). It is clear that the pressure gradient in cell i depends on the values of the pressure at cells $i+1$ and $i-1$, thus the velocity at cell i will depend on pressure at these cells. If, in the case of the grid shown in Figure 2.3, the pressure values at cells $i-1, i$ and $i+1$ are correspondingly 1,-1 and 1, the pressure gradient at cell i will appear to be zero. It is therefore possible to arrive to a solution that will satisfy the continuity equation and at the same time have an oscillating pressure field. This is clearly unrealistic, and a method is required that can detect and eliminate the oscillations.

The obvious solution to this problem is to use a staggered grid, and this is the grid type that was used until other remedies appeared. In the present study this problem is solved by using the Rhie-Chow interpolation scheme introduced by Rhie and Chow (1983). According to this scheme, the three velocity components at the east cell face for example are computed as:

$$u_e = wu_i^* + (1-w)u_{i+1}^* \underbrace{-\frac{V}{A_P}\left(\left.\frac{\partial p}{\partial x}\right|_e - \overline{\frac{\partial p}{\partial x}}\right)}_{correction\ term}, \tag{2.20}$$

where w is the weight introduced earlier in equation (2.8). It is easy to show using a Taylor expansion that the correction which is added to the linearly interpolated velocity is proportional to the third order derivative of the pressure (Ferziger and Peric, 1996). Thus when oscillations appear, this term will detect them and the correction will act to smooth out the pressure field.

2.2.3 Pressure-velocity coupling

The system that needs to be solved includes the three discrete momentum equations and continuity. The momentum equations include all the variables, while the latter includes only the three velocity components. This absence of an equation for pressure necessitates the introduction of an iterative method to extract pressure in a way so that the computed velocity satisfies continuity.

Two well-known algorithms to implement the aforementioned process are the SIMPLE (Patankar, 1980) (acronym for Semi Implicit Method for Pressure Linked Equations) and the PISO algorithms (Issa, 1986) (acronym for Pressure Implicit with Splitting Operator). The latter is an extension of the former. In the code used in the present work the PISO algorithm is employed. Other methods also exist like the fractional step method (Kim and Moin, 1985) but they were not considered in this study.

PISO Method

The discretised form of the transport equation (2.17) is written for the k^{th} velocity component

$$A_P^{u_k} u_{k,P}^{m,*} = \sum_l A_l^{u_k} u_{k,l}^{m,*} - \frac{\delta p^{m-1}}{\delta x_k} V_P + S_{u_k^{m-1}} V_P, \tag{2.21}$$

where the source term S_{u_k} contains the various correction terms, such as those arising due to the grid non-orthogonality, as well as the terms from the discretised time derivative in equation (2.13) (i.e. the velocities from the previous time steps). The asterisk superscript indicates an intermediate velocity field. Finally, the superscript m indicates the internal iteration counter, within each time step

The method starts by solving the system of equations, resulting from (2.21), for $u_{k,P}^{m,*}$ using the pressure field from the previous iteration, m-1.

The solution of equation (2.21) gives an intermediate velocity field u_k^*, which however does not satisfy continuity. So the pressure field p^{m-1} and the velocity field

$u_k^{m,*}$ are corrected using, the still unknown, corrections p' and u'_k respectively, i.e.

$$u_{k,P}^{**} = u_{k,P}^{m,*} + u'_k, \tag{2.22a}$$

$$p^{**} = p^{m-1} + p'. \tag{2.22b}$$

The objective now is to compute u'_k and p'. The first step is to find a relation between u'_k and p' The corrected fields will satisfy:

$$A_P^{u_k} u_{k,P}^{**} = \sum_l A_l^{u_k} u_{k,l}^{**} - \frac{\partial p^{**}}{\partial x_k} V + S_{u_k^{m-1}} V. \tag{2.23}$$

Subtracting equation (2.21) from equation (2.23) we get:

$$A_P^{u_k} u'_{k,P} = \sum_l A_l^{u_k} u'_{k,l} - \frac{\partial p'}{\partial x_k} V_P. \tag{2.24}$$

The fundamental assumption of the SIMPLE method is to drop the summation term in equation (2.24). This is done because the correction terms are still unknown at this stage. This does not affect the final result, since in the converged solution the correction terms will be zero, but it does affect the rate of convergence (Versteeg and Malalasekera, 2007). After this approximation the corrected velocities are given by:

$$u_{k,P}^{**} = u_{k,P}^{m,*} - \frac{\partial p'}{\partial x_k} \frac{V}{A_P^{u_k}}, \tag{2.25}$$

where the pressure correction term is still unknown. In order to calculate p', we invoke the continuity equation. Application of the divergence theorem on the continuity equation using the corrected velocities, gives:

$$\int_{CV} \rho \nabla \cdot \boldsymbol{u}^{**} dV = \oint_{S_{CV}} \rho \boldsymbol{u}^{**} \cdot \boldsymbol{n} dS = \oint_{S_{CV}} \left(\rho \boldsymbol{u}^{m,*} - \rho \frac{\partial p'}{\partial \boldsymbol{x}} \frac{V}{A_P^{u_k}} \right) \cdot \boldsymbol{n} dS = 0, \tag{2.26}$$

which after discretisation gives:

$$\sum_{i=1}^{6} \rho \left(\boldsymbol{u}_i^{m,*} \cdot \boldsymbol{n}_i \right) S_i - \sum_{i=1}^{6} \rho \left(\frac{\partial p'}{\partial \boldsymbol{x}} \cdot \boldsymbol{n}_i \right) \frac{V_P}{A_P^{u_k}} S_{k,i} = 0, \tag{2.27}$$

where the outer sums are over the 6 faces of each cell. Solution of equation (2.27) gives p'. This is where the SIMPLE algorithm stops.

The PISO algorithm adds a second correction step, which calculates a new pressure and velocity correction from equation (2.24). The difference now is that the summation term in equation (2.24), which was previously neglected, is approximated using the calculated u'_k from the first correction step. The newly corrected fields become:

$$u_{k,P}^{m+1} = u_{k,P}^{**} + u''_{k,P}, \tag{2.28a}$$

$$p^{m+1} = p^{**} + p'', \tag{2.28b}$$

where u_k^{**} and p^{**} have been calculated in the first correction step. The correction u''_k is obtained from equation (2.24):

$$u''_{k,P} = \frac{\sum_l A_l^{u_k} u'_{k,l}}{A_P^{u_k}} - \frac{\partial p''}{\partial x_k} \frac{V_P}{A_P^{u_k}}. \tag{2.29}$$

Using $u''_{k,P}$, the velocities $u_{k,P}^{m+1}$ are calculated and substituted in the discretised continuity equation and a new pressure correction p'' is obtained. After the new p'' has been calculated, the velocity and pressure fields are finally updated according to equations (2.28a), (2.28b) and (2.29). The process is repeated until the requested convergence tolerance has been achieved. For the reader's convenience, the algorithm is summarised here:

1. Initialise the pressure and velocity fields using either a restart file from a previous simulation or the fields from the last time step.

2. Solve the discretised momentum equations (2.21), using the current pressure field, to calculate an intermediate velocity field.

3. Update face velocities using the previously calculated field and evaluate the first pressure correction from equation (2.27).

4. Correct the pressure and velocities according to (2.22a), (2.22b) and (2.25).

5. Update face velocities and calculate the second pressure correction from equation (2.27).

6. Correct the pressure and velocities according to equations (2.28a), (2.28b) and (2.29).

7. Repeat steps 2 to 6 to until convergence is achieved

8. Return to step 2 for the new time step.

The convergence of the algorithm is fast, and usually no more than 2 or 3 corrections are required.

2.2.4 Boundary conditions

In the boundaries of the domain, fictitious 2D cells are defined to store the boundary values. Since the finite volume method works on the basis of fluxes through cell faces, this approach allows the boundary conditions to be easily applied.

In the present work 5 types of boundaries are used: inlet, outlet, no-slip wall, symmetric and periodic.

Inlet boundaries

At the inlet boundary the free stream velocity is prescribed. This is implemented by setting the velocities at the fictitious boundary cells equal to the free stream velocity U_∞. Diffusive and convective fluxes can then be easily calculated. Since the velocity is prescribed at these cell faces, the corresponding corrections are set to zero.

Because of incompressibility pressure is calculated with respect to a reference pressure cell, which is arbitrarily set to zero. The pressure reference cell is also

selected at the inlet and away from the region of interest. The pressure correction for this cell is also set to zero.

Outlet boundaries

At the outlet boundary a convective boundary condition is used. Each velocity component satisfies:

$$\frac{\partial u_k}{\partial t} + u_{conv}\frac{\partial u_k}{\partial x} = 0, \tag{2.30}$$

where x is the streamwise direction. The local convective velocity u_{conv} is computed from the flux at the boundary face. The assumptions behind this boundary condition is that the diffusive and pressure forces are negligible and that there is no back-flow into the domain. For these reasons the outlet boundary is taken away from the region of interest (more details are provided below)

No-slip wall

At the wall boundaries, the convective fluxes are set to zero due to the impermeability condition. Tangential velocities are also set to zero. The shear stress is calculated directly using a first order approximation of the wall normal derivative of the tangential velocity.

Symmetric boundaries

At the symmetry faces the convective fluxes of all velocity components are zero. Furthermore the gradients normal to the boundary of the tangential velocity and pressure are set to be zero.

Periodic boundaries

The periodic boundary simulates an infinite repetition of the domain in the corresponding direction (for example in the spanwise direction for an infinite wing). The flow variables from an internal cell with a periodic boundary face are copied

to a corresponding fictitious boundary cell. A simple illustration is shown in Figure 2.4 with two linked periodic cells. The flow variables from the internal cell C1 will be copied to the fictitious cell BC2 and the variables from cell C2 will be copied to BC1. It must be pointed out that in order to avoid unnecessary interprocessor communication during execution, the corresponding periodic cells are should belong to the same partition.

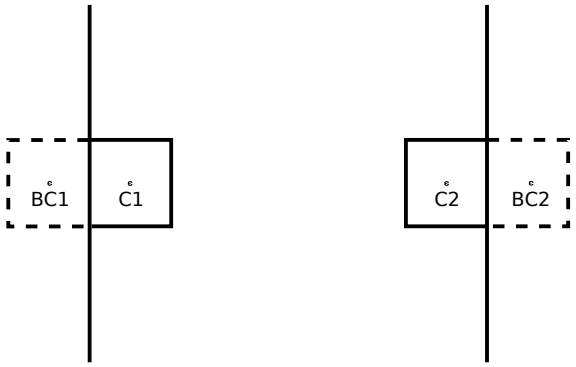


Figure 2.4: Example of the treatment of periodic boundaries.

2.3 Numerical methods for the computation of eigenvalues

Assuming that the velocity and pressure fields are evolving in the state-space around a steady (or fixed-point) solution, the two fields can be written as $\boldsymbol{u} = \boldsymbol{u}_b + \boldsymbol{u'}$ and $p = p_b + p'$ respectively, where the underscore b indicates a base field (i.e. a steady solution of the Navier-Stokes equations) and the dash indicates the fluctuations around this steady state. By definition $\boldsymbol{u}_b$ and p_b satisfy:

$$\boldsymbol{u}_b \cdot \nabla \boldsymbol{u}_b = -\frac{1}{\rho}\nabla p_b + \nu \nabla^2 \boldsymbol{u}_b, \tag{2.31}$$

$$\nabla \cdot \boldsymbol{u}_b = 0. \tag{2.32}$$

The fluctuating quantities then satisfy:

$$\frac{\partial \boldsymbol{u}'}{\partial t} + \boldsymbol{u}_b \cdot \nabla \boldsymbol{u}' + \boldsymbol{u}' \cdot \nabla \boldsymbol{u}_b + \boldsymbol{u}' \cdot \nabla \boldsymbol{u}' = -\frac{1}{\rho}\nabla p' + \nu \nabla^2 \boldsymbol{u}', \tag{2.33}$$

$$\nabla \cdot \boldsymbol{u}' = 0. \tag{2.34}$$

If the fluctuations are assumed to be of order ϵ, where ϵ is a sufficiently small positive number, i.e. it $0 < \epsilon \ll 1$, then the last two terms of equation (2.33) will be of order ϵ^2 and therefore can be ignored. This results in the linearised Navier-Stokes equations for an infinitesimal perturbation $\boldsymbol{u}'$, around the base flow field $\boldsymbol{u}_b$:

$$\frac{\partial \boldsymbol{u}'}{\partial t} + \boldsymbol{u}_b \cdot \nabla \boldsymbol{u}' + \boldsymbol{u}' \cdot \nabla \boldsymbol{u}_b = -\frac{1}{\rho}\nabla p' + \nu \nabla^2 \boldsymbol{u}', \tag{2.35}$$

$$\nabla \cdot \boldsymbol{u}' = 0. \tag{2.36}$$

Using matrix notation the previous system of equations can be written as:

$$\boldsymbol{B}\frac{\partial}{\partial t}\begin{pmatrix} \boldsymbol{u}' \\ p' \end{pmatrix} = \boldsymbol{L}\begin{pmatrix} \boldsymbol{u}' \\ p' \end{pmatrix}, \tag{2.37}$$

where the operator $\boldsymbol{L}$ and matrix $\boldsymbol{B}$ are defined as follows:

$$\boldsymbol{L} = \begin{pmatrix} -\boldsymbol{u}_b \cdot \nabla() - () \cdot \nabla \boldsymbol{u}_b + \nu \nabla^2() & -\frac{1}{\rho}\nabla() \\ \nabla \cdot () & 0 \end{pmatrix}, \tag{2.38}$$

$$\boldsymbol{B} = \begin{pmatrix} 1 & 0 \\ 0 & 0 \end{pmatrix}. \tag{2.39}$$

$\boldsymbol{L}$ is known as the linearised Navier-Stokes operator.

The discrete form of equation (2.37) depends on the discretisation method used. In the present work we have used the FreeFem++ software (Hecht, 2012), which implements the Finite Element Method, with P2 elements for the velocity variables and P1 elements for pressure. The discrete form of $\boldsymbol{B}$ is the mass matrix.

Assuming that the perturbations have the form $\boldsymbol{u}'(\boldsymbol{x},t) = \hat{\boldsymbol{u}}(\boldsymbol{x})e^{\lambda t}$ and $p'(\boldsymbol{x},t) = \hat{p}(\boldsymbol{x})e^{\lambda t}$, where the amplitudes $\hat{\boldsymbol{u}}$ and $\hat{p}$ and the frequency λ are complex numbers, equation (2.37) can be written as:

$$\lambda \boldsymbol{B} \begin{pmatrix} \hat{\boldsymbol{u}} \\ \hat{p} \end{pmatrix} = \boldsymbol{L} \begin{pmatrix} \hat{\boldsymbol{u}} \\ \hat{p} \end{pmatrix} \tag{2.40}$$

Defining vector $\boldsymbol{\phi} = \begin{pmatrix} \hat{\boldsymbol{u}} \\ \hat{p} \end{pmatrix}$ the previous can be recast as a generalized eigenvalue problem:

$$\boldsymbol{L}\boldsymbol{\phi} = \lambda \boldsymbol{B}\boldsymbol{\phi}. \tag{2.41}$$

The eigenproblem in equation (2.41) cannot be further simplified because matrix $\boldsymbol{B}$ is singular (see equation (2.39)).

To evaluate the eigenvalues λ and the eigenvectors $\boldsymbol{\phi}$ and to circumvent the aforementioned problem the Shift-And-Invert method is used. A shift σ (complex in the general case) is first applied to equation (2.41) resulting in:

$$(\boldsymbol{L} - \sigma \boldsymbol{B})\boldsymbol{\phi} = (\lambda - \sigma)\boldsymbol{B}\boldsymbol{\phi}. \tag{2.42}$$

Given that the matrix $\boldsymbol{L} - \sigma \boldsymbol{B}$ is invertible (since $\boldsymbol{L}$ is by construction invertible), the eigenproblem in equation (2.42) can be transformed to:

$$(\boldsymbol{L} - \sigma \boldsymbol{B})^{-1}\boldsymbol{B}\boldsymbol{\phi} = \nu \boldsymbol{\phi}, \tag{2.43}$$

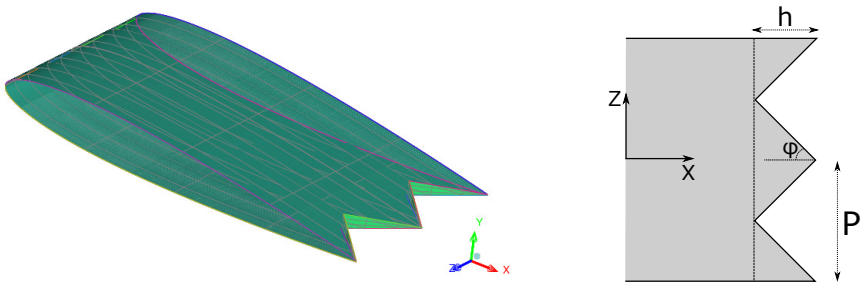
where $\nu = \frac{1}{(\lambda - \sigma)}$. By solving the eigenproblem defined in equation (2.43), with one of the standard methods such as the Arnoldi algorithm, we recover the eigenvalues ν with the largest magnitude, i.e. those of the original eigenproblem (2.41) that are closest to σ. Once we calculate ν, we can readily get $\lambda = \sigma + \frac{1}{\nu}$. The aforementioned calculations are performed in an external in-house programme, which uses the ARPACK library (Lehoucq et al., 1998), coupled with the MUMPS library

(Amestoy et al., 2001) (which is a linear solver library developed for large sparse systems), in order to handle the matrix inversions.

2.4 Meshing and validation

2.4.1 Geometrical details of the simulations

Three different trailing edge geometries were simulated using the numerical methodology described in the previous sections: a straight (unmodified) one, a blunt and a serrated. The Reynolds number in all cases was $Re_C = 50,000$, The NACA 0012 profile was used, placed at 5^o angle of attack. The blunt trailing edge is formed by a uniform cut along the span of the airfoil at a distance $h = 0.133C$ from the trailing edge. This creates a uniform bluntness of thickness $\epsilon = 0.037C$. The serrated trailing edge is formed by diagonal cuts from the trailing edge into the airfoil, creating a gradually increasing bluntness. The maximum bluntness in the serrated airfoil matches that of the blunt one. The geometric details of the serrated trailing edge are shown in Figure 2.5. As shown in Figure 2.5b the values of two of the three parameters h,ϕ and P are needed to fully define the shape of the serrations, which in the present work, and in accordance with the work in Nedić and Vassilicos (2015), were $h = 0.133C$, $P = 0.266C$ and $\phi = 45^o$.



(a) (b)

Figure 2.5: Serrated trailing edge airfoil geometry (2.5a) and characteristic dimensions (2.5b).

2.4.2 Computational domain and discretisation

The domain boundaries around the airfoil followed a C-type topology which has been extensively used in airfoil simulations in the past (for example by Jones (2008); Lehmkuhl et al. (2013b); Shan et al. (2005b); Zhang and Samtaney (2015a)). In Figure 2.6 an outline of the domain (not in scale) is shown.

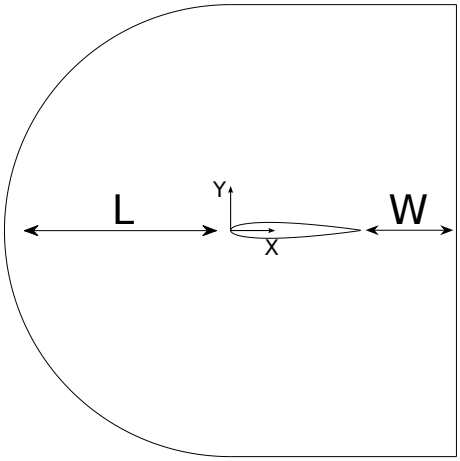


Figure 2.6: Domain topology used in the simulations.

The leading edge of the airfoil is located at the origin of the coordinate system. The three values that are needed to define the domain around the airfoil are the distances from the leading edge L, the trailing edge W and its spanwise extent ΔZ. The serrated airfoil, due to the complicated geometry of the trailing edge, required special treatment, nevertheless the overall characteristics of the domain size remained the same. The values of the 3 parameters mentioned are summarized in Table 2.1

	L	W	ΔZ
Straight (M1)	$6.0C$	$4.0C$	$0.1C$
Straight (M2)	$18.0C$	$20.0C$	$0.2C$
Blunt	$6.0C$	$6.0C$	$0.2C$
Serrated	$6.0C$	$6.0C$	$0.532C$

Table 2.1: Parameters defining the size of the domains used in the simulations.

For the straight trailing edge airfoil two entries (M1) and (M2), with different domain sizes were used. The straight trailing edge airfoil was used for a mesh convergence study using these two meshes. The results of the mesh convergence study are presented in the next section.

The top and bottom surfaces were assigned symmetric boundary conditions, while the side boundaries were periodic. The flow velocity was prescribed at the inlet, while at the outlet the convective boundary condition, discussed earlier in this chapter, was used. The commercial software ANSYS® ICEM CFD ™ was used for designing and meshing the various airfoil geometries simulated. A close up of the mesh is shown in Figure 2.7 (not every cell is shown).

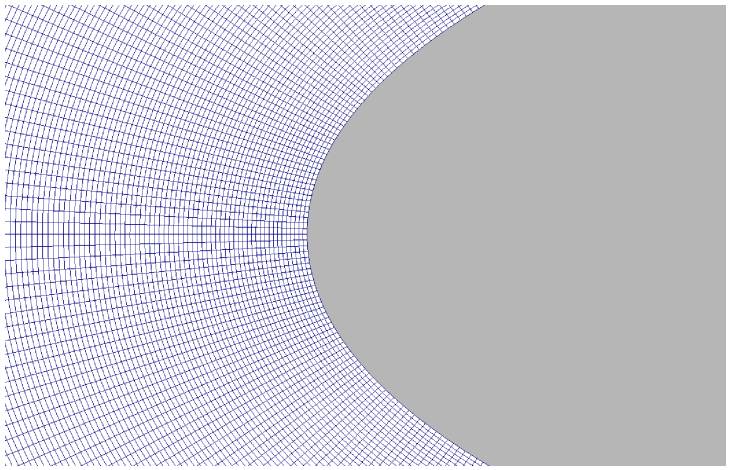


Figure 2.7: Close up of the mesh at the vincinity of the leading edge).

2.4.3 Mesh convergence and validation study

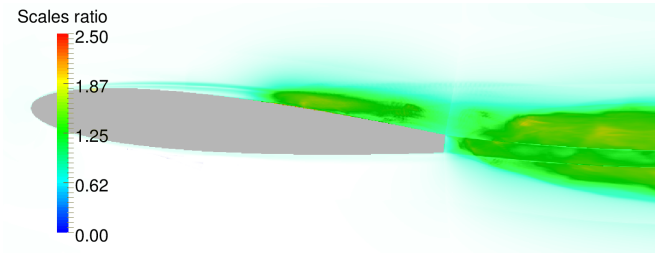
In the current section mesh convergence and validation data for the cases studied in this thesis are going to be presented. For a more generic validation study of the code's behaviour the reader is referred to the PhD thesis of Portela (2017). The size of the computational domain in 3D must be large enough to capture the potential flow as accurately as possible, while at the same time minimising the computational expense. The domain of Jones et al. (2008) extends a radius $5.3C$ away from the airfoil and computations in a larger domain with radius $7.3C$ showed

small variation in the pressure distribution. This modest domain size was found to be sufficient to capture the potential flow and this was attributed to the characteristics-based boundary conditions employed by the author. The domain of Shan et al. (2005a) extended $3C$ in the upstream and downstream directions and $4C$ in the cross-stream direction; again a compressible flow solver was used with non-reflective boundary conditions in all boundaries. Zhang and Samtaney (2015b) and Lehmkuhl et al. (2013a) employed larger domains, with radius of $10C$ and $20C$ respectively. Regarding the potential effect of the domain in the calculation of the eigenmodes, Rodríguez and Theofilis (2009) and Kitsios et al. (2008) have used, for a similar flow configuration, again a C-type domain, with radius of $5.0C$ and the outlet located at $6.0C$, which were deemed to be sufficient. In the present work, for the straight trailing edge airfoil, 3D simulations in two domains were performed as mentioned earlier. In the small domain, the inlet boundary is located $6.0C$ upstream of the leading edge, the outlet boundary $4.0C$ downstream of the trailing edge and the spanwise extent was $L_z = 0.1C$ (M1 in table 2.1). In the larger domain, the inlet, top and bottom boundaries are located $18C$ away from the airfoil, the outlet boundary $20C$ downstream of the trailing edge, and the spanwise length is $0.2C$. Comparison between the results obtained from the two domains will be presented later.

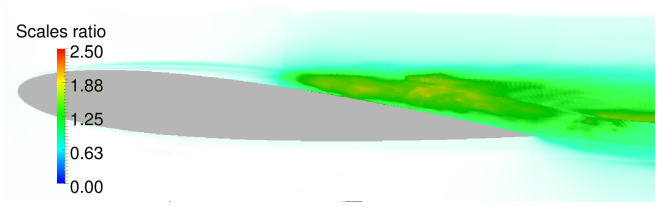
For the blunt trailing edge simulations the spanwise extent was kept at $L_z = 0.2C$ in order to capture the 3D instabilities of the vortices emanating from the blunt trailing edge. These vortices scale with the edge thickness, θ, and are expected to develop 3D instabilities at the Reynolds number examined. Note that the Reynolds number based on θ is 1850, and 3D instabilities develop (at least for the flow around a cylinder) when Re is larger than about 190 (see Williamson (1996)). There are two types of instabilities (termed modes A and B) that have different spanwise length scales (4ϵ and ϵ respectively Williamson (1996)). The spanwise extent of $L_z = 0.2C$ is therefore wide enough to accommodate both instabilities. For the serrated trailing edge airfoil, the spanwise distance was two serration periods i.e. $L_z = 0.532C$.

Grid resolution was very fine close to the airfoil, with 740 nodes around the

surface (with appropriate clustering at the suction side to adequately resolve separation, transition and reattachment), 220 nodes at the wall-normal distance up to $0.15C$ and 500 nodes at the wake up to $2C$ downstream of the trailing edge. The number of layers along the span varied from 100 (for the straight trailing edge) to 140 (for the serrated trailing edge), leading to a total grid size between 50 and 70 million cells. As previously mentioned the grid was carefully designed to minimize the existence of skewed/non-orthogonal cells (see Figure), with the maximum angle between face-normal and centroid vectors between cells being approximately 10^o. The resolution in the wall-normal direction is at worst $\Delta y^+ < 1$ while for the streamwise and spanwise directions is $\Delta x^+ < 10$, $\Delta z^+ < 10$ respectively. The corresponding maximum CFL numbers in the three directions were $CFL_x = 0.30$, $CFL_y = 0.28$ and $CFL_z = 0.02$ After the flow has developed (the boundary layer has separated and the first vortices have reached the outlet), data are collected for a period of up to 40 time units (a time unit is defined as $tu = tU_\infty/C$).



(a) Blunt trailing edge airfoil.



(b) Serrated trailing edge airfoil (plane through the peak).

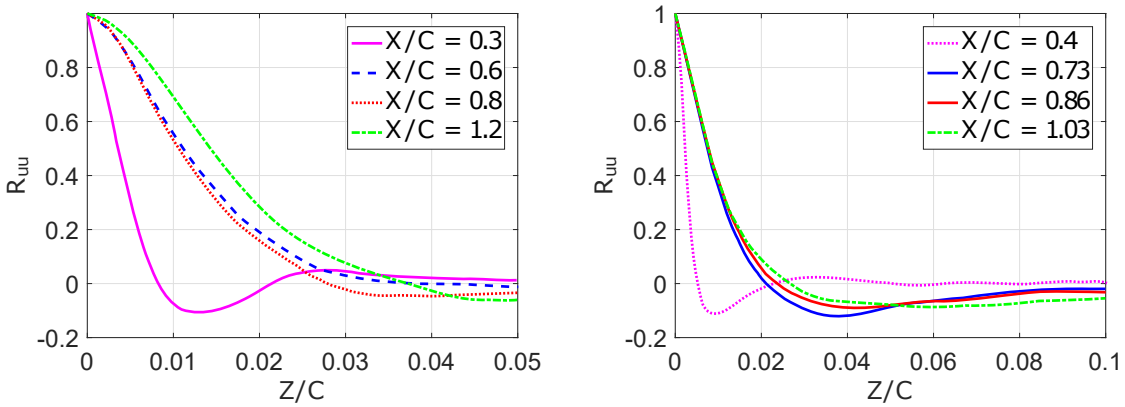
Figure 2.8: Contour plots of the the ratio of the characteristic grid size to the local Kolmogorov scale.

In order to assess the suitability of grid resolution for DNS studies, we computed the ratio of the characteristic cell size (defined as the cubic root of the cell volume) to

the local Kolmogorov length scale i.e. $\frac{\sqrt[3]{V}}{\eta}$. Contour plots for this ratio for the blunt trailing edge and the serrated trailing edge airfoil (in a plane through the peak) are shown in Figure 2.8. It must be mentioned that the cell sizes in the XZ plane are the same for all 3 configurations (there are only minor differences to account for the different trailing edge geometry). As it can be seen, the ratio varies significantly and is maximal in the region of turbulent reattachment and the wake. In the largest part of the domain, the ratio is around 1 (or smaller) and there are very small regions for which the ratio is around 2 or slightly larger (the max value is 2.5). Resolution requirements for a proper DNS have been reported in Moin and Mahesh (1998); Donzis et al. (2008). The latter authors mention that a standard resolution for 2^{nd} order quantities (such as rms velocities or the energy spectrum which takes very small values and falls off rapidly at wavenumbers $k > 1/\eta$) is $\Delta x/\eta \approx 2$. It is expected therefore that the present mesh is sufficiently fine for the results to be true DNS.

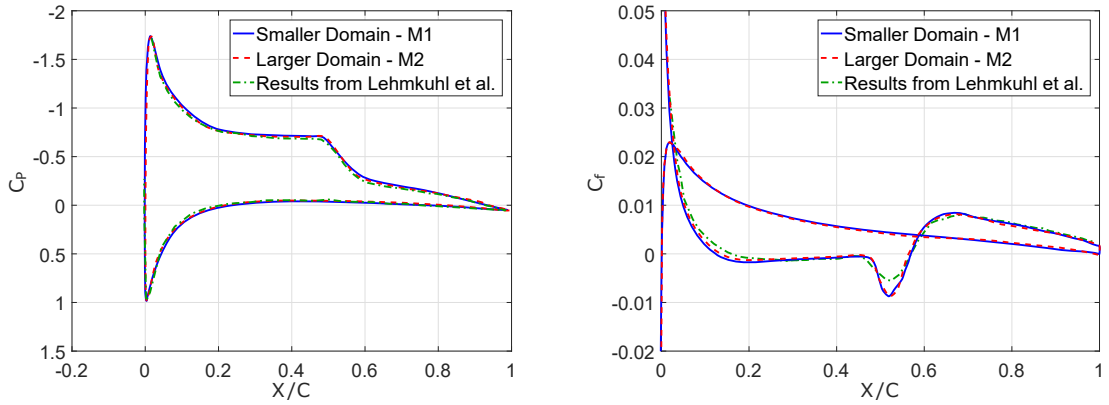
In Figure 2.9, the spanwise autocorrelations of the streamwise velocity, R_{uu}, are shown for the straight (small domain) and the blunt trailing edge airfoil at 4 points (3 inside the boundary layer and 1 in the near wake). The correlation curves depend on the selected point. The best decorrelation for both airfoils is obtained for the most upstream point, which is located before transition. For the other points the values reduce to small values at the middle of the domain. Zhang and Samtaney Zhang and Samtaney (2016a) computed the spanwise correlations for spanwise domain sizes that range from $0.1C - 0.8C$ and found that the results depend not only on the location selected, but also on the velocity component examined.

In Figure 2.10 we compare the computed statistics with available results in the literature for the small and large domain for the straight trailing edge airfoil. The DNS results of Lehmkuhl et al. (2013a) are ideal for such comparison. Figures 2.10a and 2.10b show the distribution of the pressure C_p and skin-friction C_f coefficients along the airfoil surface for the small and large domains. It can be seen that the effect of the domain size (between the two domains tested) is indeed negligible.



(a) Straight trailing edge ($L_z = 0.1C$). (b) Blunt trailing edge ($L_z = 0.2C$)

Figure 2.9: Spanwise autocorrelation functions for the straight and blunt trailing edge airfoils. The first point is in the separation bubble, the 2^{nd} and 3^{rd} points are in the reattached turbulent boundary layer and the last points is in the very near wake. The cross stream coordinates of the points are for clarity mentioned here: for Figure 2.9a $Y/C = 0.038, 0.00037, -0.031, -0.075$ and for Figure 2.9b $Y/C = 0.025, -0.019, -0.041, -0.062$ going from the first to last point.



(a) Pressure coefficient C_p. (b) Skin friction coefficient C_f.

Figure 2.10: Comparison between the current results for C_p and C_f coefficients and the DNS results from Lehmkuhl et al.Lehmkuhl et al. (2013a) .

As far as the comparison between the present results and those of Lehmkuhl et al. (2013a) is concerned, there are some small discrepancies, especially in the C_f coefficient, but overall the match is reasonably good. The shape of the C_p profiles is very similar to that measured experimentally for laminar separation bubbles with

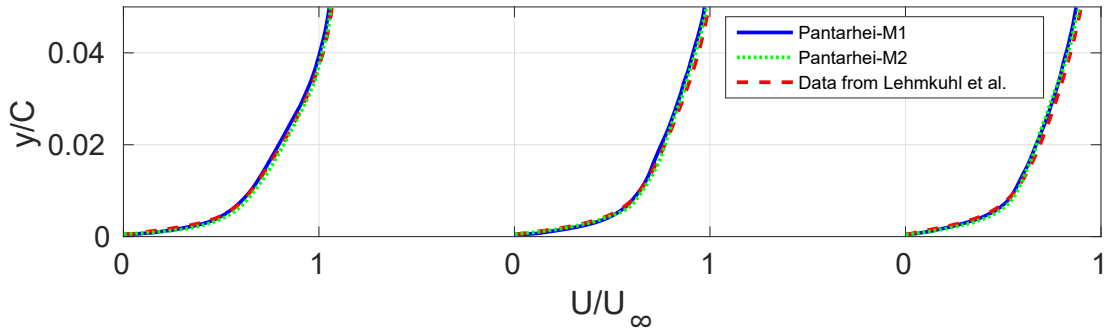
	X_{sep}	X_{re}	C_L	C_D
Present	$0.145C$	$0.564C$	0.589	0.0271
Zhang and Samtaney (2016a)	$0.141C$	$0.58C$	0.562	0.0282
Lehmkuhl et al. (2013a)	$0.169C$	$0.566C$	0.569	0.0291

Table 2.2: Comparison of time-averaged lift and drag coefficients C_L, C_D and separation and reattachment points X_{sep},X_{re}.

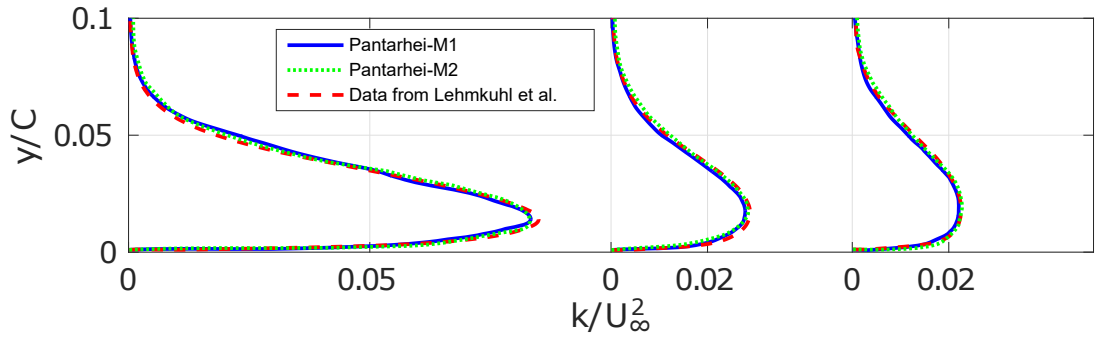
transition followed by reattachment (see O'Meara and Mueller (1987); Boutilier and Yarusevych (2012); Yarusevych et al. (2006). O'Meara and Mueller (1987) identify the location of separation as the start of the constant-pressure region (also known as pressure plateau), the free shear layer transition point as the end of the plateau, and the reattachment as the point at which pressure recovery exhibits a sharp decrease. These observations are broadly consistent with the C_p and C_f plots. The pressure plateau appears to start a little downstream of the separation point, while the reattachement point matches with the position at which the rate of pressure recovery changes. Inspection of the Reynolds stress distributions (shown in the left column of figure 3.4) indicates that transiton starts at around $X/C = 0.45$, slightly upstream of the end of the pressure plateau. The skin friction has very small values inside the recirculation region upstream of transition, which is consistent with the dead air region of Horton (1968). Following transition, C_f reaches a minimum negative value, indicative of the reverse flow vortex Horton (1968). Increased momentum transfer due to turbulent mixing eventually eliminates the reverse flow and the flow reattaches at $X/C = 0.564$.

The separation and reattachment points as well as the force coefficients computed in the present work are compared with those from two other studies in Table 2.2. There is good agreement with previously reported results. Small discrepancies do exist, but it must be borne in mind that the transition and reattachment locations are very sensitive to the numerical discretisation and mesh resolution. The lift and drag coefficients are also in reasonably good agreement with the results of Lehmkuhl et al. (2013a) and Zhang and Samtaney (2016a).

Figures 2.11a and 2.11b show the variation of streamwise velocity and turbulent kinetic energy across the boundary layer at three locations after reattachment (results obtained using the smaller domain). The profiles are compared with those of Lehmkuhl et al. (2013a) and again very good agreement is observed.



(a) Streamwise velocity profiles at 3 locations (from right to left $X/C = 0.7$, 0.8 and 0.9).



(b) Turbulent kinetic energy profiles at the same X/C locations.

Figure 2.11: Comparison of profiles across the boundary layer.

In Figure 2.12 instantaneous iso-surfaces of the Q criterion are shown for visualization of the flow separation and transition. The Q criterion was introduced by Jeong and Hussain (1995) for visualisation of a vortex and it is defined as $Q = \frac{1}{2}(||\mathbf{\Omega}||^2 - ||\mathbf{S}||^2)$, where $\mathbf{\Omega}$ and $\mathbf{S}$ are rotation and strain rate tensors respectively. When $Q > 0$ the rotation rate dominates the strain rate, and serves as a way to identify a vortex core. The periodic formation and break up of Kelvin-Helmholtz vortices is clearly seen in the figure. The break up, at this particular time instant, starts to appear clearly at around $x/C = 0.50$, at the end of the pressure 'plateau' and the start of the rapid pressure recovery.

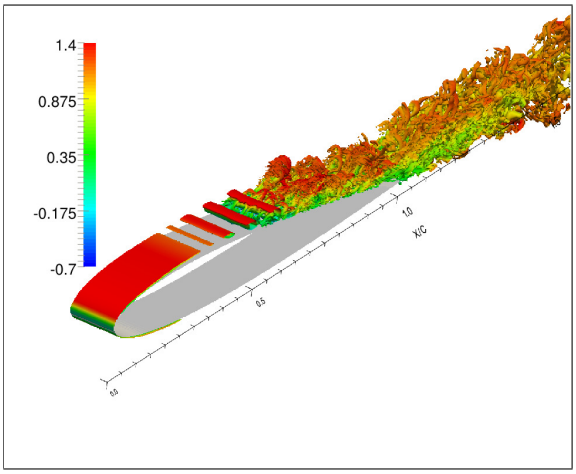


Figure 2.12: Q contours in the range $[20, 100] \times (U_\infty/C)^2$ for the straight trailing edge case. The colorscale values are based on the streamwise velocity.

In the next chapter we explore the physical characteristics of the flow around the three airfoils.

Chapter 3

Interaction between the flow field and the trailing edges

3.1 Introduction

In this chapter[1] we investigate the interaction of the separated shear layer with the trailing edge for the 3 airfoils of section 2.4.1. This investigation will be performed with the aid of a known model reduction method, the dynamic mode decomposition (DMD).

In the current work we use the Dynamic Mode Decomposition (DMD) method proposed by Schmid (see Schmid et al. (2011); Schmid (2010)). The method provides a set of modes, each having a characteristic frequency. The temporal and spatial variations are therefore fully coupled. This method is more suitable than POD for the flow fields examined in the present work, which are characterized by a set of few fundamental frequencies. It is therefore possible to extract directly the structures that oscillate at these frequencies. A brief description of the algorithm will be presented below, but for a more rigorous treatment we refer the reader to the original works by Schmid et al. (2011) and Schmid (2010) and the analysis of Jovanović et al.

[1]The results of this chapter have appeared in the paper: Thomareis, N. and Papadakis, G. (2017). Effect of trailing edge shape on the separated flow characteristics around an airfoil at low Reynolds number: A numerical study. *Physics of Fluids*, 29(1):014101.

(2014). The review paper of Bagheri (2012) provides a more general discussion on model reduction methods.

3.1.1 Derivation of the Dynamic Mode Decomposition formulas

The DMD method was applied in the straight and blunt trailing edge airfoils in which the dominant instabilities (shear layer shedding and Karman shedding from the blunt trailing edge) consist of spanwise elongated structures which allows a 2D application of the method. The data used for these cases where the u and v velocity components at a plane of constant Z. Attempts were made to apply the method in 2D cuts in the serrated trailing edge, but, as we will see in this chapter, the three dimensionality of the developing instabilities (especially from the serrated trailing edge) rendered the 2D method insufficient. We assume a series of N time snapshots of the velocity field separated by Δt, $\mathbf{X}_1^N = \{\mathbf{v}_1, \mathbf{v}_2, ..., \mathbf{v}_N\}$. Each vector $\mathbf{v}_i$ is a column with the field data under consideration. We assume that each vector $\mathbf{v}_i$ has size M, with $M \gg N$. The method assumes a linear dependence between consecutive snapshots of the form:

$$\mathbf{v}_{i+1} = \mathbf{A}\mathbf{v}_i, \tag{3.1}$$

where $\mathbf{A} \in \mathbb{R}^{M \times M}$ is the underlying (unknown) constant system matrix that describes the dynamic behavior of the system. If the differential evolution equation for variable $\mathbf{v}$ is $\frac{d\mathbf{v}}{dt} = \mathbf{B}\mathbf{v}$ then $\mathbf{A} = e^{\mathbf{B}\Delta t}$ and the aim of DMD is to extract the eigenvalues and eigenvectors of matrix $\mathbf{B}$ using the field snapshots. If we define matrix $\mathbf{X}_1^{N-1} = \{\mathbf{v}_1, \mathbf{v}_2, ..., \mathbf{v}_{N-1}\} \in \mathbb{R}^{M \times (N-1)}$ then because of (3.1):

$$\mathbf{X}_1^{N-1} = \{\mathbf{v}_1, \mathbf{A}\mathbf{v}_1, \mathbf{A}^2\mathbf{v}_1, ..., \mathbf{A}^{N-2}\mathbf{v}_1\}. \tag{3.2}$$

Combining (3.1) and (3.2) we get

$$\mathbf{X}_2^N = \mathbf{A}\mathbf{X}_1^{N-1}, \tag{3.3}$$

where $\mathbf{X}_2^N = \{\mathbf{v}_2, \mathbf{v}_3, ..., \mathbf{v}_N\}$. Finding matrix $\mathbf{A}$ then amounts to solving the under-determined systems defined by equation (3.3)[2], as an optimization problem. Such solutions can be expressed in the form:

$$\mathbf{A} = \mathbf{X}_2^N \left(\mathbf{X}_1^{N-1}\right)^+. \tag{3.4}$$

The exponent + above denotes the pseudo-inverse. The calculation of the pseudo-inverse can be performed using the singular value decomposition (SVD) of $\mathbf{X}_1^{N-1}$ according to which $\mathbf{X}_1^{N-1} = \mathbf{U}\mathbf{\Sigma}\mathbf{V}^\dagger$ († denotes the conjugate transpose of a matrix). $\mathbf{\Sigma}$ is a diagonal $(r \times r)$ matrix that contains the r non-zero singular values of $\mathbf{X_1^{N-1}}$(i.e. r is the rank of $\mathbf{X}_1^{N-1}$) and $\mathbf{U}$ and $\mathbf{V}$ are matrices with orthonormal columns ($\mathbf{U}^\dagger\mathbf{U} = \mathbf{I}$ and $\mathbf{V}^\dagger\mathbf{V} = \mathbf{I}$) and dimensions $(M \times r)$ and $((N-1) \times r)$ respectively.

The SVD has been extensively used for finding optimal solutions for under-determined problems, by effectively using a lower order approximation of the system matrix. Since the system matrix of an under-determined system will always have fewer rows than columns, it will always be $r \leq N < M$, and thus the left singular values (i.e. the columns of matrix $\mathbf{U}$) are used for this purpose. In the present case, we get from equation (3.4):

$$\begin{aligned} &\mathbf{A} = \mathbf{X}_2^N \left(\mathbf{X}_1^{N-1}\right)^+ \Rightarrow \\ &\mathbf{A} = \mathbf{X}_2^N \mathbf{V}\mathbf{\Sigma}^{-1}\mathbf{U}^\dagger \Rightarrow \\ &\mathbf{U}^\dagger\mathbf{A}\mathbf{U} = \mathbf{U}^\dagger\mathbf{X}_2^N\mathbf{V}\mathbf{\Sigma}^{-1}, \end{aligned} \tag{3.5}$$

[2]Equation (3.3) effectively defines M systems, each one having as system matrix $\left(\mathbf{X}_1^{N-1}\right)^\dagger \in \mathbb{R}^{(N-1)\times M}$, and as input vector each of the M the rows of $\mathbf{X_2^N}$, thus it is not solvable in the traditional sense.

where the last step is effectively the projection of the columns of matrix $\mathbf{A}$ onto the basis spanned by the left singular values of $\mathbf{X_1^{N-1}}$. If we now set $\mathbf{F} = \mathbf{U}^\dagger\mathbf{A}\mathbf{U}$ then the matrices $\mathbf{A}$ and $\mathbf{F}$ will be similar and the eigenvalues of $\mathbf{F}$ will approximate the eigenvalues of $\mathbf{A}$. Also, an eigenvector $\mathbf{y}_i$ of $\mathbf{A}$ will be given by $\mathbf{y}_i = \mathbf{U}\boldsymbol{\phi}_i$, where $\boldsymbol{\phi}_i$ is an eigenvector of $\mathbf{F}$. From the defining relation of $\mathbf{F}$ it is straightforward to see that its dimensions will be at most $N \times N$ and thus the calculations of its eigenvalues and eigenvectors can be accomplished much more efficiently.

The reconstructed flow field $\tilde{\mathbf{v}}_j$ $(j = 1 \dots N-1)$ will then be given by:

$$\tilde{\mathbf{v}}_j = \sum_{i=1}^{r} \mathbf{y}_i \ (\lambda_i)^j \ \alpha_i, \tag{3.6}$$

where α_i is the amplitude of the i-th mode and λ_i the corresponding eigenvalue of $\mathbf{F}$. In the case where the reconstructed flow field needs to be calculated, the amplitudes α_i need to calculated by solving a second optimization problem (Jovanović et al., 2014).

When applied to a linear system, equation (3.1) is exact. In this case, the computed modes/eigenvalues represent the physically correct structures and their growth rates, frequencies. For non-linear systems, (3.1) represents a best linear map that links all snapshots. If the flow is characterized by periodically repeatable and persistent (i.e. neutrally stable) structures, the DMD method should be able to detect these and the associated frequencies. For these structures, the growth rate (i.e. the magnitude of λ) should be very close to 1, which indicates that they are neutral. A large value of the amplitude, α_i, is not a reliable indicator for the selection of such structures, as it may characterise a mode that will eventually decay. For this reason, the amplitudes α_i are multiplied by $(\lambda_i)^{N-1}$, so that modes with high α_i but $|\lambda_i| < 1$ (i.e. higher damping ratios) are not prominent.

3.2 Results and discussion

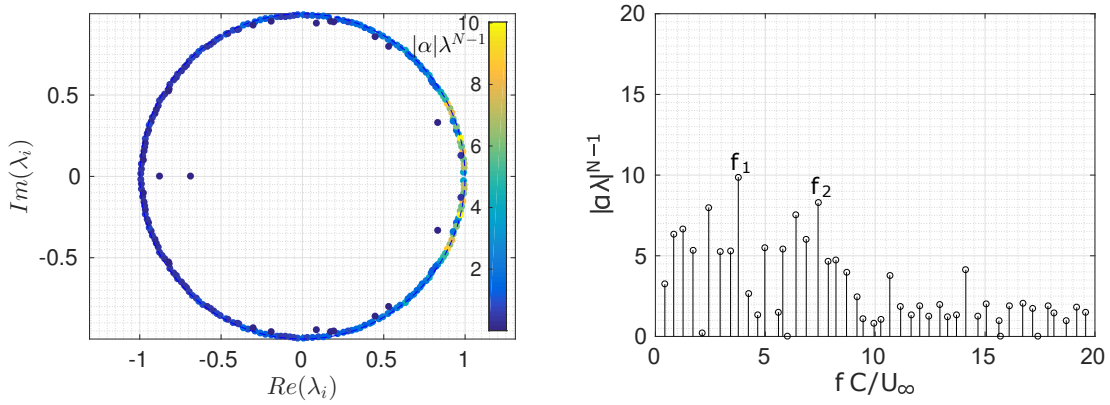
In this section results are presented starting with the straight trailing edge, followed by the flatback and ending with the serrated edge. This order of exposition helps to understand better the process of interaction of the trailing edge with the separating shear layer.

3.2.1 Airfoil with straight trailing edge

The DMD method was applied on a plane of constant Z at the mid span, in an $X-Y$ window with dimensions $[-0.2, 2] \times [-0.27, 018]\, C$. In total $N = 300$ time snapshots separated by $\Delta T = 0.01^{C}/_{U_\infty}$ were used. This number of snapshots corresponds to approximately 12 shedding cycles of the smallest dominant frequency of the flow field (the wake shedding as we will shortly see). Higher frequencies will obviously have more periods within this interval. It is thus expected that this number of snapshots is sufficient to capture the dominant dynamics of the flow field. A polar plot of the computed eigenvalues is shown in Figure 3.1a. The modes appear in complex conjugate pairs and the ones with the largest amplitude $\alpha_i \left(\lambda_i\right)^{N-1}$ are marked with yellow colour. Two dominant modes can be identified from the DMD spectrum shown in Figure 3.1b: a low frequency mode located at $f_1 = 3.8$ and a high frequency at $f_2 = 7.4$[3].

In order to verify that these frequencies are indeed present and they are dominant, velocity time-signals from two different locations at the mid span were analysed: one on the suction side of the airfoil at $X/C = 0.53, Y/C = 0.032$ (inside the transitioning shear layer but upstream of reattachment) and one in the wake at $X/C = 2.0, Y/C = -0.17$. In Figures 3.2a and 3.2b the power spectral density of the cross-stream velocity is plotted. The velocity signal at the first point (Fig. 3.2a) shows a peak at the high frequency f_2 observed in Figure 3.1b. Note that

[3]All the frequencies in this text have been normalised by the airfoil's chord and streamwise velocity, unless stated otherwise.



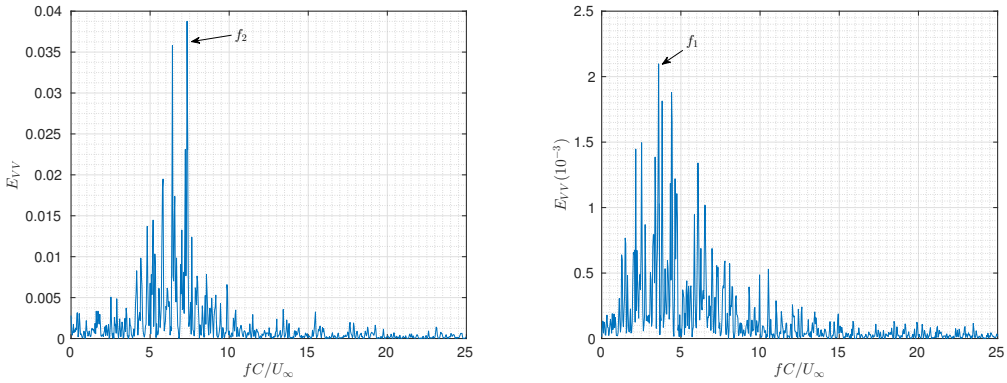
(a) Polar plot of the eigenvalues of each mode (color coded with the scaled amplitude).

(b) Scaled amplitude distribution against frequency of the DMD modes.

Figure 3.1: Amplitude distribution of the eigenvalues calculated from the DMD algorithm.

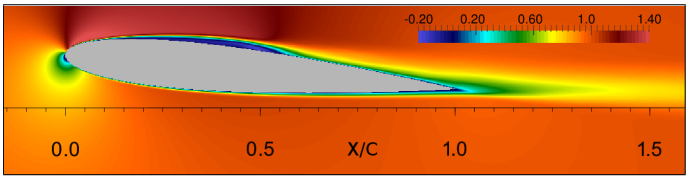
in Figure 3.2a the horizontal axis is linear and re-plotting using logarithmic axis (figure not shown) reveals that the energy content of the signal is distributed among a range of frequencies, centered around a broad peak at frequency f_2. Such a broad peak has also been observed experimentally (Yarusevych et al., 2009; Boutilier and Yarusevych, 2012) and is due to the fact that the shear layer amplifies a broad range of frequencies (Ho and Huerre, 1984). Similarly, the velocity signal at $X/C = 2.0$ (Figure 3.2b), shows a dominant peak located at the lower frequency f_1; again this is a broad peak due to the fact that the point is immersed in a turbulent wake.

The spatial structure of the two most dominant modes as well as the time averaged streamwise velocity field are depicted in Figure 3.3. In the time averaged field, shown in Figure 3.3a, a thin recirculation zone can be clearly seen on the suction side of the airfoil. The high frequency, $f_2 = 7.4$, is associated with the Kelvin-Helmholtz instability triggered by the inflectional velocity profile across the separating shear layer (Dovgal et al., 1994). As Figure 3.3b shows, this mode is dominant in the separating shear layer, approximately between $X/C = 0.4 - 0.8$. In the region where it is most dominant, the shear layer rolls up and sheds vortices, as shown in Figure 2.12.

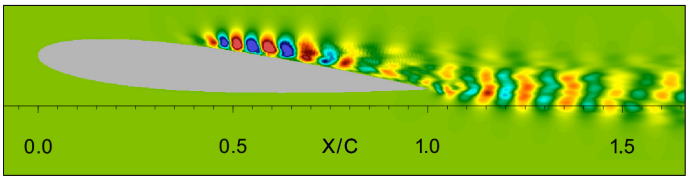


(a) (b)

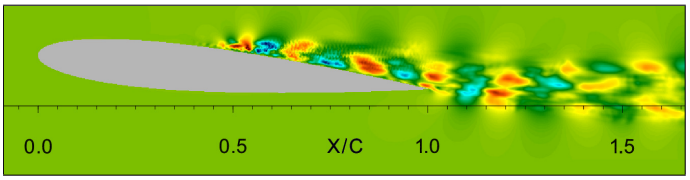
Figure 3.2: Power spectral density of the cross stream velocity component V at two different locations, $X/C = 0.53C, Y/C = 0.032$ (a) and $X/C = 2.0C, Y/C = -0.17$ (b).



(a) Streamwise component of the mode corresponding to the mean flow.



(b) Cross-stream component of the mode at f_2.

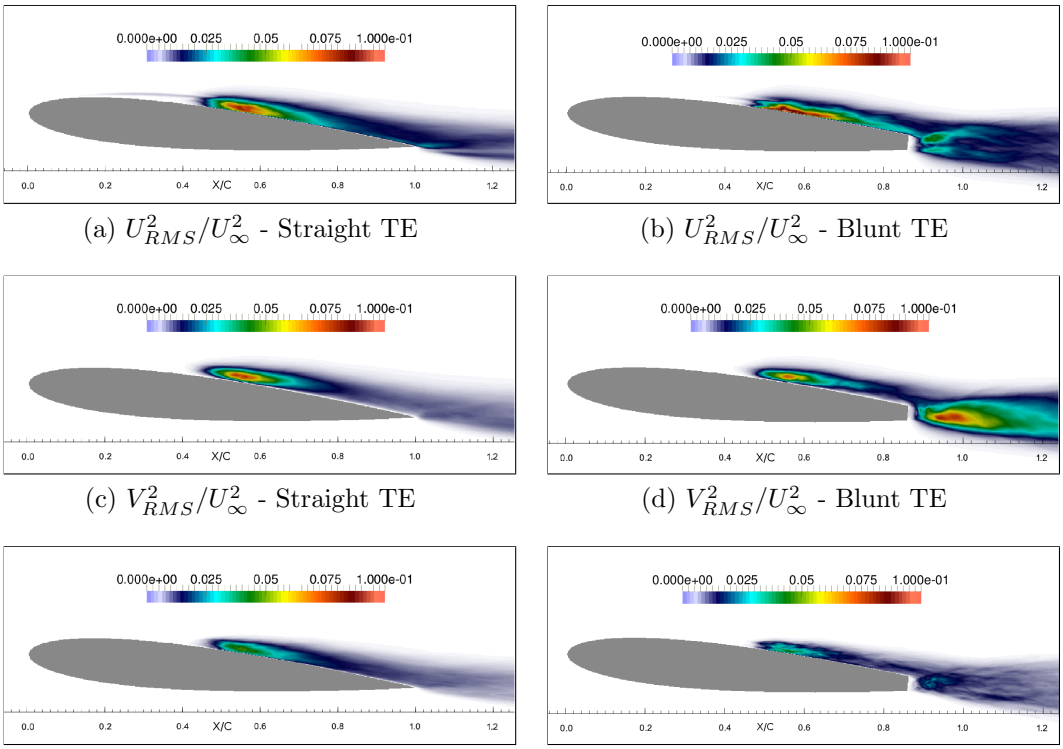


(c) Cross-stream component of the mode at f_1.

Figure 3.3: Time-averaged streamwise velocity field (Figure 3.3a) and two most dominant DMD modes for a straight trailing edge (Figures 3.3b and 3.3c).

It is difficult to compare directly this frequency against results from the literature because the flow conditions are different. For example, Jones (2008) performed one-dimensional spatial stability analysis on a number of time-averaged velocity profiles along the suction side for the same airfoil, angle of attack and Reynolds number, but with Mach number equal to 0.4, which makes compressibility effects non-negligible. The frequency with the strongest spatial growth slightly changes from one profile to the other, but overall the most amplified frequency in the shear layer was found to be $f = 8.49$, which is close to the present f_2. The difference can be attributed to two reasons: firstly, Jones's analysis is one-dimensional and is based on the Orr-Sommerfeld equation and, secondly, compressibility effects are expected to become more important in the area of high acceleration around the leading edge and therefore affect the velocity distribution of the separating shear layer and the most amplified frequencies. Boutilier and Yarusevych (2012) examined the flow around a NACA 0018 at Re=100,000 and they also performed one-dimensional stability analysis using the measured time-averaged profiles. For the 5^o angle of attack, the dominant frequency was found to be 13.0 (table II in their paper). The difference with the present work can be attributed to the different Reynolds number (there is a power law dependency of the shear layer frequency and Reynolds number Yarusevych et al. (2006)) and the different thickness of the airfoil that affects the velocity distribution in the suction side.

The predicted frequency, f_2, however is in agreement with previous results when non-dimensionalized with the appropriate length and velocity scales. Huang and Ho (1990) and Yarusevych et al. (2009) have identified the streamwise distance of the shed vortices, ψ_0, and the velocity at the edge of the boundary layer at the point of separation, U_{es}, as the relevant length and velocity scales respectively. The distance ψ_0 can be directly estimated from the spatial structure of the DMD mode (Figure 3.3b) and it is found to be $\psi_0 \approx 0.08C$, while $U_{es} = 1.4U_\infty$. The corresponding non-dimensional frequency is $f_2^* = f_2\psi_0/U_{es} \approx 0.44$, very close to the observed range of



(a) U^2_{RMS}/U^2_∞ - Straight TE

(b) U^2_{RMS}/U^2_∞ - Blunt TE

(c) V^2_{RMS}/U^2_∞ - Straight TE

(d) V^2_{RMS}/U^2_∞ - Blunt TE

(e) W^2_{RMS}/U^2_∞ - Straight TE

(f) W^2_{RMS}/U^2_∞ - Blunt TE

Figure 3.4: Streamwise, cross-stream and spanwise Reynolds stress distributions for the straight and blunt trailing edge airfoils.

values $0.45 - 0.5$ (Yarusevych et al., 2009).

It is known that as the amplitude of the perturbation grows spatially, non-linear interactions result in a lower frequency, which is a subharmonic of the fundamental instability frequency (for the mechanism of the generation of the subharmonic refer to the review paper by Ho and Huerre (1984) and references therein). The DMD method captures a low frequency at $f_1 = 3.8$. The footprint of this frequency is shown in Figure 3.3c. The mode is activated at $x \approx 0.45C$ (slightly downstream compared with the high frequency mode) and is seen to be present in the reattaching shear layer and the near wake, before decaying slowly further downstream. This frequency is indeed very close to the subharmonic of the fundamental frequency $f_2/2 = 3.7$ (the difference is 2.7%).

In the left column of Figure 3.4 contour plots of the three normal components

of the Reynolds stresses are shown. The same color scale is used to facilitate comparison of the plots. Rapid growth of fluctuations starts at about $X/C = 0.45$ indicating transition to turbulence, as already mentioned. Shortly afterwards is the location of the start of rapid pressure recovery shown in the C_p plot (Figure 2.10a) and the location of the minimum value of the skin friction (Figure 2.10b). Close to the reattachment point ($X/C = 0.56$) all three normal components attain very large values. After the peak, the Reynolds stresses decay downstream. Note also that strong spanwise velocity fluctuations appear denoting the rapid 3D breakdown of the vortices. Two dimensional simulations for this Reynolds number and angle of attack therefore do not describe accurately the flow.

3.2.2 Airfoil with blunt trailing edge

The DMD method was applied again on the mid-span plane in the same $X - Y$ window as in the straight trailing edge case i.e. $[-0.2, 2] \times [-0.27, 0.18]\, C$. In total 240 time snapshots, separated by $\Delta T = 0.01 {}^{C}/_{U_\infty}$, were used, which correspond to 11 shedding cycles. The DMD spectrum in this window is shown in Figure 3.5. One very dominant frequency appears at $f_{bl,1} = 4.5$. Its first harmonic at $f_{bl,3} = 2f_{bl,1}$ also appears. The shear layer natural frequency identified previously is still present at $f_{bl,2} = 7.5$, albeit highly attenuated. It is clear that the truncation of the trailing edge affects significantly the separating shear flow and its frequency content; this interaction will be examined in more detail below.

In Figure 3.6a contour plots of time-averaged streamwise velocity are shown. The flow in the suction side is qualitatively similar compared to the straight trailing edge airfoil: laminar separation, transition to turbulence, and reattachment. The locations of the separation and reattachment points are, however, different (at $0.23c$ and $0.58c$ respectively compared to $0.145c$ and $0.564c$ for the straight trailing edge) leading to a net reduction of the recirculation zone size. The most striking difference in the mean flows between the two airfoils is in the near wake: the presence of

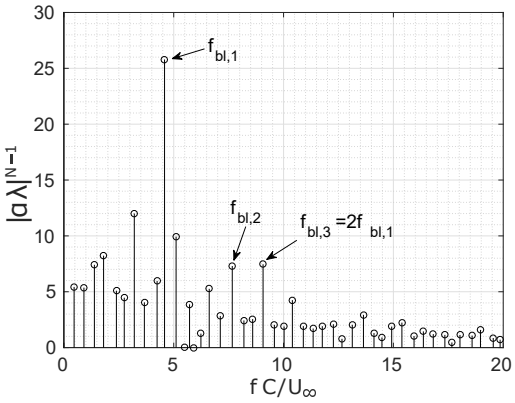
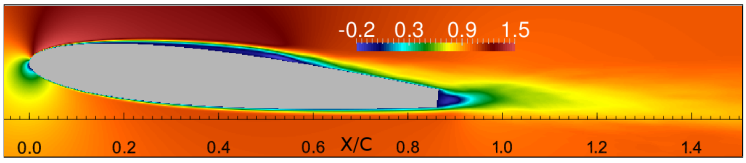
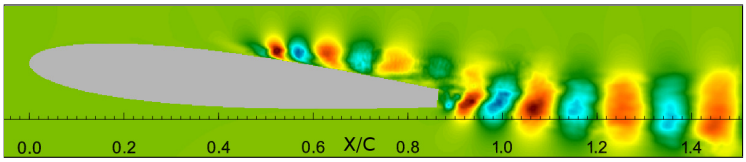


Figure 3.5: DMD spectrum of the flow field around the blunt trailing edge airfoil.



(a)



(b)

Figure 3.6: Contour plots of the time-averaged velocity field U/U_∞ (3.6a) and the most dominant flow mode (3.6b) at $f_{bl,1}$.

bluntness creates a small recirculation zone, which is absent in the straight airfoil case.

Inspection of Figure 3.7 demonstrates that the pressure distribution in the separating shear layer is also different. The minimum C_P is -1.72 for the straight trailing edge, and -1.59 for the blunt trailing edge. To identify the origin of this difference, potential flow simulations with Xfoil (Drela and Youngren, 2001) were performed and exactly the same behavior was observed; the origin therefore is inviscid. This difference has been also observed in the past by Chen and Agarwal (2012) and it is a direct effect of the truncation of the trailing edge, which increases the radius of curvature of the leading edge in relation to the chord length.

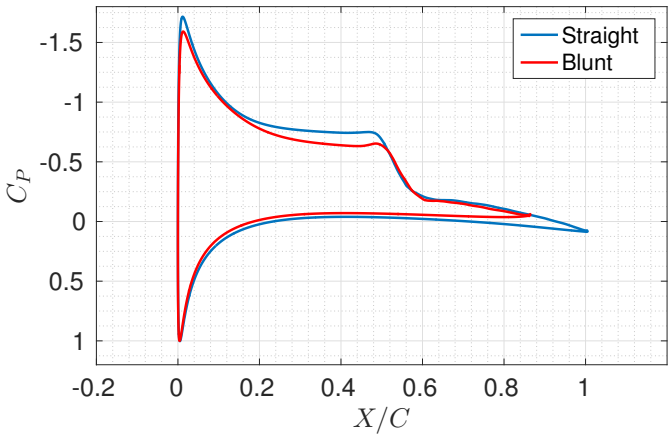


Figure 3.7: Comparison of the pressure coefficients for the straight and blunt trailing edge cases.

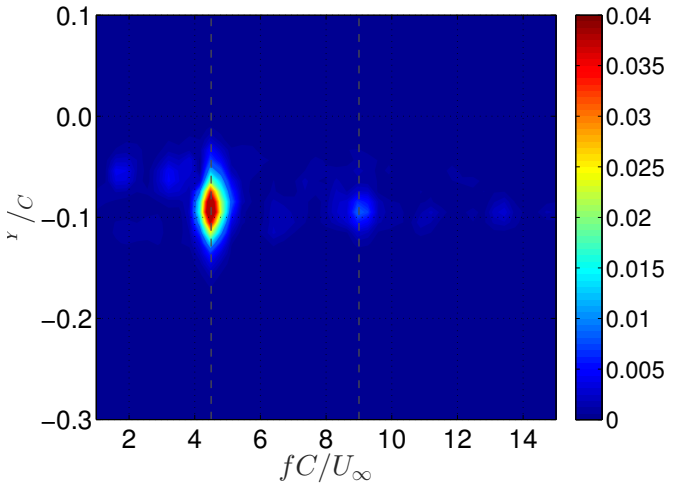
Coherent structures originating from the truncated part of the airfoil are clearly illustrated in Figure 3.6b. This mode, corresponding to the frequency peak $f_{bl,1} = 4.5$, is characteristic of bluff body von Karman vortex shedding. Well-organized structures are shed from the truncated part of the airfoil and convect downstream without significant attenuation, at least in the current field of view. The Strouhal number of this mode based on the trailing edge bluntness and the free stream velocity is $St_{bl,1} = 0.17$. The Strouhal number measured by Nedić and Vassilicos (2015) was 0.189 for an identical geometry but with the chord based Reynolds number three times higher ($Re = 150,000$) and without laminar separation (both boundary layers were tripped). Krentel and Nitsche (2013) found the shedding Strouhal number to be 0.2, but the Reynolds number based on the trailing edge thickness was $44,000$, more than an order of magnitude higher compared to the one in the present paper ($1,850$). Although this mode has the strongest presence in the wake, it's footprint extends far upstream in the suction side of the airfoil, as can be seen in Figure 3.6b. This is not surprising. The wake shedding is the result of a global flow instability and therefore present in the whole flow field. This wake mode is therefore partially collocated with the separating shear layer and provides an excitation (forcing) to it. This has important implications as will be discussed below.

In order to confirm the dominance of the peaks identified in the DMD spectrum, Fourier analysis of the time signals from various probe points in the wake and the suction boundary layer was performed. In Figure 3.8, contour plots of the PSD of the cross-stream velocity spectra are plotted for three different streamwise locations. A strong peak can be identified at $f_{bl,1} = 4.5$, along with a weaker peak at the first harmonic $2f_{bl,1}$. These peaks are observed behind the trailing edge, they are elongated in the Y direction, are strongest close to the airfoil and attenuate downstream.

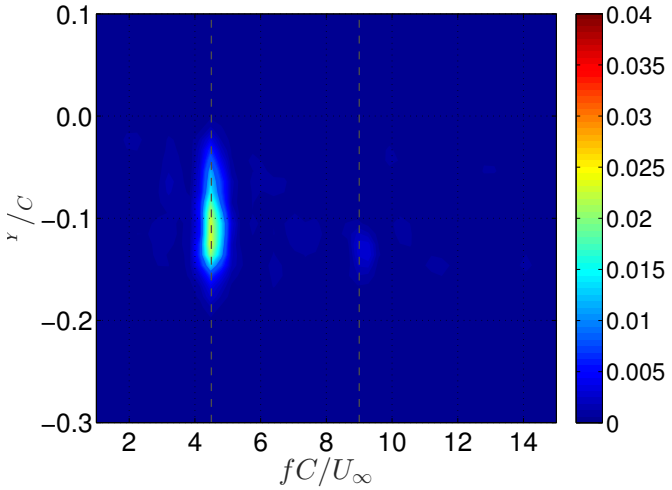
In Figure 3.9 the spectra at 6 points in the suction side boundary layer are plotted. A clear peak can be observed again at $f_{bl,1}$ at all locations. The maximum amplitude appears at Point B, inside the transitioning shear layer.

Both DMD and the spectra reveal a pronounced peak associated with the shedding frequency and it's harmonic. A third peak, with relatively reduced amplitude, can be observed in Figures 3.5 and 3.9 at frequency $f_{bl,2} = 7.5$. This peak is very close to the frequency $f_2 = 7.4$ of the straight trailing edge case and corresponds to the natural shear layer instability. Indeed, using the same length and velocity scales for the non-dimensionalisation of the shear layer shedding frequency, which for the blunt airfoil are $\psi_0 \approx 0.075C$ and $U_{es} = 1.34U_\infty$ respectively, the corresponding non-dimensional frequency $f^* = f_{bl,2}\psi_0/U_{es} \approx 0.42$, which is again close, albeit slightly below, the range of observed values (Yarusevych et al., 2006). Despite the presence of the natural instability, the shedding mode at $f_{bl,1} = 4.5$ is significantly more dominant, both in the DMD spectrum (Figure 3.5) and in the point spectra in the wake and suction side of the airfoil (Figures 3.8 and 3.9 respectively).

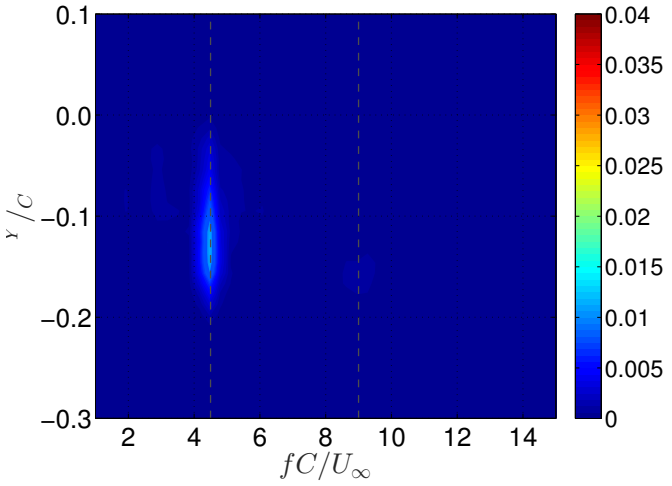
In order to investigate in more detail the behavior of the separating shear layer, the DMD method was applied on a smaller window on the suction side of the airfoil (see Figure 3.10b). The corresponding spectrum is shown in Figure 3.10a. Peaks at the same frequencies as in the spectrum of Figure 3.5 can be identified. The spatial structure of the mode corresponding to the peak at $f_{bl,1}$ is shown in Figure 3.10b. Distinct vortices originating from the separated shear layer can be identified.



(a) Spectrum at $X/C = 1.05$.



(b) Spectrum at $X/C = 1.4$.



(c) Spectrum at $X/C = 2.0$.

Figure 3.8: Spectra for the blunt trailing edge airfoil for different cross stream ($Y/C\big[-0.3, 0.1\big]$) and streamwise ($X/C = 1.05,\ 1.4,\ 2.0$) locations.

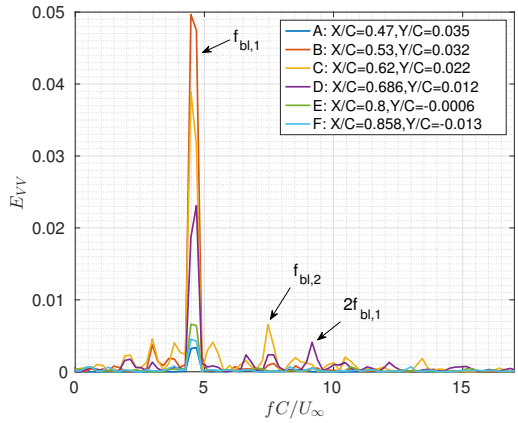
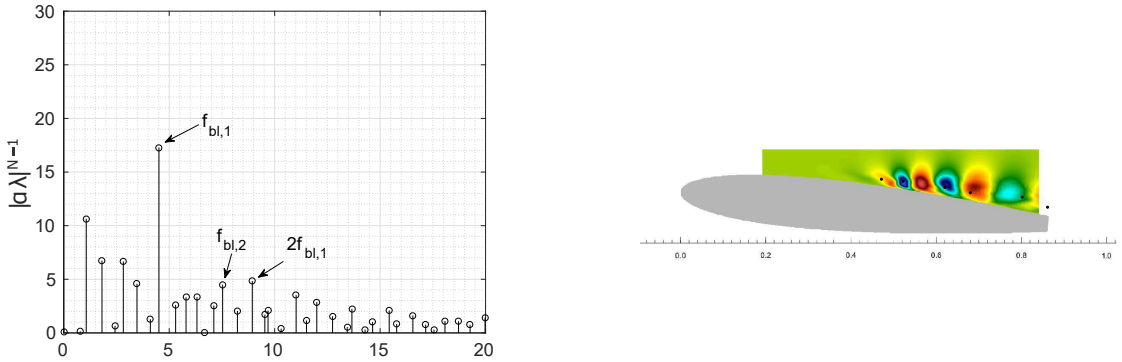


Figure 3.9: Cross stream velocity spectra for 6 different locations (indicated with black dots in Figure 3.10b)at the suction side boundary layer, starting from $X/C = 0.47$ up to $X/C = 0.87$.

It appears that the trailing edge shedding affects the response of the shear layer, by forcing it to oscillate and release vortical structures, at the same frequency. In other words, the shear layer is now locked to the shedding.

Previous works in the literature have examined the effect of forcing in the characteristics of separating shear layers but with an entirely different objective, namely that of control of separation. Marxen and Rist (2010) looked at the mean flow deformation of a laminar separation bubble that develops in a flat plate due to harmonic forcing upstream of the bubble. They noticed a reduction in the size of the bubble and a stabilisation of the flow with respect to small linear perturbations. Similar were the findings of Rist and Augustin (2006). Greenblatt and Wygnanski (2000) have written an extensive review on the subject. The difference with the present work is that periodic perturbations aiming at separation control are imposed externally and upstream of the separation bubble. In our case however, they appear naturally due to the vortex shedding from the blunt trailing edge, they are strongest in the near wake, but they have strong upstream influence.

The response of a free shear layer to external forcing has been studied by Ho and Huang (1982), where it was found that the shear layer showed different states of lock-in depending on the ratio f_f/f_n, where f_f is the frequency of the external



(a) (b)

Figure 3.10: DMD spectrum (3.10a) and spatial structure of the mode at $f_{bl,1}$ (3.10b) at the plane capturing the shear layer transition and reattachment. The cross-stream component of the mode is plotted.

forcing and f_n the natural frequency of the shear layer. For our case, this ratio is $4.5/7.5 = 0.6$, i.e the forcing frequency is close to the subhamonic. Ho and Huang (1982) have shown that this ratio is well within the region where the frequency response of the shear layer is expected to be the same as the forcing frequency. This is exactly what we find in our simulations.

Vortex shedding has also appeared in many experiments, however the ratio of the shear layer frequency to the vortex shedding frequency is quite large. For example in the experiments of Yarusevych et al. (2009), for the range of Reynolds numbers for which reattachment occured, this ratio was at least 7. There is one study in which these two frequencies are similar, that of Kotapati et al. (2010). The authors studied a flow configuration with laminar separation, reattachment and vortex shedding. There are however some important differences compared to our case: first, instead of an airfoil, they examined a flat plate with elliptic leading edge and a blunt trailing edge (with thickness 5% of the chord) at zero angle of incidence, and secondly, they induced the laminar separation bubble close to the trailing edge, in the aft one-third of the flat plate. They report a shear layer instability frequency equal to 7.3 (surprisingly close to ours) and a vortex shedding frequency of 5.0 (obtained when there was no separation bubble, again not far from ours). Their 2D simulations

showed that the shear frequency and the shedding locked to a single frequency of 2.9, while we find locking at a larger frequency (equal to 4.5). The explanation for this difference is the following: the authors induced the separation bubble close to the trailing edge (the reattachment point is located at $0.97C$), therefore the effective length scale for the vortex shedding (in essence, the effective thickness seen by the flow) is the sum of the plate thickness and the height of the separating bubble (Kotapati et al., 2010) (equal to $0.037C$ and located at around $0.88C$, as can be observed from their Figure 5). In our case the separation bubble appears in the middle of the airfoil, the flow reattaches at $0.56C$, so the thickness of the bubble does not affect the effective length scale of shedding. In order to confirm that this is indeed the case, we performed an additional DNS simulation in which the boundary layer was tripped numerically at the region $X/C = 0.03-0.04$. The tripping resulted in a quick transition to an attached turbulent boundary layer on the suction side of the airfoil, and the shedding frequency was also 4.5. This confirms that the presence of separation bubble does not affect the shedding frequency, and the latter is due only to the bluntness. The shear layer then locks to the externally imposed frequency and that frequency depends only on the thickness of the trailing edge.

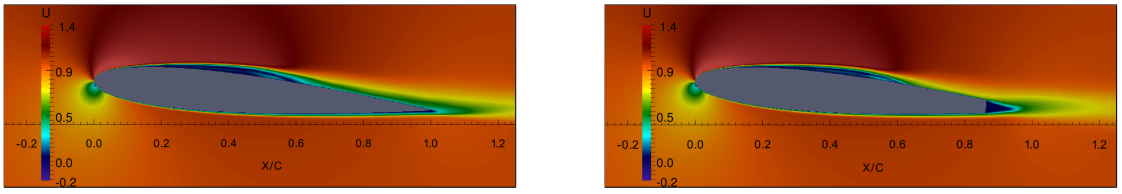
There is one more aspect that needs clarification: Why are the shear layer and shedding frequencies similar, while in the other studies (excluding that of Kotapati et al.) the ratio is significantly higher, as already mentioned? The answer lies in the different length scales that generate the vortex shedding and in the particular value of the Reynolds number examined. More specifically, in the present case the characteristic length scale for the shedding is the trailing edge bluntness and not the thickness of body (as is, for example, in a thick NACA 0025 airfoil (Yarusevych et al., 2009) or in a cylinder (Williamson, 1996)); this has important implications for the shedding frequency. Reducing the characteristic length scale, increases the frequency (in order to keep the Strouhal number constant and relatively independent of the Reynolds number). In our case, the ratio of the trailing edge thickness to that of the airfoil is $\epsilon/t = 0.31$ resulting in a significant larger frequency, close to

the subharmonic of the natural shear layer frequency. The latter has a power-law dependency on the Reynolds number (Yarusevych et al., 2009) and, for the particular Re examined, it attains the value of 7.5, as already mentioned.

The Reynolds stress distributions are shown in the right column of Figure 3.4. The same scale is used for the straight and flatback airfoil. Significant differences are noticed, especially in the near wake. As expected for the flatback airfoil, the Reynolds stress distributions are similar to those created due to vortex shedding behind bluff-bodies. More specifically, the streamwise stress component, U^2_{RMS}, has two peaks close to the top and bottom edge of the blunt trailing edge (confirming that this is the correct length scale to use for the Strouhal number), while a single strong peak appears for the cross-stream component V_{RMS}. Both are results of the periodic formation and detachment of vortices from the top and bottom of surface of the exposed bluntness. A wider area of spanwise fluctuations, W^2_{RMS}, is also observed, which is a direct effect of the wider wake due to the Kármán shedding.

3.2.3 Airfoil with serrated trailing edge

The effect of adding the serrated trailing edge on the flow field will be examined in this section. As will be shown, the flow field in this case is characterized by a three dimensional, secondary flow.



(a) Spanwise plane through the peak.

(b) Spanwise plane through the trough.

Figure 3.11: Time-average streamwise flow fields through the peak and trough planes.

Attention is focused first on the characterisation of the spanwise inhomogeneity of the time-average flow. The streamwise flow fields at two planes (through the peak

and the trough) are shown in Figure 3.11. The flow patterns in these two planes resemble the patterns around a straight and blunt trailing edge respectively.

Although not immediately evident from Figure 3.11 because of the color scale used, close examination of the velocity field in the near wake reveals an unexpected behaviour. Figure 3.12 shows profiles of velocity magnitude at 4 positions at the same streamwise distance ΔX from the trough and the peak locations. It can be clearly seen that the velocity deficits at the same distance from the airfoil surface are different. Most importantly, the wake deficit downstream of the peak is higher than the deficit downstream of a trough. At the location closest to the trailing edge, at $\Delta X = 0.1C$, the deficit after the peak is approximately 20% higher compared to the deficit after the trough. As ΔX increases, the relative difference diminishes and spanwise homogeneity is observed approximately one chord length downstream of the trailing edge. Due to the presence of bluntness at the trough base, one would expect a higher deficit downstream of the trough, and not the peak, at the same distance from the airfoil. This flow characteristic of the serrated trailing edge has also been observed experimentally by Prigent et al. (2016).

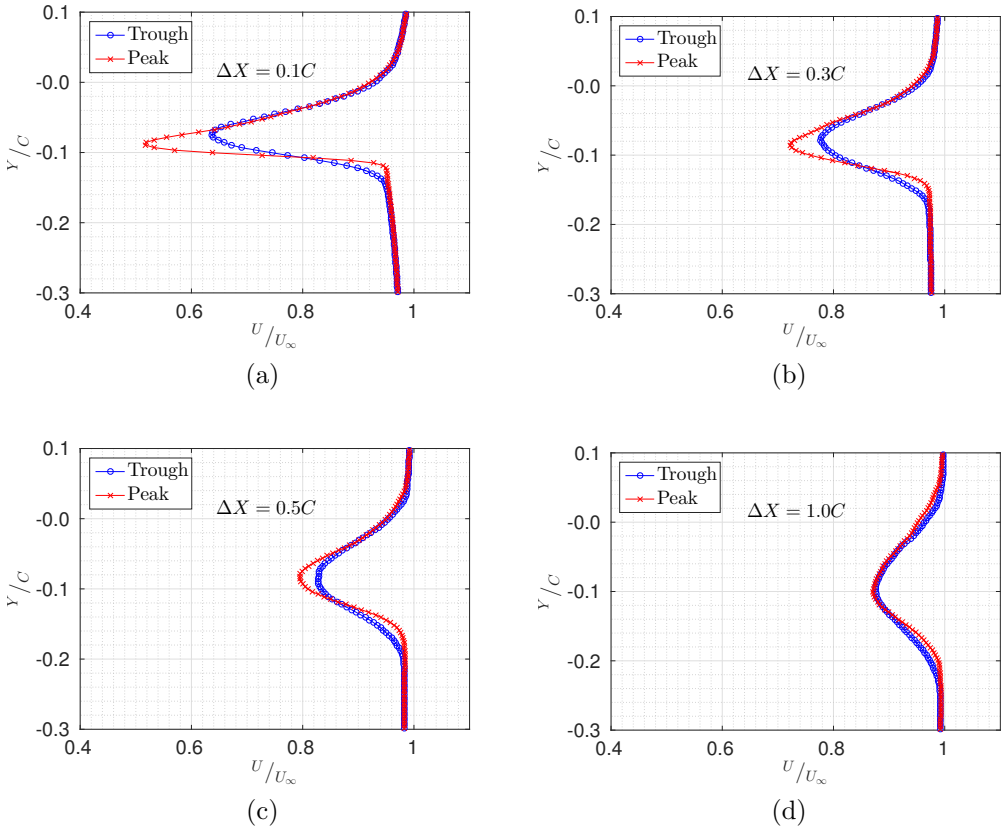
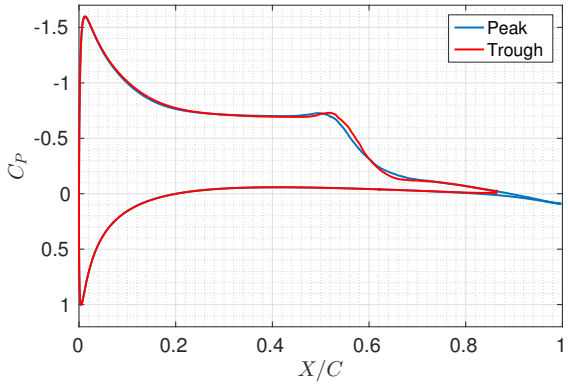
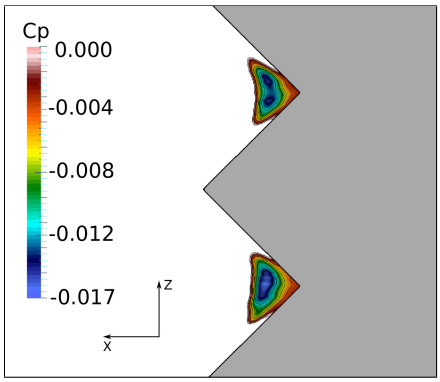


Figure 3.12: Streamwise velocity profile at 4 different positions located at distance ΔX downstream of the trailing edge (ΔX is measured locally along the X direction from the trough and the peak spanwise locations).

In order to explain the flow acceleration behind the trough, we examine first the spanwise variation of the pressure distribution. Figure 3.13a depicts the surface pressure distribution trough the trough and the peak planes. It is clear that the pressure distribution is almost identical in the pressure and the suction side, with only small differences in the separating shear layer. The trailing edges however experience significant pressure difference. The static pressure at the peak is larger compared to the trough by about 10% of the dynamic pressure $\left(\frac{1}{2}\rho U_\infty^2\right)$. The reason for this pressure difference in the spanwise direction is not difficult to explain: after reattachment, the turbulent flow at the peak plane can recover pressure along a larger distance, thereby reaching higher pressure at the trailing edge peak compared to the trough. Pressure varies also slightly inside the trough gaps (by less than 2% of dynamic pressure), as shown in Figure 3.13b.



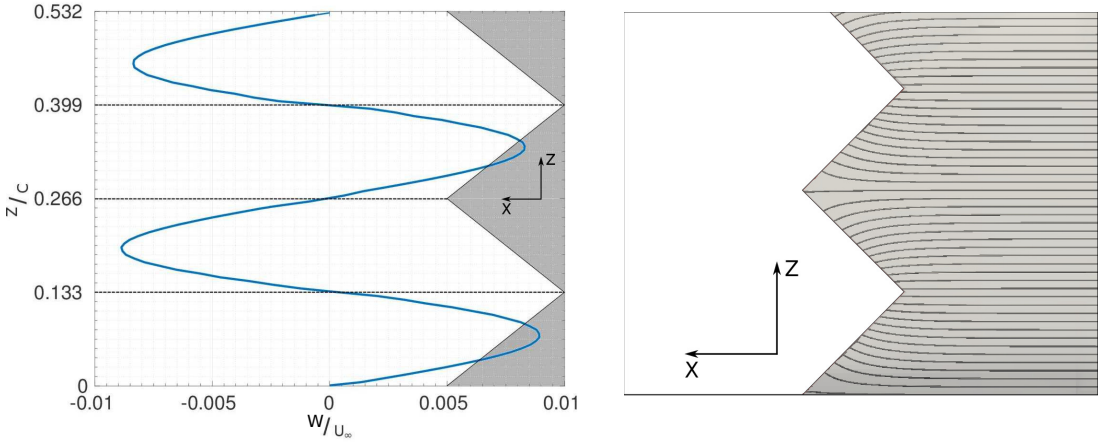
(a) Surface pressure distribution in the trough and peak planes.



(b) Pressure inside the troughs.

Figure 3.13: Pressure distributions on the airfoil surface and inside the troughs.

This spanwise pressure difference is responsible for the development of a secondary flow pattern. More specifically, the spanwise pressure gradient creates an undulating spanwise velocity component, W, as shown in Figure 3.14a. This velocity component is equal to 0 at the trough and peak locations (denoted by the dashed lines in Figure 3.14a) and is maximized in the area in-between. It's value at the specific streamwise location shown is small, but close to the trailing edge increases,



(a) (b)

Figure 3.14: (a) Spanwise velocity component (W) along the span (pressure side of the airfoil, at distance $0.05C$ upstream of the trailing edge trough). The dashed lines indicate the positions where $W = 0$. (b) Time-averaged streamlines at the pressure side of the airfoil.

causing the time-averaged streamlines to bend towards the serration troughs, as illustrated in Figure 3.14b. The drawing in Figure 3.15 shows an illustration of the flow field's behaviour as it bends to enter the area between the serrations' peaks.

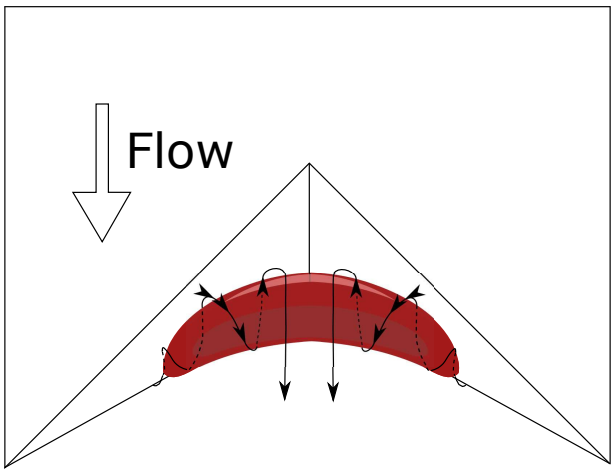
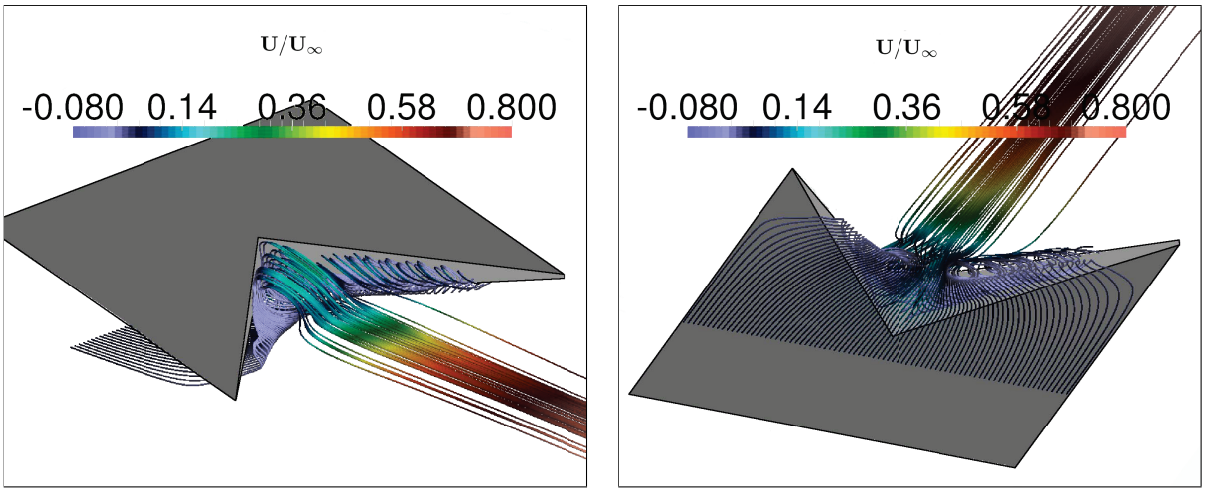


Figure 3.15: Drawing of the flow behaviour inside a serration. The red blob corresponds to the low pressure core forming directly downstream of the trough.

A three dimensional view of the time-averaged streamlines close to the trailing edge is shown in Figure 3.16. The lines are color-coded with the streamwise velocity. The starting points for the generation of streamlines are placed at the pressure side of the airfoil. The streamlines are reminiscent of the flow generated from the wing tip vortices of a finite wing. The low base pressure (due to the finite bluntness) creates a recirculating pattern along at the lip of the serration. The presence of the spanwise pressure variation and the W velocity component results in streamlines that spiral around the recirculation, transporting fluid from the peak to the trough. By virtue of the mass conservation, the flow in the trough is accelerated, thereby providing the mechanism that explains the aforementioned smaller velocity deficit oberved in the near wake.

Spectra are probed along the Y direction from $Y = -0.3C$ to $Y = 0.1C$ in $\Delta Y = 0.01C$ increments at three spanwise locations, directly after the trough, the mid-point and the peak (refer to Figure 3.17).

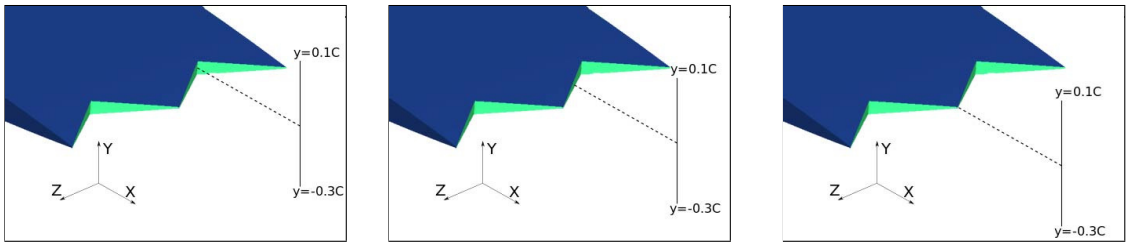
In Figure 3.18 spectra of the V velocity component (in the Y direction) are plotted. Each row corresponds to one spanwise location: directly after the trough, the mid-point and the peak (from top to bottom). Each column corresponds to one streamwise location: very close to the trailing edge at $X = 1.05C$ (left column) and



(a) Seed line placed at the pressure side of the airfoil (Top view)

(b) Seed line placed at the pressure side of the airfoil (Bottom view)

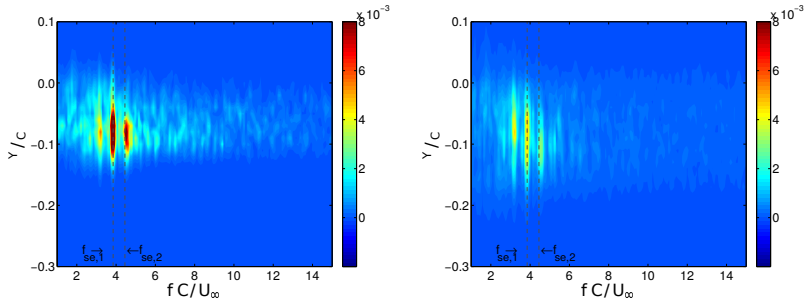
Figure 3.16: Time averaged streamlines, color-coded with the streamwise velocity U/U_∞.



(a) (b) (c)

Figure 3.17: Probing lines and their corresponding spanwise locations after the trough (a), the mid point (b) and the peak (c).

at $X = 1.40C$ (right column). At the very-near wake ($X = 1.05C$) and directly after the trough two distinct peaks can be observed: one located at $f_{se,1} = 3.8$ and one located at $f_{se,2} = 4.4$. As we move towards the mid-point between the trough and the peak, the energy of both peaks reduces but they can still be identified. At the serration, the peaks still appear to exist, albeit significantly attenuated. The reduction in the peak energy as we move from the trough to the peak indicates a strong shedding inhomogeneity along the span of the airfoil.



(a) Trough - $X = 1.05C$ (b) Trough - $X = 1.40C$

(c) Mid - $X = 1.05C$ (d) Mid - $X = 1.40C$

(e) Peak - $X = 1.05C$ (f) Peak - $X = 1.40C$

Figure 3.18: Power spectra of V velocity component for different cross-stream locations, extending from $Y = -0.3C$ to $Y = 0.1C$. Left column data are probed very close to the trailing edge peak ($X = 1.05C$), while right column data are probed at $X = 1.40C$. From top to bottom, the probing lines are aligned with the trough, the mid-point and the peak of the serrations.

The two frequencies $f_{se,1}$ and $f_{se,2}$ are in almost perfect agreement with the dominant frequencies identified in the two previous airfoil cases. The dominant wake mode for the straight trailing edge was found to oscillate at $f_1 \approx f_{se,1}$, which was found to be the subharmonic of the natural frequency of the separating shear layer. The $f_{bl,1} \approx f_{se,2}$ frequency was found to be the shedding frequency of the flatback

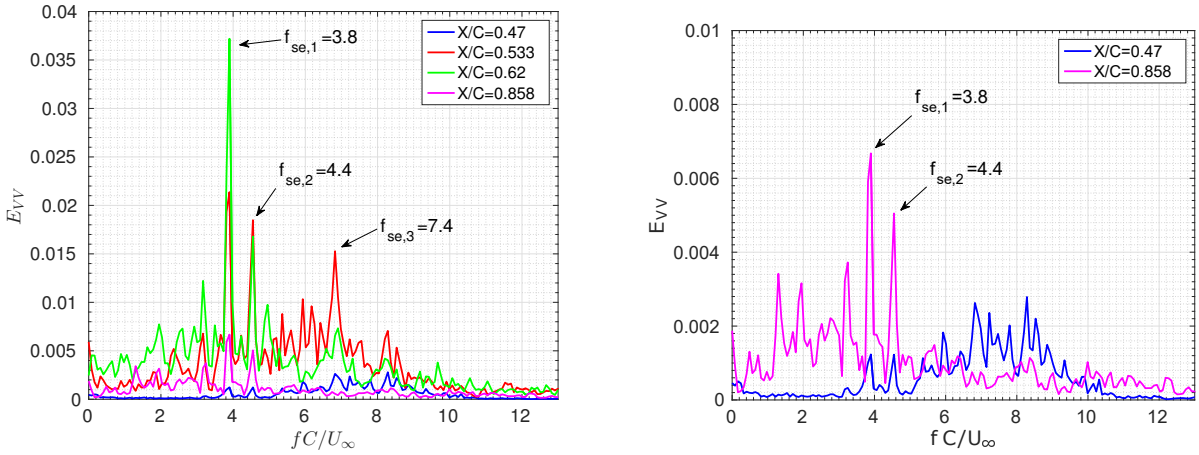


Figure 3.19: PSD of the cross velocity component at four streamwise locations at the suction side of the airfoil at $Z/C = 0.266$ (plane through the peak). Figure 3.19b has zoomed in the region $E_{vv} \leq 0.01$ for better illustration of the signals at $X/C = 0.47$ and $X/C = 0.858$.

airfoil, which forced a lock-in between the shear layer and the wake shedding, as analysed in section (3.2.2). In the straight trailing edge airfoil only the subharmonic was present in the wake, while for the flatback only the shedding frequency was present. For the serrated case, both can be detected.

In Figure 3.19 the spectra for 4 different points in the suction side of the airfoil are plotted. All of the points are located at $Z/C = 0.266$, which corresponds to a plane through the peak. Figure 3.19b on the right has zoomed-in at the small values of E_{vv} for better visualisation of the spectra at two points. The first point at $X/C = 0.47$ shows a similar behavior to that in Figure 3.2a, namely a broad spectrum at relatively high frequencies. As the shear layer transitions, three peaks appear at the points located at $X/C = 0.533$ and $X/C = 0.62$. The peak at $f_{se,3} = 7.4$ is very close to the shear layer natural frequency observed at the straight trailing edge case, while the peaks at $f_{se,1}$ and $f_{se,2}$ are at the same frequencies already identified in Figure 3.18. At the fourth measurement point, at $X/C = 0.858$ i.e. directly before the trailing edge, the peak at $f_{se,3}$ has completely attenuated and only $f_{se,1}$ and $f_{se,2}$ are still dominant, an observation in agreement with the wake

spectra of Figure 3.18.

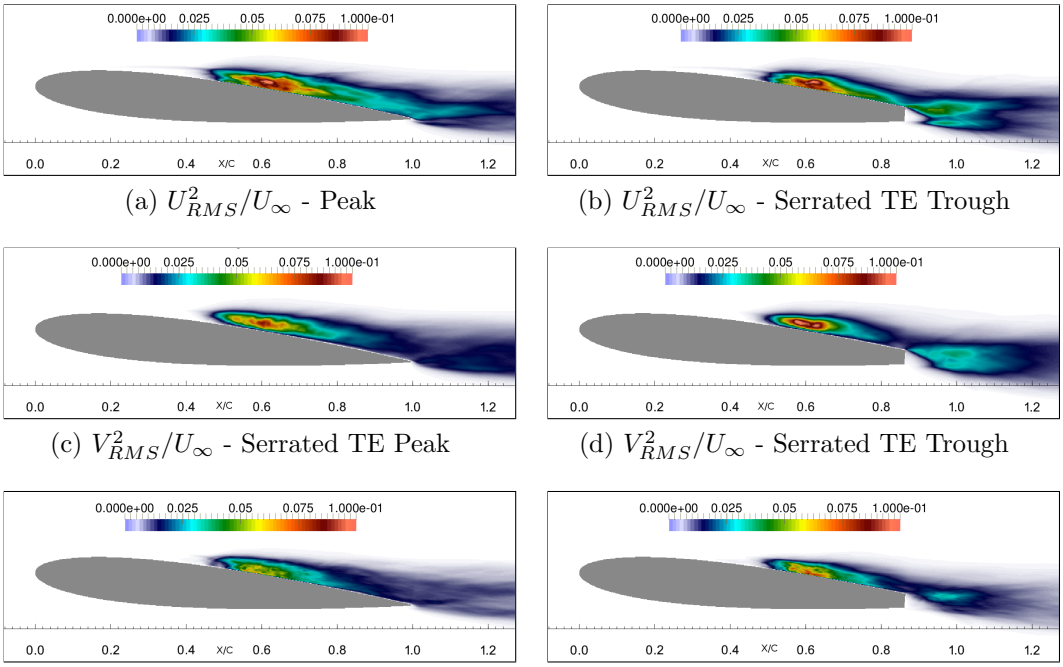
If the trough bluntness, ϵ, is used as a length scale, the Strouhal number corresponding to the frequency $f_{se,2}$ is $St = 0.1628$. Nedić and Vassilicos (2015) studied a similar configuration and measured a Strouhal number equal to 0.203. However, the Reynolds number was three times larger and the boundary layers were tripped on both sides of the airfoil, as already mentioned. Due to tripping the boundary layers were attached, so Nedić and Vassilicos (2015) detected only the trailing edge shedding frequency, $f_{se,2}$, and not $f_{se,1}$ which is due to the separating shear layer. This is fully consistent with the present findings.

Unlike the blunt trailing edge, where the shedding frequency was the only one present, in the serrated edge case we detect two distinct frequencies, the subharmonic of the natural frequency and the trailing edge shedding frequency. Why is the subharmonic frequency observed for the serrated case and not for the blunt case? The reason is that the shedding for the serrated case is weaker due to the linear tapering of the thickness, from a maximum at the trough to almost zero at the peak. For the blunt trailing edge, the energy contained in the shedding frequency (Figure 3.8) is 5 times larger than that for the serrated trailing edge (Figure 3.18). This indicates that the forcing is much stronger for the blunt case, leading to a suppression of the subharmonic.

There are few other papers that have dealt with the flow around an airfoil with serrated trailing edges. Jones and Sandberg (2012) have studied similar flows, but there is an important difference, as already mentioned in the introduction: the serrations are attached to a straight trailing edge airfoil, and are not cut into the body of the airfoil. The thickness is therefore minimal and secondary patterns, as the one observed in this paper, were not reported.

In Figure 3.20 the normal Reynolds stresses are plotted for the serrated trailing edge airfoil. The left column shows the distributions at a spanwise plane through the serration peak, and the right column through the trough. The spanwise variation of

the Reynolds stress distributions in the wake is clear. The wakes in the peak resemble those of the straight trailing edge airfoil shown in Figure 3.4 (left column), while in the trough plane the distributions are similar to those of the flatback airfoil (Figure 3.4, right column). There is however a significant difference in the V_{RMS} component in the wake. Comparison between Figures 3.4d and 3.20d reveals that the intense shedding from the blunt trailing edge, which gives rise to an elongated region of cross-stream fluctuations extending up to almost half a chord length downstream, is significantly attenuated in the serrated airfoil both in terms of magnitude as well as size. This indicates that the intensity of the wake shedding is reduced due to the presence of the serrations, and agrees with the previous discussion of the spectra. Experimental measurements (Nedić and Vassilicos, 2015) also confirm this behaviour. Another difference worth mentioning is the peak which appears in the spanwise velocity fluctuations W_{RMS} directly after the trailing edge trough (Figure 3.20f). This peak indicates a strong spanwise fluctuation of the flow field on this location, originating from the 3D secondary flow pattern discussed earlier in this section.



(a) U^2_{RMS}/U_∞ - Peak

(b) U^2_{RMS}/U_∞ - Serrated TE Trough

(c) V^2_{RMS}/U_∞ - Serrated TE Peak

(d) V^2_{RMS}/U_∞ - Serrated TE Trough

(e) W^2_{RMS}/U_∞ - Serrated TE Peak

(f) W^2_{RMS}/U_∞ - Serrated TE Trough

Figure 3.20: Streamwise, cross-stream and spanwise Reynolds stress distributions for the serrated trailing edge airfoil at a spanwise plane through a peak (Figures 3.20a, 3.20c and 3.20e) and through a trough (Figures 3.20b, 3.20d and 3.20f).

3.3 Conclusions

This chapter considered the effect of trailing edge modifications on the time-average and dynamic characteristics of the separating shear layer and the near wake of a NACA 0012 airfoil. Two airfoils, one with blunt and the other with serrated trailing edge, were compared with a standard NACA 0012 airfoil with straight trailing edge. The DMD method was applied to extract the dominant modes in the wake and the corresponding frequencies. For the standard airfoil, two modes were detected: one with high frequency which corresponds to the Kelvin Helmholtz instability originating from the separating shear layer, and one with low frequency that emerges as a subharmonic, and is detectable in the suction side and the near wake.

In the blunt trailing edge airfoil, the two shear layer frequencies were strongly suppressed, and the frequency of the shear layer was locked to the shedding frequency due to the exposed bluntness. Examination of the spatial structure of the shedding mode revealed an upstream effect on the suction side of the airfoil. The shedding frequency was close to the subharmonic of the natural shear layer frequency and, under such conditions, lock-on is known to occur.

When the trailing edge consists of triangular serrations with tapering bluntness, the strength of the vortices shed from the exposed blunt part was strongly attenuated compared to the flatback airfoil. In this case, both the subharmonic and the shedding frequency were present in the velocity spectra, in the wake as well as in the suction side of the airfoil. In contrast with the flatback airfoil, in this case lock-in was not observed. This was attributed to the weaker forcing amplitude due to the decorrelation of the vortices shed along the span.

Chapter 4

Resolvent analysis of the flow around the airfoil

4.1 Introduction

In the previous chapter a direct link was established between the behaviour of the separated boundary layer and the shedding characteristics of the various trailing edges shapes. In this chapter, we employ a different point of view to shed more light into the flow. This approach, called resolvent analysis, treats differently the linear and non-linear part of the Navier-Stokes equations that govern the velocity perturbations around the time-averaged flow. The non-linear part is considered as an unknown input to a linear system whose behaviour is determined solely by the linear part. This method was introduced by McKeon and Sharma (2010) in a turbulent pipe flow and has since then been used in the studies of various flow configurations (see chapter 1).

Mathematical formulation.

We start by employing the Reynolds decomposition and express the instantaneous velocity field as the sum of the mean flow field and the fluctuating field $\boldsymbol{u} = \overline{\boldsymbol{u}} + \boldsymbol{u'}$.

Substituting this decomposition into the Navier-Stokes equations and time-averaging we get the Reynolds Averaged Navier-Stokes equations:

$$\overline{\boldsymbol{u}} \cdot \nabla \overline{\boldsymbol{u}} + \overline{\boldsymbol{u}' \cdot \nabla \boldsymbol{u}'} + \frac{1}{\rho} \nabla \overline{p} - \nu \nabla^2 \overline{\boldsymbol{u}} = 0, \tag{4.1}$$

$$\nabla \cdot \overline{\boldsymbol{u}} = 0. \tag{4.2}$$

Subtracting equations (4.1) and (4.2) from the Navier-Stokes equations, we get the following equations for the fluctuating quantities:

$$\frac{\partial \boldsymbol{u}'}{\partial t} + \overline{\boldsymbol{u}} \cdot \nabla \boldsymbol{u}' + \boldsymbol{u}' \cdot \nabla \overline{\boldsymbol{u}} = -\frac{1}{\rho} \nabla p' + \nu \nabla^2 \boldsymbol{u}' - \boldsymbol{u}' \cdot \nabla \boldsymbol{u}' + \overline{\boldsymbol{u}' \cdot \nabla \boldsymbol{u}'} \tag{4.3}$$

$$\nabla \cdot \boldsymbol{u}' = 0. \tag{4.4}$$

We can now consider the last two terms of the right hand side as an unknown turbulent forcing term $\boldsymbol{f}' = \overline{\boldsymbol{u}' \cdot \nabla \boldsymbol{u}'} - \boldsymbol{u}' \cdot \nabla \boldsymbol{u}'$. This approach has been used, among others, by Gómez et al. (2016b), Beneddine et al. (2016) and McKeon and Sharma (2010). It differs from the usual approach of considering an externally applied forcing, which has been used in the studies of Schmid and Brandt (2014), Sipp et al. (2010), Sipp and Marquet (2013) and Lu and Papadakis (2014), in that the input forcing $\boldsymbol{f}'$ has an implicit, non-linear, dependence on the output $\boldsymbol{u}'$. The forcing $\boldsymbol{f}'$ contains the Reynolds stresses terms, which are determined by the perturbations $\boldsymbol{u}'$ and which, in their turn, affect the time-averaged flow field. Thus there is also an indirect dependence, via the Reynolds stresses, of the input $\boldsymbol{f}'$ on the internal state of the system (since the latter is determined by the time-averaged flow field). Equation (4.3) is not linear, but if we assume that the flow has reached a statistically steady state making $\overline{\boldsymbol{u}}$ known and immutable, then equations (4.3) and (4.4) can indeed be treated as a linear system, where the linear part of equation (4.3) and equation (4.4) act as the transfer function linking the output $\boldsymbol{u}'$ to $\boldsymbol{f}'$. A schematic of this approach is shown in Figure 4.1, where the assumption amounts effectively to the removal of the feedback non-linear part inside the dashed box.

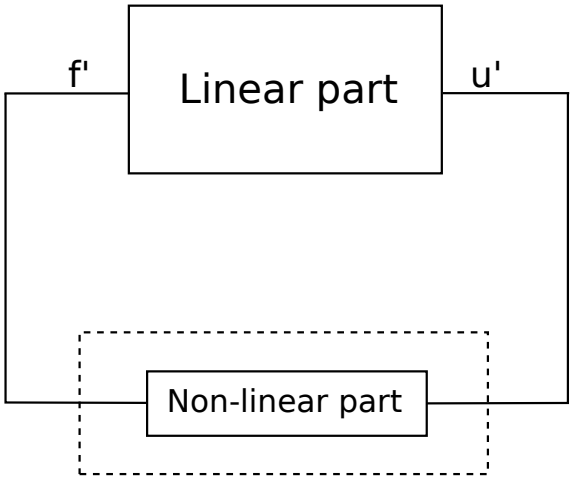


Figure 4.1: Schematic of the resolvent operator system.

Equations (4.3) and (4.4) can be written in matrix form as:

$$\boldsymbol{B}\frac{\partial}{\partial t}\begin{pmatrix}\boldsymbol{u}'\\ p'\end{pmatrix} = \boldsymbol{L}\begin{pmatrix}\boldsymbol{u}'\\ p'\end{pmatrix} + \boldsymbol{M}\boldsymbol{f}', \tag{4.5}$$

where the following operators and matrices have been defined:

$$\boldsymbol{L} = \begin{pmatrix}-\overline{\boldsymbol{u}}\cdot\nabla() - ()\cdot\nabla\overline{\boldsymbol{u}} + \nu\nabla^2() & -\frac{1}{\rho}\nabla()\\ \nabla\cdot() & 0\end{pmatrix} \tag{4.6}$$

$$\boldsymbol{M} = \begin{pmatrix}1\\ 0\end{pmatrix} \tag{4.7}$$

$$\boldsymbol{B} = \begin{pmatrix}1 & 0\\ 0 & 0\end{pmatrix}. \tag{4.8}$$

The discrete form of the operators and matrices will generally depend on the discretisation method used. For example if the finite element method is used, as in the current work, the discrete form of $\boldsymbol{B}$ will be the mass matrix, with elements $(B_{ij}) = \int_\Omega \phi_i\phi_j d\Omega$, where ϕ denotes the basis functions used. If the finite volume method is used then $\boldsymbol{B}$ is a diagonal matrix with the volumes of the cells in its

main diagonal. If the finite differences method is used then $\boldsymbol{B}$ becomes the identity matrix. The matrix $\boldsymbol{L}$ will be the discretised Navier-Stokes operator and finally the matrix $\boldsymbol{M} = \boldsymbol{BP}$ will be the mass matrix pre-multiplied by the prolongation matrix $\boldsymbol{P}$ which will add zeros to the terms of the forcing vector that correspond to the continuity equation (since this equation is already linear does not contain a forcing term).

Taking the temporal Fourier transform of equation (4.5) we get:

$$i\omega \boldsymbol{B} \begin{pmatrix} \hat{\boldsymbol{u}} \\ \hat{p} \end{pmatrix} = \boldsymbol{L} \begin{pmatrix} \hat{\boldsymbol{u}} \\ \hat{p} \end{pmatrix} + \boldsymbol{BP}\hat{\boldsymbol{f}}, \tag{4.9}$$

where the variables $\hat{\boldsymbol{u}}$, $\hat{p}$ and $\hat{\boldsymbol{f}}$ indicate the complex amplitudes of the Fourier transforms of the velocity, pressure and turbulent forcing fields respectively. If the forcing amplitude $\hat{\boldsymbol{f}}$ is assumed to be zero, we recover the generalized eigenvalue problem which is used to determine the stability characteristics of the time-averaged flow field (the eigenvalue would be $i\omega$). For non-zero forcing term, equation (4.9) can be written as:

$$\begin{pmatrix} \hat{\boldsymbol{u}} \\ \hat{p} \end{pmatrix} = \left(i\omega \boldsymbol{B} - \boldsymbol{L}\right)^{-1} \boldsymbol{BP}\hat{\boldsymbol{f}}. \tag{4.10}$$

Pre-multiplying the left and right hand sides by $\boldsymbol{P}^{\dagger}$ we can extract only the velocity fluctuations $\hat{\boldsymbol{u}}$:

$$\hat{\boldsymbol{u}} = \boldsymbol{P}^{\dagger} \left(i\omega \boldsymbol{B} - \boldsymbol{L}\right)^{-1} \boldsymbol{BP}\hat{\boldsymbol{f}}, \tag{4.11}$$

where the dagger ($\dagger$) indicates the conjugate transpose. The matrix $\boldsymbol{R}(\omega) = \boldsymbol{P}^{\dagger} \left(i\omega \boldsymbol{B} - \boldsymbol{L}\right)^{-1} \boldsymbol{BP}$ is discretised resolvent operator of the mean-flow and it is the focus of the analysis presented in this chapter.

Calculation of the optimal forcings and responses

In the aforementioned context, the inputs are the components of the vector $\hat{\boldsymbol{f}}$, i.e. the turbulent fluctuations (in Fourier space) of the flow field, which are unknown.

The resolvent is the transfer function between the response of the flow field to a forcing and it can be used to study the types of forcing and frequencies that will maximise the gain G of the system, defined using an appropriate $\|\cdot\|$ norm as: :

$$G = \frac{\|\hat{\boldsymbol{u}}\|_{Q_u}^2}{\|\hat{\boldsymbol{f}}\|_{Q_f}^2}, \tag{4.12}$$

where the subscripts Q_u and Q_f indicate that different weighting matrices can be used to define the forcing and response measures. In the current work, the norm defines the energy of the corresponding variable in the whole domain. For any vector variable $\boldsymbol{y}$ in the domain Ω, the norm is defined as $\|\boldsymbol{y}\|^2 = \int_\Omega \boldsymbol{y}^\dagger \boldsymbol{y} d\Omega$. The discrete form is $\|\boldsymbol{y}\|^2 = \boldsymbol{y}^\dagger \boldsymbol{Q} \boldsymbol{y}$, where $\boldsymbol{Q}$ is a symmetric positive definite[1] matrix arising from the discretisation of the integral operator in the domain, and $\boldsymbol{y}$ is now the vector of discrete values of the variable $\boldsymbol{y}$ (here we abuse the notation and use the same symbol for the continuous variable and the vector of discrete values, but we hope that the distinction becomes clear from the context).

The discrete form of equation (4.12) can be written as:

$$G = \frac{\hat{\boldsymbol{u}}^\dagger \boldsymbol{Q}_f \hat{\boldsymbol{u}}}{\hat{\boldsymbol{f}}^\dagger \boldsymbol{Q}_u \hat{\boldsymbol{f}}}. \tag{4.13}$$

As mentioned earlier, the norms define the energy in the whole domain, so $\boldsymbol{Q}_f = \boldsymbol{Q}_u = \boldsymbol{Q}$. This is not necessary, since the response norm can be selected to maximise the energy only on a specific part of the domain, in which case $\boldsymbol{Q}_f \neq \boldsymbol{Q}_u$. Such an experiment, with different Q_f and Q_u matrices, was performed in this work and its results will be shown in the next chapter.

Replacing $\boldsymbol{Q}_f$ and $\boldsymbol{Q}_u$ with $\boldsymbol{Q}$ and using the resolvent relation in (4.11), equation

[1]The finite element approximation of $\boldsymbol{y}$ is $\boldsymbol{y}(\boldsymbol{x}) = \sum_i \boldsymbol{y}_i \phi_i(\boldsymbol{x})$, where $\phi_i(\boldsymbol{x})$ are the basis functions used and $\boldsymbol{y}_i$ are the nodal values of the variable $\boldsymbol{y}$. The discretised norm will then be $\|\boldsymbol{y}\|^2 = \sum_{i,j} \boldsymbol{y}_i \boldsymbol{y}_j \int_\Omega \phi_i(\boldsymbol{x}) \phi_j(\boldsymbol{x}) d\Omega$ or using matrix notation $\|\boldsymbol{y}\|^2 = \boldsymbol{y}^\dagger \boldsymbol{Q} \boldsymbol{y}$ with $\boldsymbol{Q} = (Q_{ij})$ and $Q_{ij} = \int_\Omega \phi_i(\boldsymbol{x}) \phi_j(\boldsymbol{x}) d\Omega$. Thus, by definition $Q_{ij} = Q_{ji}$ making $\boldsymbol{Q}$ symmetric and since $\|\boldsymbol{y}\|^2 = \boldsymbol{y}^\dagger \boldsymbol{Q} \boldsymbol{y} > 0$, $\boldsymbol{Q}$ is also positive definite.

(4.13) becomes:

$$G = \frac{\hat{\boldsymbol{f}}^\dagger \boldsymbol{R}^\dagger \boldsymbol{Q} \boldsymbol{R} \hat{\boldsymbol{f}}}{\hat{\boldsymbol{f}}^\dagger \boldsymbol{Q} \hat{\boldsymbol{f}}}. \tag{4.14}$$

The maximum of G can be directly found by a straightforward differentiation of equation (4.14):

$$\begin{aligned} \frac{\partial G}{\partial \hat{\boldsymbol{f}}} &= \frac{2\boldsymbol{R}^\dagger \boldsymbol{Q} \boldsymbol{R} \hat{\boldsymbol{f}} \hat{\boldsymbol{f}}^\dagger \boldsymbol{Q} \hat{\boldsymbol{f}} - 2\hat{\boldsymbol{f}}^\dagger \boldsymbol{R}^\dagger \boldsymbol{Q} \boldsymbol{R} \hat{\boldsymbol{f}} \boldsymbol{Q} \hat{\boldsymbol{f}}}{(\hat{\boldsymbol{f}}^\dagger \boldsymbol{Q} \hat{\boldsymbol{f}})^2} = \\ &= \frac{2}{\hat{\boldsymbol{f}}^\dagger \boldsymbol{Q} \hat{\boldsymbol{f}}} \left(\boldsymbol{R}^\dagger \boldsymbol{Q} \boldsymbol{R} \hat{\boldsymbol{f}} - G \boldsymbol{Q} \hat{\boldsymbol{f}} \right) = 0. \end{aligned} \tag{4.15}$$

Thus the forcing $\hat{\boldsymbol{f}}$ which maximises the gain G is the solution of the following generalized eigenvalue problem:

$$\boldsymbol{R}^\dagger \boldsymbol{Q} \boldsymbol{R} \hat{\boldsymbol{f}} = G \boldsymbol{Q} \hat{\boldsymbol{f}}, \tag{4.16}$$

which is solved with the methods described in chapter 2 (due to the positive definiteness of matrix $\mathbf{Q}$ the calculations are greatly simplified - see Lehoucq et al. (1998)). The eigenproblem of equation (4.16) gives the weighted[2] right singular vectors and their corresponding squared singular values of the resolvent matrix $\boldsymbol{R}$. The left singular vectors are then given by:

$$\hat{\boldsymbol{u}}_i = \sigma_i^{-1} \boldsymbol{R}(\omega) \hat{\boldsymbol{f}}_i, \tag{4.17}$$

where $\sigma_i = \sqrt{G}$ are the singular values of $\boldsymbol{R}(\omega)$.

The previous analysis illustrates the physical significance of the right and left singular vectors, which are, respectively, the forcing (at a given frequency) which will maximise the output of the system under the defined measure, and the response respectively. The gain of the system (i.e. the ratio of the kinetic energies) will then be G. The right and left singular vectors which correspond to the highest singular

[2]In the classical SVD, the left and right singular vectors satisfy $u_i^\dagger u_j = \delta_{ij}$ and $v_i^\dagger v_j = \delta_{ij}$, whereas in the weighted SVD they satisfy $u_i^\dagger Q_u u_j = \delta_{ij}$ and $v_i^\dagger Q_v v_j = \delta_{ij}$, where Q_u and Q_v are positive definite matrices (Jolliffe, 2002).

value -i.e. those which produce the largest response - will also be referred from now on as the optimal forcing and optimal response respectively.

It is straightforward to show that the forcings and responses form bases of their corresponding spaces and thus any arbitrary forcing and response can be written as a linear combination of the base members $\hat{\boldsymbol{f}}_i$ and $\hat{\boldsymbol{u}}_i$ respectively. This allows us to express any forcing $\boldsymbol{f}$ as a weighted sum of the base forcings $\hat{\boldsymbol{f}}_i$:

$$\hat{\boldsymbol{f}} = \sum_{i=1}^{N} \langle \hat{\boldsymbol{f}}, \hat{\boldsymbol{f}}_i \rangle \hat{\boldsymbol{f}}_i, \tag{4.18}$$

where N is the number of singular modes and $\langle \cdot, \cdot \rangle$ denotes the projection of the arbitrary forcing $\boldsymbol{f}$ to the i^{th} forcing mode. Then, using equations (4.11) and (4.17), the corresponding response $\hat{\boldsymbol{u}}$ to the arbitrary forcing $\hat{\boldsymbol{f}}$ can be expressed as:

$$\hat{\boldsymbol{u}} = \sum_{i=1}^{N} \sigma_i \langle \hat{\boldsymbol{f}}, \hat{\boldsymbol{f}}_i \rangle \hat{\boldsymbol{u}}_i. \tag{4.19}$$

Another implication of the orthogonality of the optimal modes is that their energy is simply the sum of their corresponding weights:

$$\|\hat{\boldsymbol{f}}\|_f^2 = \sum_{i=1}^{N} \langle \hat{\boldsymbol{f}}, \hat{\boldsymbol{f}}_i \rangle^2, \tag{4.20}$$

and

$$\|\hat{\boldsymbol{u}}\|_u^2 = \sum_{i=1}^{N} \sigma_i^2 \langle \hat{\boldsymbol{f}}, \hat{\boldsymbol{f}}_i \rangle^2. \tag{4.21}$$

In many shear flows the first singular value is orders of magnitude larger than the rest (McKeon and Sharma (2010); Beneddine et al. (2016)). This means that with just the first optimal response we can capture most of the kinetic energy of the perturbations in the flow field, since for an arbitrary forcing, its projection onto the optimal forcing $\hat{\boldsymbol{f}}_1$, when multiplied with the corresponding singular value σ_1, will dominate. Furthermore, as we will see in Section 4.4, we can use this result to calculate approximations to the velocity spectra based on the estimation of the

coefficient $\langle \boldsymbol{f}, \hat{\boldsymbol{f}}_1 \rangle$ for each frequency.

In the following we apply the resolvent analysis to the time-averaged field obtained for the straight and blunt trailing edge airfoils. The time-averaged flow is the one obtained from the DNS results presented in the previous chapter.

4.2 Straight trailing edge airfoil results

4.2.1 Spectrum of the resolvent operator

The results for the straight trailing edge airfoil are presented first. In Figure 4.2 the spectrum of the resolvent operator is shown for the 5 most dominant singular values. It can be observed that the most dominant singular value, (i.e. the one with

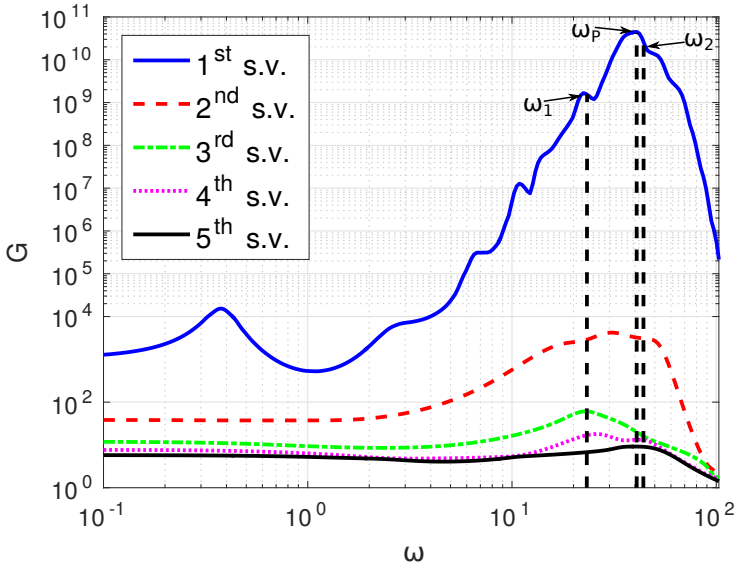


Figure 4.2: Singular values plot of the resolvent operator. The first 5 singular values ($s.v.$) of the operator are plotted against the angular frequency ω.

the largest growth ratio in equation (4.12)) is several orders of magnitude larger than all the others for a wide range of frequencies. This strong amplification is a characteristic feature of the convectively unstable nature of the separated shear layer which forms on the suction side of the airfoil. Indeed, in several other studies

(see Beneddine et al. (2016), Sipp et al. (2010), Garnaud et al. (2013), Alizard et al. (2009)), a similar behaviour has been observed in flows which exhibit a strong convective instability. It is clear from the analysis presented earlier, that as the frequency ω approaches an eigenvalue of the disretised Navier-Stokes operator $\boldsymbol{L}$, the resolvent norm attains very large values (this is the classical definition of resonance - i.e forcing a system close to one of its eigenfrequencies). Moreover, when this happens, the optimal response and the optimal forcing approach the direct and adjoint optimal modes respectively (Schmid and Brandt (2014), Sartor et al. (2014)).

Despite the physical explanation of the large values of the resolvent norm given in the previous paragraph, another reason that also plays an important part, is the non-normality of the Navier-Stokes operator $\boldsymbol{L}$ which can arise from regions of high-shear and lead to badly conditioned matrices and large responses. An understanding of non-normality of the discretised operator can be obtained if we consider the spectral decomposition of a system matrix $\boldsymbol{A}$. If the system matrix $\boldsymbol{A}$ is normal (i.e. it satisfies $\boldsymbol{A}^\dagger\boldsymbol{A} = \boldsymbol{A}\boldsymbol{A}^\dagger$), its eigenvectors will be orthogonal and the matrix can be decomposed as $\boldsymbol{A} = \boldsymbol{V}\boldsymbol{\Lambda}\boldsymbol{V}^{-1} = \boldsymbol{V}\boldsymbol{\Lambda}\boldsymbol{V}^\dagger$, where the columns of $\boldsymbol{V}$ contain the eigenvectors of $\boldsymbol{A}$ and $\boldsymbol{\Lambda}$ is a diagonal matrix with the eigenvalues of $\boldsymbol{A}$ in its main diagonal. Thus, the response of the system to an initial condition $\boldsymbol{u}(0)$ will be:

$$\begin{aligned}
&\frac{d\boldsymbol{u}}{dt} = \boldsymbol{L}\boldsymbol{u} \Leftrightarrow \\
&\boldsymbol{u}(t) = e^{t\boldsymbol{A}}\boldsymbol{u}\,(0) \Leftrightarrow \\
&\boldsymbol{u}(t) = e^{t\boldsymbol{V}\boldsymbol{\Lambda}\boldsymbol{V}^{-1}}\boldsymbol{u}\,(0) \Leftrightarrow \\
&\boldsymbol{u}(t) = \boldsymbol{V}e^{t\boldsymbol{\Lambda}}\boldsymbol{V}^{-1}\boldsymbol{u}\,(0)\,.
\end{aligned} \tag{4.22}$$

The asymptotic time behaviour of this system will then be solely dependent on the matrix exponential $e^{t\boldsymbol{\Lambda}}$ or, consequently, the eigenvalues of $\boldsymbol{A}$, since the consecutive applications of the unitary[3] matrix $\boldsymbol{V}$ and its inverse will have no net effect on the gain of the system.

[3]The matrix $\boldsymbol{V}$ is unitary because the eigenvectors of $\boldsymbol{A}$, which form the columns of $\boldsymbol{V}$, are orthogonal.

If, however, matrix $\boldsymbol{A}$ is non-normal, while its eigendecomposition can still be calculated, the eigenvectors will not be orthogonal, and consequently matrix $\boldsymbol{V}$ will not be unitary, and it will have a net contribution to the response of the system under consideration. In that case, for a stable matrix, it is possible to have a large transient response, followed by the eventual decay. Another approach is to use the singular value decomposition, $\boldsymbol{A} = \boldsymbol{U}\boldsymbol{\Sigma}\boldsymbol{W}^{\dagger}$, where the columns of $\boldsymbol{U}$ contain the left singular vectors of $\boldsymbol{A}$, $\boldsymbol{\Sigma}$ is diagonal and it contains the singular values of $\boldsymbol{A}$, and the columns of $\boldsymbol{W}$ contain the right singular vectors of $\boldsymbol{A}$. In this case, the matrices $\boldsymbol{U}$ and $\boldsymbol{W}$ are unitary, but they represent different spaces. Furthermore, the identity that was used in the last step of equation (4.22), and allowed us to have an asymptotic dependence only on $\boldsymbol{\Lambda}$, cannot be applied now. The response of the system in this case is given by:

$$\boldsymbol{u}(t) = e^{t\boldsymbol{U}\boldsymbol{\Sigma}\boldsymbol{W}^{\dagger}}\boldsymbol{u}\left(0\right). \tag{4.23}$$

It is clear thus from equation (4.23) that the response of the system to the initial perturbation will not be dependent only on the singular values of the matrix $\boldsymbol{A}$, but also on matrices $\boldsymbol{U}$ and $\boldsymbol{W}$. If $\boldsymbol{A}$ is close to being normal the singular value decomposition will be close to the spectral decomposition (they are equal for a normal positive semi-definite matrix), and the aforementioned effect will be minimal. If, on the other hand, the matrix is highly non-normal the effects can be important, leading to very high values of the response even when the forcing frequency is not close to an eigenvalue of the matrix. Indeed such *pseudoresonance* phenomena have been observed in similar studies (Sartor et al. (2014),Garnaud et al. (2013)). For a thorough explanation on how the non-normality can lead to high response gains see Trefethen (1991).

We now turn our focus to the gain observed in the various frequencies of interest. As can be seen in Figure 4.2, the optimal growth reaches its highest value at a frequency which is very close to the natural frequency of the separated shear

layer obtained in chapter 3 (annotated frequency ω_2 in Figure 4.2). Linear stability analysis performed in the flow field of the straight trailing edge airfoil revealed an unstable eigenvalue again at a frequency very close ω_2. In Figure 4.3 the spectrum of the linearised Navier-Stokes operator is plotted and the unstable mode can be seen at the angular frequency $\omega = 48.46$ (a 3.7% difference from ω_2). This indicates a resonance at this frequency which can partially explain the very high amplification rates around ω_2, along with the aforementioned effect of non-normality. It must be pointed out that unstable modes such as the one seen in Figure 4.3 are not uncommon when the time-averaged flow is used (see for example Mittal (2008), Barkley (2006), Rodriguez and Theofilis (2010) and Zhang and Samtaney (2016b)). A last observation is related to the overall shape of the resolvent norm, which resembles that of a band-pass filter centred approximately at the shear layer frequency ω_2. Indeed past studies, such as those by Jones et al. (2010), Desquesnes et al. (2007) and Rodriguez and Theofilis (2010), identified a frequency selection mechanism in laminar separation bubbles, according to which the separation bubble will selectively amplify frequencies around the dominant frequency of the shear layer, thus acting as a band-pass filter.

The present analysis also appears to be highly capable of capturing the fundamental frequency of the flow field. The frequency ω_2 in Figure 4.2 is approximately 7.8% larger than the frequency ω_P at which the graph peaks. This is a very good estimation of the shear layer natural frequency, bearing in mind that only the time-averaged flow has been used in these calculations. The time-averaged flow field has been found in past studies (see Barkley (2006) and Sipp and Lebedev (2007)) to provide an accurate estimate of the dominant flow frequency, in the context of the linear stability analysis.

4.2.2 Optimal modes

The real part of the streamwise and cross-stream components of the optimal forcing and response at the peak frequency ω_P in Figure 4.2 are shown in Figures 4.4 and

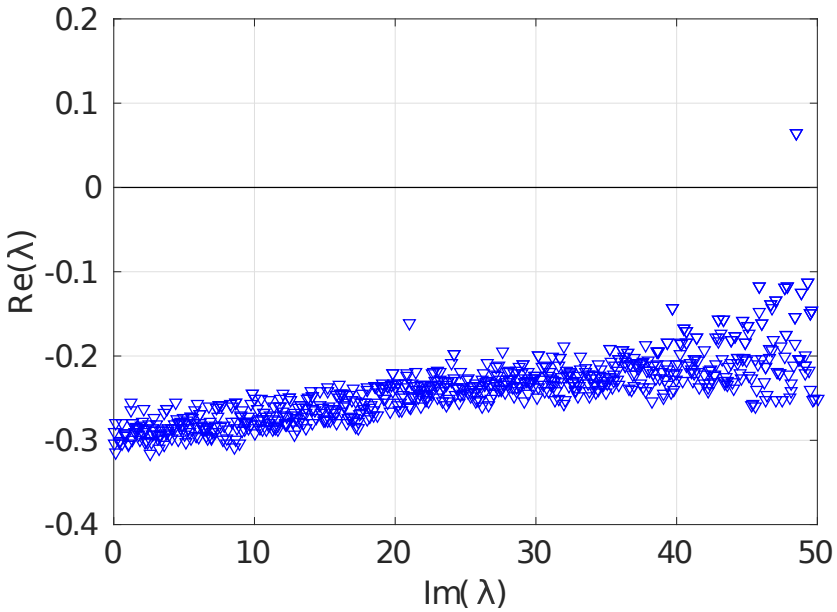
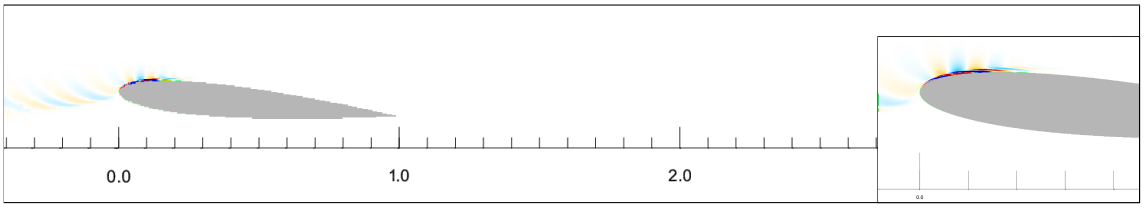


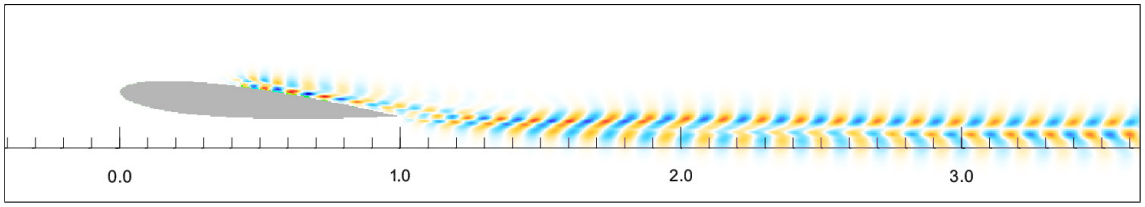
Figure 4.3: Spectrum of the linearized Navier-Stokes operator for the straight trailing edge case.

4.5 respectively. The imaginary part (not shown here) is very similar, but displaced in the streamwise direction (the time variation of the displaced real and imaginary parts results in the perturbation propagating in the streamwise direction). Both components of the forcing, shown in Figures 4.4a and 4.5a, are found to be highly localized in the leading edge of the airfoil with their magnitude decaying rapidly further downstream. The area in which the forcing is dominant coincides with the area of maximum acceleration of the boundary layer. It was found in chapter 3 that the separation point is located at $X/C = 0.145$ and, as can be observed in Figure 4.4a, the forcing attains its maximum value slightly upstream of this location. This observation has also been made in past studies, where the stability characteristics of similar flow configurations were studied (Dovgal et al. (1994),Desquesnes et al. (2007)).

The insets shown in Figures 4.4a and 4.5a, provide a more detailed view of the forcing close to the leading edge of the airfoil. The structure of the forcing and, more specifically, the opposing inclination to the mean flow suggests that the Orr



(a) Optimal forcing $\hat{f}_x$ corresponding to the frequency with the largest gain in Figure 4.2.

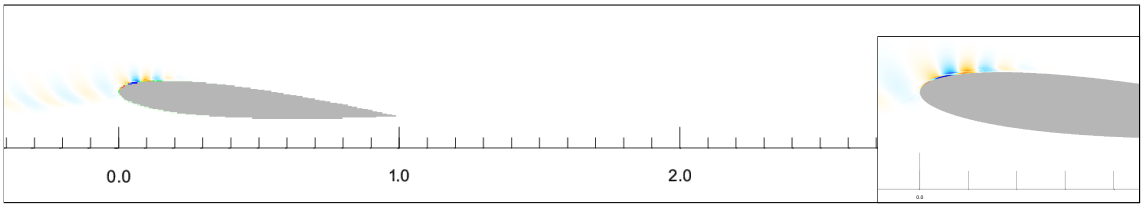


(b) Optimal response $\hat{u}_x$ corresponding to the frequency with the largest gain in Figure 4.2.

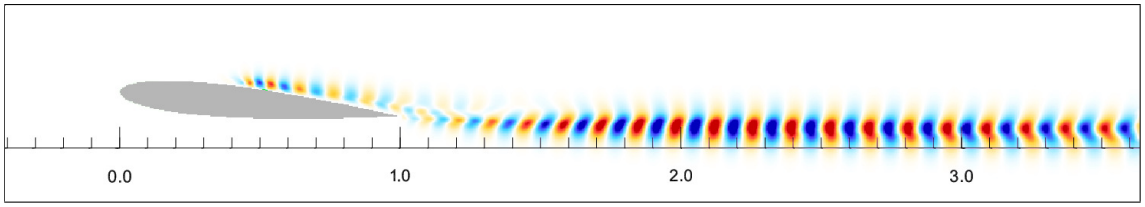
Figure 4.4: Streamwise component of the optimal forcing $\hat{f}_x$ and response $\hat{u}_x$ at the frequency ω_P with the highest amplification rate. The inset in Figure 4.4a shows in detail the structure of the mode close to the leading edge of the airfoil.

mechanism is at play as the dominant mechanism amplifying the disturbances upstream of separation. Butler and Farrell (1992) studied the optimal perturbations (i.e. the perturbations which give the maximum energy growth) in three model flows (Couette flow, Poiseuille flow and a Blasius boundary layer), and found a very similar structure in the initial condition which would give the maximum amplification. It was suggested that the initial perturbations are amplified by the action of the Reynolds stresses, as the latter transfer energy from the mean shear to the perturbations, which consequently re-align with the mean flow taking the usual form of the TS-waves (see also Åkervik et al. (2008) and references therein). In Figure 4.6 the streamwise forcing is plotted along with the displacement thickness of the boundary layer, and as can observed the forcing is entirely located inside the area between the airfoil and the displacement thickness, that is the area where the mean shear is maximised.

The streamwise and cross-stream components of the optimal response, shown in Figures 4.4b and 4.5b are again indicative of the convectively unstable nature of the flow field. There is a clear cause-and-effect relation between the forcing, localised upstream, and the corresponding response further downstream. The applied forcing



(a) Optimal forcing $\hat{f}_y$ corresponding to the frequency with the largest gain in Figure 4.2.



(b) Optimal response $\hat{u}_y$ corresponding to the frequency with the largest gain in Figure 4.2.

Figure 4.5: Cross-stream component of the optimal forcing $\hat{f}_y$ and response $\hat{u}_y$ at the frequency ω_P with the highest amplification rate. The inset in Figure 4.5a shows in detail the structure of the mode close to the leading edge of the airfoil.

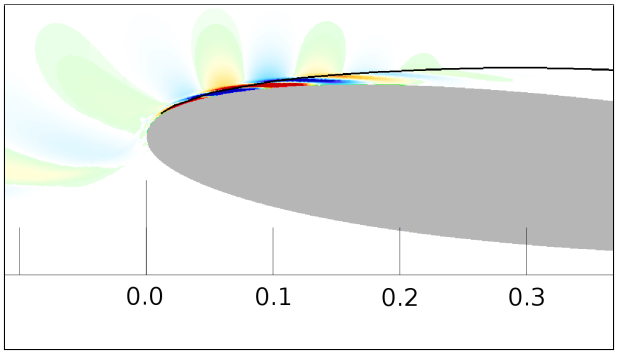
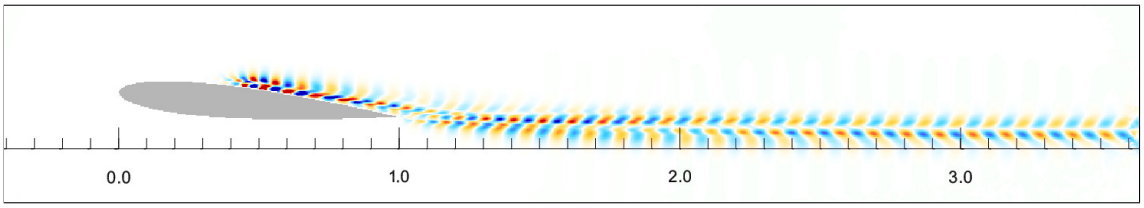


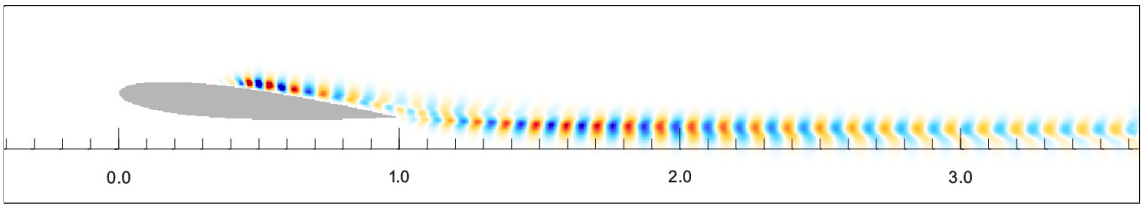
Figure 4.6: Streamwise component of the optimal forcing $\hat{f}_x$ at the leading edge with the displacement thickness of the boundary layer overlapped.

leads to a response which is gradually amplified in the separated shear layer and reaches a local maximum value at reattachment. The attached boundary layer causes a significant attenuation of the response, which is again amplified further downstream in the wake where it reaches its global maximum value at approximately one chord length downstream of the trailing edge. We recall that, since the peak frequency is very close to the most unstable eigenvalue of the linearised problem, the optimal forcing and response should be very close to the adjoint and direct modes respectively. Indeed as Figure 4.7 suggests, where the streamwise and cross-

stream components of the most unstable direct mode are shown, there is a striking resemblance between the optimal response calculated from the resolvent analysis and the global mode, calculated from the global linear stability analysis.



(a) Streamwise component.



(b) Cross-stream component.

Figure 4.7: Spatial structure of the eigenmode corresponding to the most unstable eigenvalue in Figure 4.3 at $\omega = 48.46$.

It was mentioned earlier in this section that due to the dominance of the first singular value, the dominant mode of the flow field, found in the previous chapter, should be very close to the optimal response shown in Figures 4.4b and 4.5b. Indeed a comparison between Figures 3.3b and 4.5b appears to corroborate this statement, since in both cases a very similar spatial structure can be observed. It must be pointed out that DMD results of Figure 3.3b are computed directly from the simulation results, thus differences are expected due to the fact that the DMD method is an approximation to the dominant modes while the resolvent analysis presented here provides an exact analysis (see Sharma et al. (2016) for a study on the similarities and differences between the two approaches).

In Figure 4.8 the displacement thickness of the suction side boundary layer (solid black line) and the zero streamwise mean velocity contour (solid brown line) are superimposed on the cross-stream component of the optimal response. It can be seen that the response grows rapidly at the downstream end of the recirculation zone.

The growth of the disturbance is also very closely correlated with the maximum reverse flow observed in the separation bubble. In Figure 4.9 the maximum reverse flow and the velocity ratio R[4] at the separated part are plotted at the airfoil's suction side. It can indeed be observed that the rapid growth of the response in Figure 4.8, which takes place at approximately $X/C = 0.4$, closely matches the location of the rapid increase of the reverse flow seen in Figure 4.9. Indeed, a strong effect of the strength of the reverse flow on the amplification rate of the disturbances has been found in the past. Strykowski and Niccum (1992) found a significant increase in the amplitude of velocity oscillations, in a mixing layer where the velocity ratio R is larger than 1 (counter-current mixing layer) compared to the case where $R < 1$ (co-flowing mixing layer), with an even larger increase as this ratio exceeds the critical value of approximately $R = 1.3$. In Figure 4.9 the velocities ratio appears to be close to this critical value and even exceed it at a small area. Despite the fact that the flow studied by Strykowski and Niccum (1992) (a parallel mixing layer) is different from the one examined in the present thesis, the results appear to agree and to justify, at least in a qualitatively sense, the location where the disturbances are rapidly amplified. More pertinent to the present case, Hammond and Redekopp (1998) and Rist and Maucher (2002) identified a relation between the onset of global absolute instability and the magnitude of the reverse flow, which would need to be at least 30% of the free stream velocity for a global absolute instability to be observed. In an almost identical flow configuration as the present one, Jones (2008) found a maximum reverse flow of approximately 15%, which is in a very good agreement with the peak of the reversed flow in Figure 4.9.

We now turn our focus to the optimal modes at the wake shedding frequency, which was found in chapter 3 to be the sub-harmonic of the shear layer frequency (annotated frequency ω_1 in Figure 4.2). The streamwise component of the forcing is shown in Figure 4.10a and its corresponding response in Figure 4.10b. The optimal

[4]The velocity ratio of a shear layer is defined as $R = \frac{U_1 - U_2}{U_1 + U_2}$, where U_1 and U_2 are the velocities of the two streams. In the current case they are the free stream velocity and the maximum reverse velocity at each point respectively.

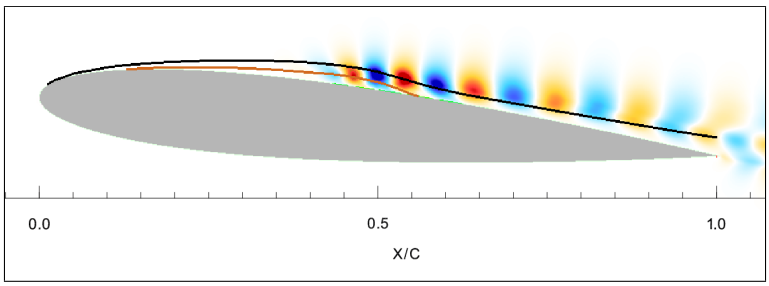


Figure 4.8: Cross-stream component of the optimal response at the suction side of the airfoil. The solid black lines shows the displacement thickness of the boundary layer while the solid brown line is the zero-streamwise mean velocity contour.

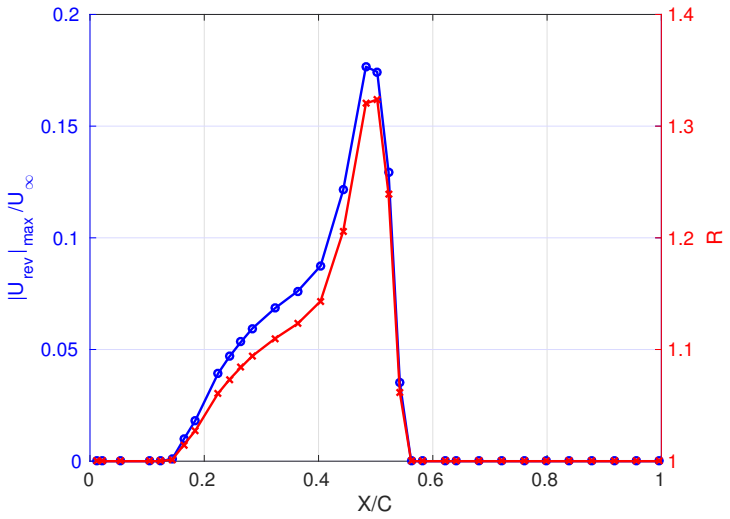
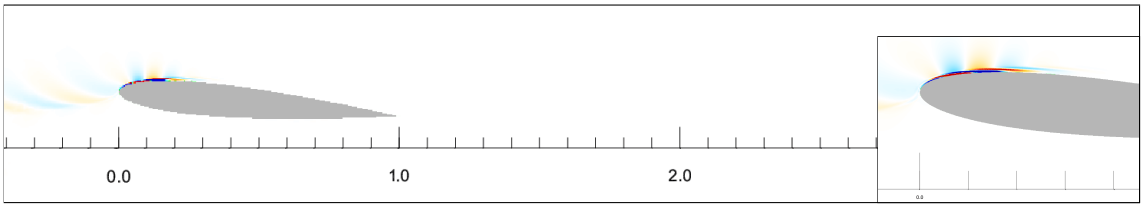
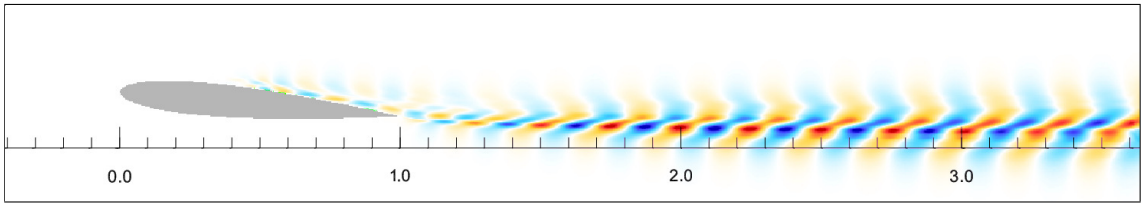


Figure 4.9: Absolute value of the maximum reverse flow (blue line-left axis) and velocities ratio R (red line-right axis), over the airfoil's suction side.



(a) Optimal forcing (X-component).

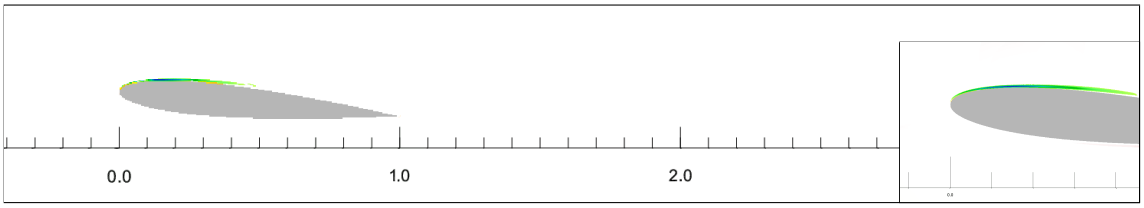


(b) Optimal response (X-component).

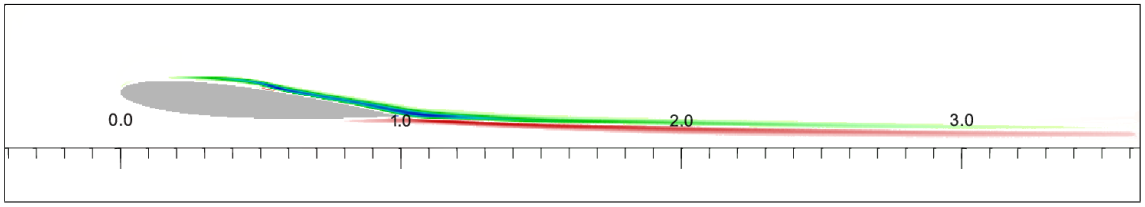
Figure 4.10: Streamwise component of the optimal forcing $\hat{f}_x$ and response $\hat{u}_x$ at the wake shedding frequency that was calculated in chapter 3.3b. The inset in Figure 4.10a shows in detail the structure of the mode close to the leading edge of the airfoil.

forcing in this case shows a very similar spatial structure with the forcing in Figure 4.4a. The only observable difference is the smaller wavenumber of the perturbations shown in the inset of Figure 4.10a, a result which is expected due to the lower temporal frequency of this mode. The response to this forcing is shown in Figure 4.10b. The spatial support of the response suggests a much higher receptivity of the wake to this lower frequency excitation compared to the shear layer, where any response is barely visible. This is anticipated since, as was shown in Figure 3.2b in chaper 3, the fundamental frequency in the wake is the sub-harmonic which originates from the shear layer.

It is interesting to see that a low frequency peak can be detected in Figure 4.2 around $\omega = 0.4$. The streamwise component of the corresponding forcing and response modes are shown in Figures 4.11a and 4.11b respectively, with the inset in Figure 4.11a showing in detail the forcing at the leading edge. The spatial structure of the response appears to originate at the separation point and it appears to follow the separated shear layer, the reattached boundary layer and the mixing layer after the trailing edge. Furthermore, the frequency of the mode is very low compared to



(a) Optimal forcing.



(b) Optimal response.

Figure 4.11: Streamwise component of the optimal forcing $\hat{f}_x$ and response $\hat{u}_x$ at the low frequency peak shown in Figure 4.2.

the range of frequencies where the dynamic content of this flow lies. Similar low frequency bumps have been observed in past similar studies of separation bubbles (see Dovgal et al. (1994) and references therein) and they were attributed to the long-waved vertical motions of the shear-layer (the flapping of the shear layer). This frequency could therefore be the low frequency response of the aforementioned flapping motion of the shear layer.

4.3 Blunt trailing edge airfoil results

4.3.1 Spectrum of the resolvent operator

In this section the results of the resolvent analysis will be presented for the blunt trailing edge airfoil. In Figure 4.12 the resolvent spectrum is plotted against the same range of frequencies. A very similar result to that shown in Figure 4.2 can be observed overall, albeit with two noticeable differences. The first one is a much higher irregularity of the most dominant singular value at its peak area. Indeed, one can observe in Figure 4.12 that, at the same range of frequencies which in the previous case was characterized by a smooth rise in the amplification gain, reaching

a peak close to the shear layer natural frequency and then sharply dropping, we now have, after again an initial increase, a very coarse behaviour followed by the expected drop. At the range of this irregular behaviour we have a pronounced peak at $\omega_{SH} = 29.3$ which almost perfectly matches the shedding frequency identified in chapter 3. After this peak a series of smaller local ones are observed until the gain decays rapidly after approximately $\omega = 60$. The second difference is related to the second highest singular value (red dashed line in Figure 4.12) which shows a much narrower amplification band compared to the same plot in Figure 4.2, and a maximum value of approximately an order of magnitude larger.

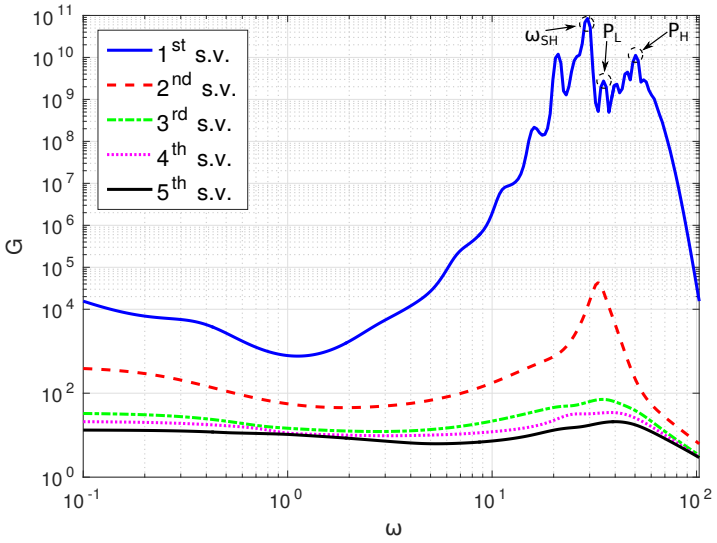


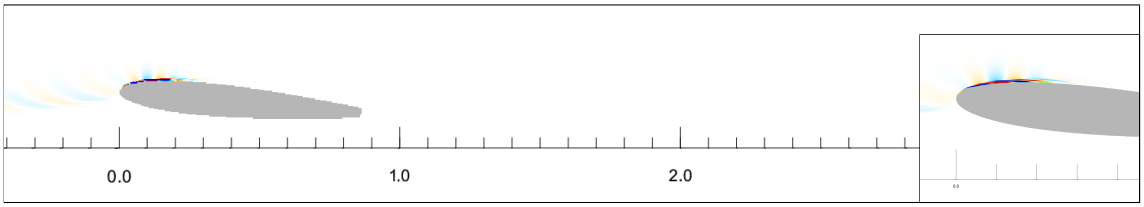
Figure 4.12: Singular values plot of the resolvent operator for the blunt trailing edge airfoil. The first 5 singular values ($s.v.$) of the operator are shown.

4.3.2 Optimal modes

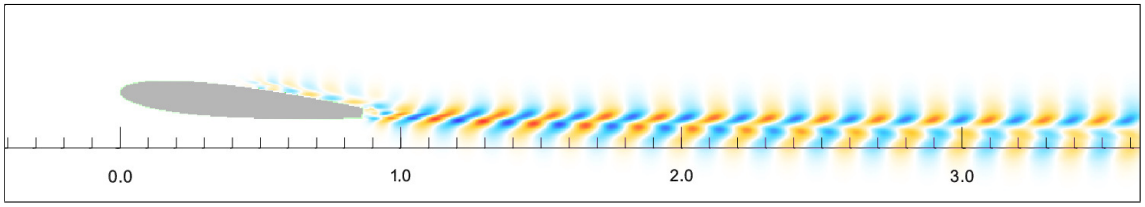
We now turn our attention to the spatial structures of the modes corresponding to some of the frequencies of interest identified above. In Figure 4.13 the optimal forcing and response which correspond to the highest peak at the shedding frequency ω_{SH} of Figure 4.12 can be seen. The streamwise and cross-stream components of the forcing (Figures 4.13a and 4.14a respectively) show a very similar structure with

the straight trailing edge case. The area of maximum receptivity is again found to be at the leading edge, before separation and with slender structures aligned against the mean flow.

The streamwise and cross-stream components of the corresponding optimal response (shown in Figures 4.13b and 4.14b respectively) are found to be concentrated in the wake of the airfoil, a direct result of the Kárman shedding originating from the truncated trailing edge. There is a presence of the mode at the suction side of the airfoil, albeit very attenuated. The shape of this mode is again, and as expected from the analysis until now, very similar to the dominant DMD mode found for the same airfoil in chapter 3, with highly energetic structures originating from the truncated part of the trailing edge and propagating downstream. For the sake of completeness we are also plotting for this case the cross-stream component of the response along with the boundary layer's displacement thickness and the zero velocity contour in Figure 4.15 and the maximum reverse flow with the velocities ratio in Figure 4.16. Not many differences are observed in Figure 4.15 when compared with the previous case. The reverse flow, seen in Figure 4.16 shows a similar shape but with smaller values of the reverse flow and of the velocity ratio. The maximum value of the reverse flow in this case is 15% of U_∞ as opposed to approximately 17.6% for the straight trailing edge.

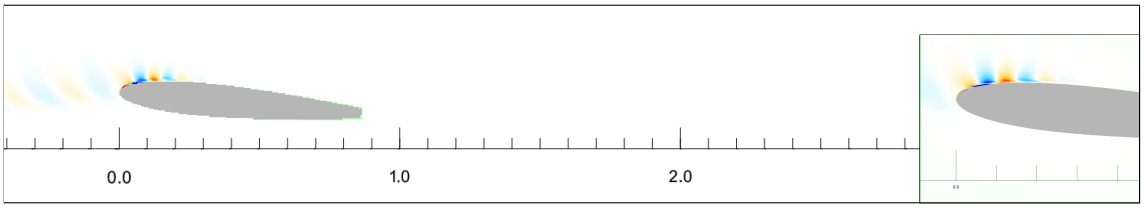


(a) Optimal forcing $\hat{f}_x$.

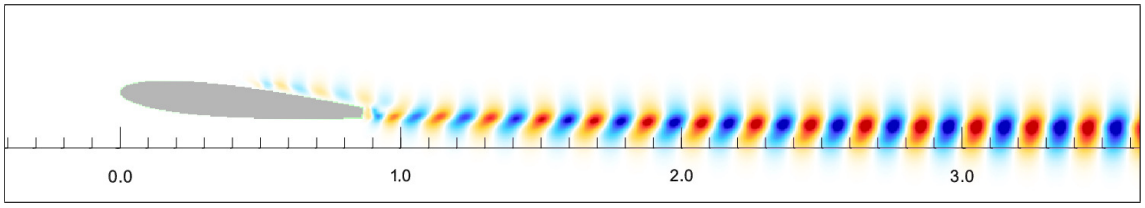


(b) Optimal response $\hat{u}_x$.

Figure 4.13: Streamwise component of the optimal forcing $\hat{f}_x$ and response $\hat{u}_x$ at the frequency showing the vortex shedding frequency.



(a) Optimal forcing $\hat{f}_y$.



(b) Optimal response $\hat{u}_y$.

Figure 4.14: Cross-stream component of the optimal forcing $\hat{f}_y$ and response $\hat{u}_y$ at the frequency showing the vortex shedding frequency.

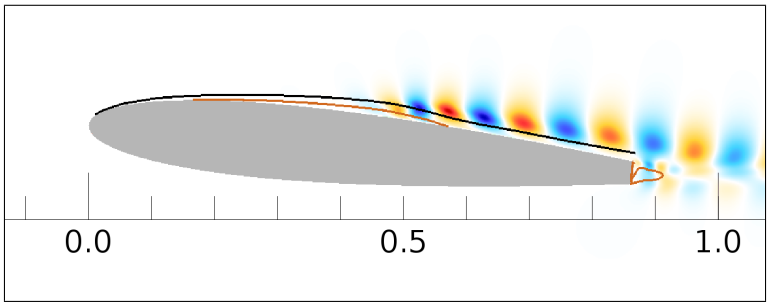


Figure 4.15: Cross-stream component of the optimal response at the suction side of the airfoil. The solid black lines shows the displacement thickness of the boundary layer while the solid brown line shows the zero streamwise velocity contour.

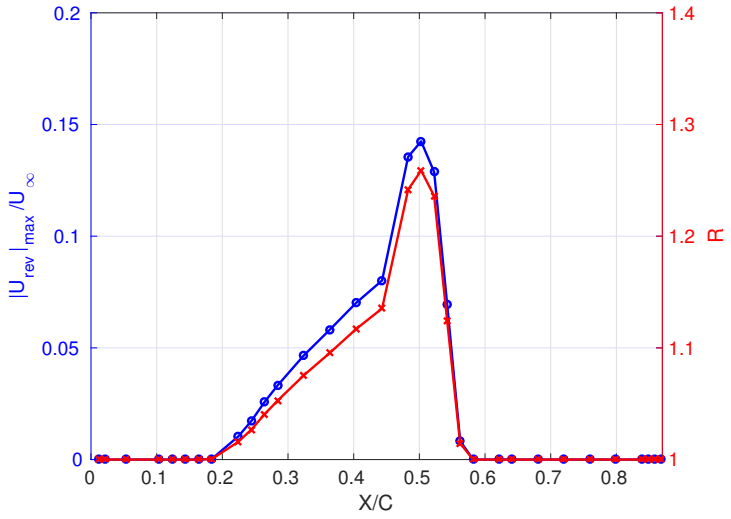
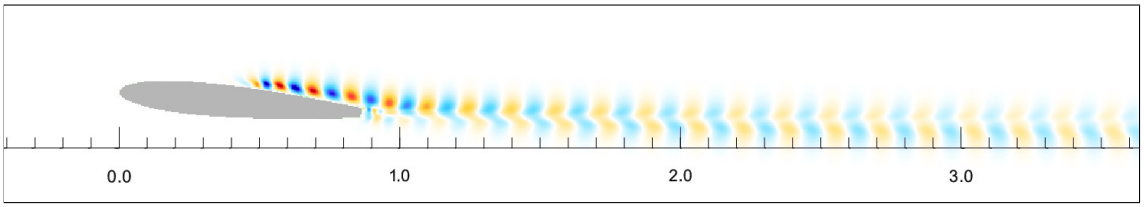


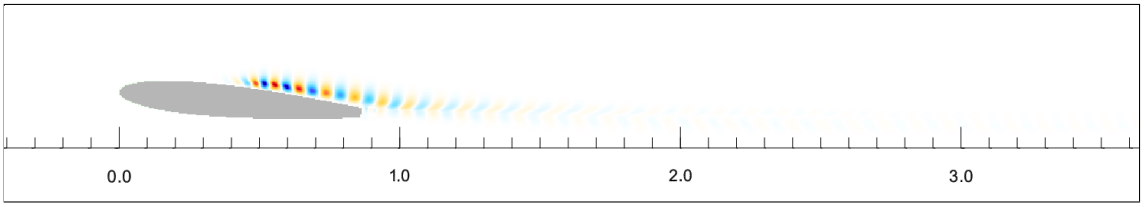
Figure 4.16: Absolute value of the maximum reverse flow and the velocities ratio over the airfoil's suction side.

As mentioned before, the singular value plot of the resolvent for this case shows some irregularities compared to the smooth spectrum of the straight trailing edge case. In order to identify the spatial behaviour of the modes in the range where these irregularities are observed, we identify two peaks (marked as P_L and P_H in Figure 4.12) which fall within this range and plotted the responses at the corresponding frequencies. In Figures 4.17 the cross-stream component of each response is shown. An important difference between Figures 4.17a, 4.17b and Figure 4.14b is that the responses at the two smaller peaks P_L and P_H have minimal presence in the wake, with most of their energy being concentrated at the suction side of the airfoil, as opposed to the response at the global maximum which had shown the opposite behaviour. Their corresponding forcings (not shown here) had a very similar structure with every forcing corresponding to the 1^{st} singular value seen until now, i.e. localized at the leading edge and inclined against the mean flow.

The spatial behaviour of the optimal responses at the two peaks, suggests a difference on the receptivity characteristics of the flow, and more specifically on which region of the flow field is more receptive to a specific frequency. In Figure 4.18 we plot together the resolvent spectra of both the blunt and the straight trailing edge airfoils. It can be observed that the range of frequencies where the two graphs are mostly different, is in the range of maximum receptivity of the straight trailing edge case, roughly between $\omega = 30$ and $\omega = 60$, with the amplification rate for the blunt trailing edge airfoil being almost an order of magnitude smaller in the region of interest. These differences suggest an interplay between the different stability characteristics of the two phenomena present at the blunt airfoil, namely the Kárman shedding from the truncated trailing edge and the separated shear layer. Indeed these two different flows have been found to exhibit distinctively different behaviours (Schmid and Sipp (2016), Huerre and Monkewitz (1990)), with the former being characterized by the presence of an absolute instability (known also as an *oscillator*) whereas the latter being characterised by a convective instability (known as a *noise amplifier*). It can thus be inferred that the presence of the absolute instability



(a) Response at peak P_L.



(b) Response at peak P_H.

Figure 4.17: Cross-stream component of the optimal response at the two annotated peaks P_L 4.17a and P_H 4.17b.

renders the separated shear layer much less receptive when compared to the straight trailing edge case. The observations in this chapter suggest a significant disparity between the response of the two flow fields to perturbations. It appears that the lock-in mechanism, identified in chapter 3, has reduced the receptivity of the shear layer to perturbations.

4.4 Estimation of velocity spectra based on point measurements.

As shown earlier in this chapter, the response $\hat{\boldsymbol{u}}$ of the flow field to any forcing $\hat{\boldsymbol{f}}$, can be written as (equation (4.19) repeated below):

$$\hat{\boldsymbol{u}} = \sum_{i=1}^{N} \sigma_i \langle \hat{\boldsymbol{f}}, \hat{\boldsymbol{f}}_i \rangle \hat{\boldsymbol{u}}_i. \tag{4.24}$$

It is clear from equation (4.24) that if the first singular value is several orders of magnitude larger than all the others, the first term in the sum of equation (4.24) will dominate all the other terms (provided of course that the forcing has appreciable

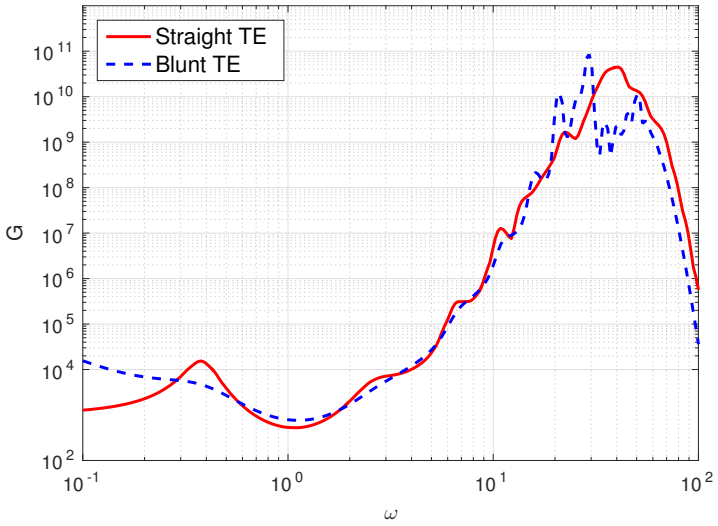


Figure 4.18: Resolvent spectra of the straight and blunt trailing edge cases.

projection to the optimal forcing $\hat{\boldsymbol{f}}_1$). In this case, the arbitrary response can be approximated by:

$$\hat{\boldsymbol{u}} = \sigma_1 \langle \hat{\boldsymbol{f}}, \hat{\boldsymbol{f}}_1 \rangle \hat{\boldsymbol{u}}_1. \tag{4.25}$$

The only unknown in equation (4.25) is the term $\langle \hat{\boldsymbol{f}}, \hat{\boldsymbol{f}}_1 \rangle$ which is the projection of the turbulent forcing $\hat{\boldsymbol{f}}$ onto the optimal forcing vector $\hat{\boldsymbol{f}}_1$. The forcing $\hat{\boldsymbol{f}}$ contains the non linear part of equation (4.3), which is unknown, thus the projection $\langle \hat{\boldsymbol{f}}, \hat{\boldsymbol{f}}_1 \rangle$ cannot be calculated. If we define the scalar $\Psi = \sigma_1 \langle \hat{\boldsymbol{f}}, \hat{\boldsymbol{f}}_1 \rangle$ then it is clear, that Ψ is only a function of the frequency ω, $\Psi = \Psi(\omega)$. Making the dependence of each variable in equation (4.25) explicit, we get:

$$\hat{\boldsymbol{u}}(\boldsymbol{x}, \omega) = \Psi(\omega) \hat{\boldsymbol{u}}_1(\boldsymbol{x}, \omega). \tag{4.26}$$

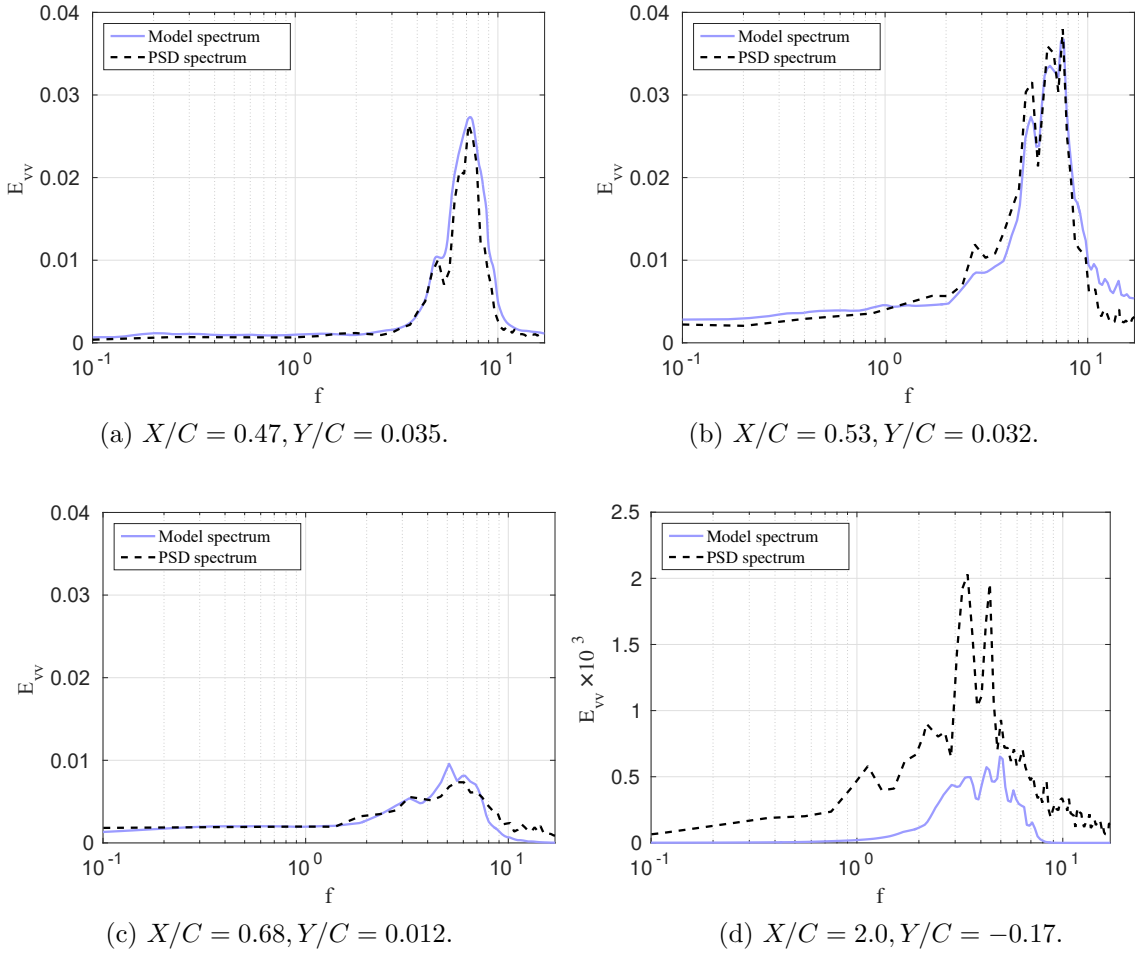
The only unknown variable is $\Psi(\omega)$. The spatial distribution of $\hat{\boldsymbol{u}}_1$ is known for every frequency, thus if we probe a point $\boldsymbol{x}_0$ in the flow field and take the Fourier transform of the velocity signal, we can then calculate $\Psi(\omega)$ by solving (4.26) to get:

$$\Psi(\omega) = \frac{\hat{\boldsymbol{u}}(\boldsymbol{x}_0, \omega)}{\hat{\boldsymbol{u}}_1(\boldsymbol{x}_0, \omega)} \tag{4.27}$$

Having estimated $\Psi(\omega)$ for each ω we can get from equation (4.26) an estimation of the spectrum of the velocity at an arbitrary point $\boldsymbol{x}$. This approach has been used recently with very promising results. Beneddine et al. (2016) used this method to estimate the velocity spectra at several points on a backward facing step flow, while Gómez et al. (2016b) used a variation of this method to estimate the forces acting on an inclined square cylinder (the coefficients in the latter case were calculated in the time domain rather than in the frequency domain as was done by Beneddine et al. (2016) and in the present work). In the latest of a series of publications on this topic Beneddine et al. (2017) applied the method to reconstruct the velocity and pressure fluctuation fields on a round jet at $Re = 3300$.

In the present study we applied this method to estimate the spectra in the two regions of interest of the flow field, namely the suction side of the airfoil and the wake. In Figure 4.19 the spectra of the cross-stream velocity are plotted along with the spectra estimated using equation (4.26), for the straight trailing edge airfoil. The function $\Psi(\omega)$ has been estimated from equation (4.27), using the spectrum of the cross-stream velocity signal at the calibration point $X/C = 0.62, Y/C = 0.022$, a location which is slightly downstream of the reattachment point of the boundary layer. A very good agreement can be observed in Figures 4.19a, 4.19b and 4.19c which show the spectra at 3 locations at the suction side of the airfoil at $X/C = 0.47, 0.53$ and 0.68 respectively. On the other hand a large discrepancy can be observed at the estimation of the spectrum in the wake, at $X/C = 2.0$, shown in Figure 4.19d.

This discrepancy reveals a pitfall of this model, which is related to the location of the calibration point used to estimate $\Psi(\omega)$. If the point is located at a position in which the energy content of a specific frequency or range of frequencies is low, it is expected that the values of $\Psi(\omega)$ will not be calculated correctly at these frequencies. In a flow which is characterized by a single frequency (for example a bluff body wake as in the case studied by Gómez et al. (2016b)) this problem does not manifest itself, since the flow is dominated by a single frequency and the



(a) $X/C = 0.47, Y/C = 0.035$.

(b) $X/C = 0.53, Y/C = 0.032$.

(c) $X/C = 0.68, Y/C = 0.012$.

(d) $X/C = 2.0, Y/C = -0.17$.

Figure 4.19: PSD spectrum as calculated from the model (calibration at $X/C = 0.62, Y/C = 0.022$).

calibration point can be selected in an energetic area of the flow field, such as the wake. As has been shown both in the present chapter and in chapter 3, the flow field created by the straight trailing edge airfoil shows two dominant frequencies: the shear layer frequency, present on the suction side of the airfoil, and its sub-harmonic which develops further downstream in the wake. It is thus clear that if the calibration point used for calculating the weights $\Psi(\omega)$ is located on the suction side of the airfoil, where the sub-harmonic frequency hasn't still fully developed, the values of $\Psi(\omega)$ at the corresponding omegas will not be accurate. This is exactly the case in the estimates shown in Figure 4.19, where the calibration point is located at

$X/C = 0.62$ where the dominant frequency is that of the shear layer. Consequently the values of $\Psi(\omega)$ at the nearby points $X/C = 0.47, 0.53$ and 0.68 are calculated correctly leading to the very good agreement seen in Figures 4.19a, 4.19b and 4.19c. The values, however, of $\Psi(\omega)$ at the smaller frequencies (that are present in the wake) were erroneous, since the energy content of the spectrum at $X/C = 0.62$ at these frequencies is very small, leading to the very small values of the estimation shown in Figure 4.19d.

A solution to this problem, proposed by Beneddine et al. (2016), is to use, instead of a single point, several points in the flow field and solve the, now over-determined, system of equations (4.27) (one equation for each point) in a least squares sense. If we select M points the minimization problem is:

$$\underset{\Psi(\omega)}{\text{minimize}} \quad \sum_{i=1}^{M} \|\hat{\boldsymbol{u}}(\boldsymbol{x}_i, \omega) - \Psi(\omega)\hat{\boldsymbol{u}}_1(\boldsymbol{x}_i, \omega)\|^2 \tag{4.28}$$

Using this approach the minimization algorithm will effectively select for each ω the most appropriate of the M points used, i.e. the point which, for the specific ω, will minimize the objective function shown above.

In Figure 4.20 the spectrum estimation is plotted again in the wake at the same streamwise location $X/C = 2.00$, the only difference being that the spectrum at an additional point located at $X/C = 1.40, Y/C = -0.12$ was also used to calculate the values of $\Psi(\omega)$ (the previous point at $X/C = 0.62$ was still used). As this figure suggests, application of this method using one extra point in the wake, has indeed corrected the discrepancy seen earlier in Figure 4.19d, since the velocity signal at $X/C = 1.40$ has now enough energy in the frequency range of the wake to properly scale the values of the optimal response. The spectra estimates at the three other points were virtually unchanged and they are not plotted here.

To illustrate the full capabilities of this method, a set of 10 points was used to calibrate the coefficients $\Psi(\omega)$. Eight of the points were located on the suction side of the airfoil and 2 in wake of the airfoil. Their locations are indicated by the

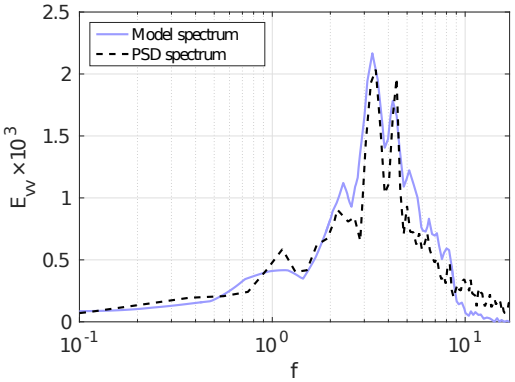
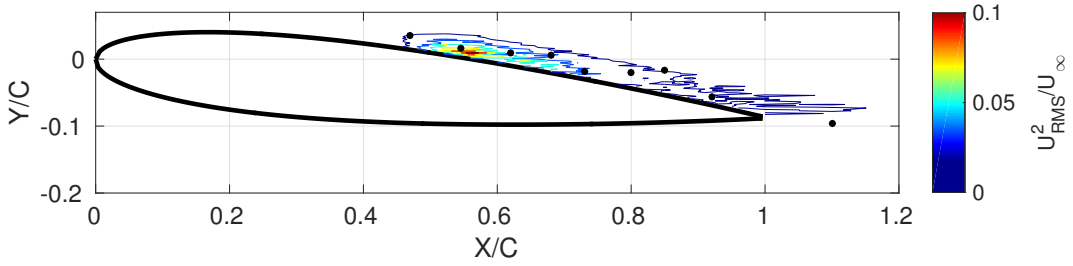


Figure 4.20: Spectrum estimate in the wake using two points for the estimation of the values of $\Psi(\omega)$.

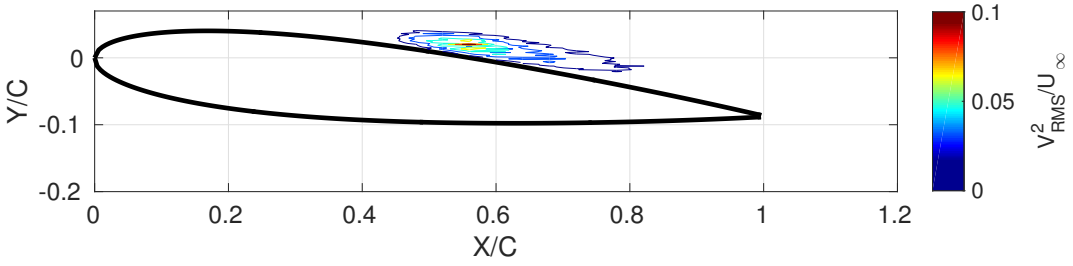
black dots in Figure 4.21a (with the exception of the last point which was located at $X/C = 1.40C$ and it is out of the field of view). Using the weight $\Psi(\omega)$ the spectra were calculated at several points of the flow field using equation (4.26), and by a direct integration of these spectra the mean square fluctuations of the streamwise and cross-stream velocities where estimated. The results are shown in Figure 4.21, where a very good agreement with Figure 3.4 can be observed.

The same method was applied for the blunt trailing edge airfoil, with the results shown in Figure 4.22 at the same locations as before. A very good agreement can be observed in all cases. For the blunt trailing edge airfoil a single calibration point, located again at $X/C = 0.62, Y/C = 0.022$, was used to calculate $\Psi(\omega)$. Nevertheless the estimations are very close to the actual spectrum, and the shedding frequency of $f_{bl,1} = 4.5$ is accurately predicted at all locations. The reason for the good agreement, is the dominance of the shedding mode throughout the flow field in this case. It was found in chapter 3 that the flow field around the blunt airfoil is dominated by the Kárman shedding from the truncated trailing edge. Apart from the wake, the shedding frequency was also identified in the shear layer (see Figure 3.10) whose frequency was now locked-in with the shedding frequency. Thus the probing point at $X/C = 0.62$ contains enough energy at this frequency to correctly predict $\Psi(\omega)$ and, consequently, give accurate estimations for the entire spectrum.

The estimation of the fluctuating values was calculated here using the points



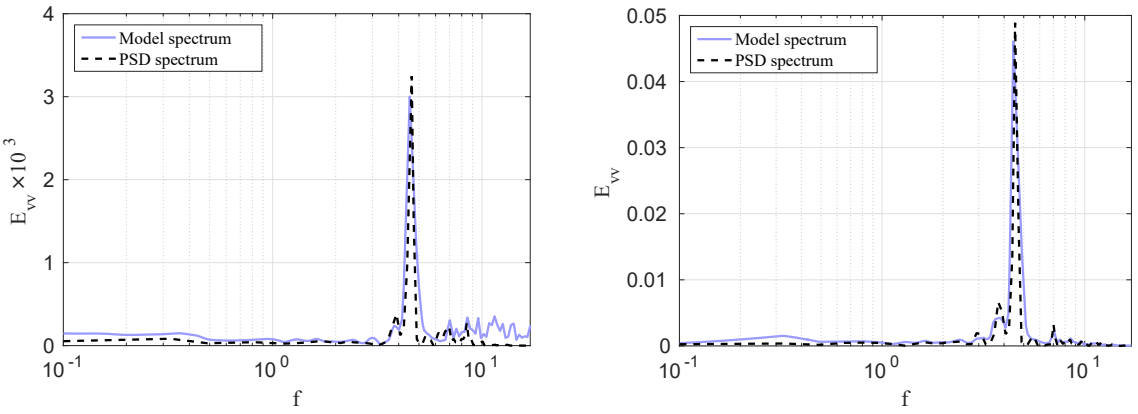
(a) RMS of streamwise velocity fluctuations.



(b) RMS of cross-stream velocity fluctuations.

Figure 4.21: Velocity fluctuations estimates for the straight trailing edge airfoil.

annotated in Figure 4.23a. Although as mentioned in the previous paragraph fewer points should be sufficient for this flow, due to the dominance of the Kárman shedding, 10 points were used again to improve the accuracy of the model. Indeed, comparing the results of Figures 4.23a and 4.23b with the equivalent plots in Figure 3.4, a very good agreement can be observed, and the accuracy of the model in estimating the spectra and, consequently the fluctuations, can be verified.



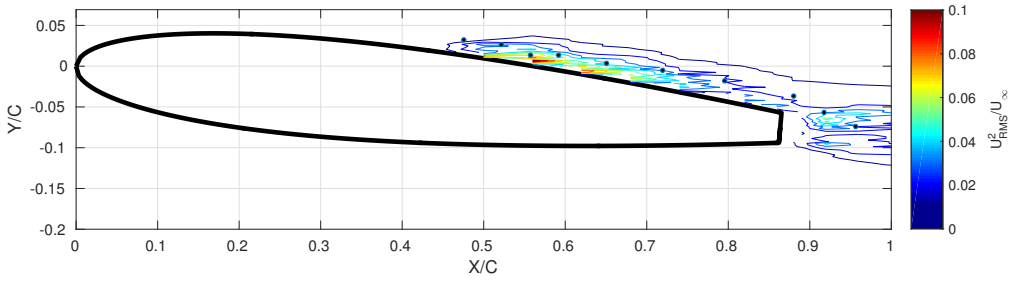
(a) $X/C = 0.47, Y/C = 0.035$.

(b) $X/C = 0.53, Y/C = 0.032$.

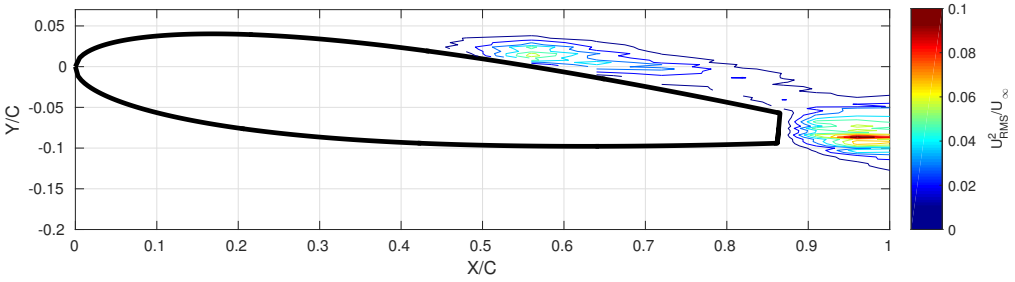
(c) $X/C = 0.68, Y/C = 0.012$.

(d) $X/C = 2.0, Y/C = -0.17$.

Figure 4.22: PSD spectrum as calculated from the model (calibration at $X/C = 0.62, Y/C = 0.022$).



(a) RMS of streamwise velocity fluctuations.



(b) RMS of cross-stream velocity fluctuations.

Figure 4.23: Velocity fluctuations estimates for the blunt trailing edge airfoil.

4.5 Conclusions

In this chapter we studied the frequency response of the separation bubble which forms around the straight and blunt trailing edge airfoils. The resolvent operator was used for this purpose, which allowed us to study the behaviour of the flow field from a system's point of view. The Reynolds stresses gradients which appear in the RANS equations, are treated as a turbulent forcing term, assuming that the time-averaged flow field is known. The resolvent operator provides then a linear map between this turbulent forcing and the perturbations, for a given angular frequency ω. The singular value decomposition of the resolvent allowed a detailed study of its behaviour for different frequencies. The singular values quantify the amplification while the left and right singular modes provide the optimal response and corresponding forcing which would give that amplification.

For the straight trailing edge airfoil, the spectrum of the dominant singular value of the resolvent operator suggests a very high amplification of the frequencies close to the natural frequency of the separated shear layer, a behaviour which is consistent with the frequency selection mechanism which characterizes the separation bubbles. The optimal forcing and response for certain frequencies of interest was also studied. It was revealed that the area most susceptible to forcing is the leading edge of the airfoil, up to approximately $X/C = 0.2$. The spatial structure of the forcing showed an inclination against the mean flow, a result which has been found also in other flow configurations such as jets Garnaud et al. (2013) and boundary layers Sipp and Marquet (2013) and can be attributed to the Orr mechanism, according to which the perturbations inclined against the mean flow extract energy from the strong shear. The spatial structure of the corresponding responses was found to depend on the frequency at which the forcing is applied. Indeed, as the frequency varied from the shear layer's natural frequency to lower frequencies, the spatial structure of the corresponding responses was increasingly concentrated on the wake of the airfoil, whereas as it varied to higher frequencies it concentrated on the suction side

boundary layer of the airfoil.

A different behaviour was identified for the blunt trailing edge airfoil. In this case the resolvent spectrum was found to peak at the frequency of the Karman vortex shedding. Furthermore, the amplification rate was reduced by almost an order of magnitude at the range of frequencies close to the natural frequency of the shear layer found earlier, an indication of the reduced receptivity of the separation bubble due to the lock-in effect.

Finally, it was demonstrated how the resolvent analysis can be used to make accurate predictions of the spectra at any point in the flow field, based on point measurements. It was shown that when the first singular value is several orders of magnitude larger than the rest, an approximation can be made which allows only the corresponding optimal response to be used when reconstructing the velocity spectrum. Its coefficient (i.e. the projection of the forcing to the forcing basis) can then be estimated for every frequency using the velocity spectrum of a selected calibration point. The location of this point is important; it should be located in a highly energetic area of the flow where the mode corresponding to the given frequency is not zero, otherwise, as was demonstrated, the model fails to accurately estimate the projection coefficients.

Chapter 5

Analysis of the attached boundary layer on the airfoil.

5.1 Introduction

As has been demonstrated in the previous two chapters, the separation bubble which forms on the suction side of the airfoil significantly affects the flow characteristics. Downstream of the straight trailing edge case the flow is dominated by the shedding originating from the separated shear layer, whereas when the truncated trailing edge is introduced, the Kárman shedding dominates the wake, with a noticeable effect on the separated flow.

In this chapter, a numerical tripping method was implemented and applied on the boundary layer developing on the suction side, in order to trigger transition earlier and keep the boundary layer attached. The tripping was applied as a boundary condition on the surface of the airfoil at a thin stripe in the spanwise velocity component. The thin stripe is located shortly downstream of the leading edge, between $X/C = 0.04$ and 0.06, which, as the results of chapter 4 suggest, is within the area of maximum sensitivity of the flow field. Thus, any perturbation introduced there is expected to have a large impact on the flow field.

5.1.1 Numerical details of the tripping method

The tripping method applied, was developed and used by Schlatter and Örlü (2012) in boundary layers and by Hosseini et al. (2016) in the flow around a NACA-4412 airfoil. A brief description of the method will be given here, but for a more detailed analysis the reader is referred to the aforementioned papers. The spanwise velocity at the tripping location has the generic form:

$$g(z,t) = AU_\infty \left([1 - b(t)]\, h(z)^i + b(t) h(z)^{i+1} \right) \tag{5.1}$$

where A is the, user-defined, amplitude of the forcing and $h(z)$ is a randomly generated harmonic function. The value of A was chosen to be 0.05 (i.e. the tripping velocity will attain a maximum value of 5% of the free stream velocity). The harmonic function is generated as a sum of harmonic modes with unit amplitude and wavenumbers smaller than a user defined value z_s. The following auxiliary functions were used:

$$b(t) = 3p(t)^2 - 2p(t)^3$$

$$p(t) = \frac{t}{t_s} - i$$

and

$$i = int\left(\frac{t}{t_s}\right)$$

where t_s defines the time scale of forcing. Thus, at each consecutive time interval of length t_s, the boundary forcing is calculated as a 3^{rd} order interpolation between the randomly generated functions $h(z)^i$ and $h(z)^{i+1}$. This ensures a smooth transition between the consecutive harmonic functions as they are randomly generated when i changes (i.e. when we move to the next time interval of length t_s). Figure 5.1 shows the temporal spectrum of the forcing. The energy distribution of the forcing is constant until the cut-off frequency $f_c = \frac{1}{t_s}$, which means that the forcing does not introduce any artificial modes in the flow field. For the results presented in this

chapter the tripping time scale t_s was chosen to be $5\delta t$, where δt is the simulation time step. Thus, the cut-off frequency is 20% of the sampling frequency, as can be seen in Figure 5.1. It must be pointed out that the specific selection of the forcing time scale is not of major importance, as long as it covers the flow field's bandwidth (i.e. the forcing time scale is able to be captured by the flow field in order to have the desired effect). In the current context the flow field's bandwidth doesn't extent to more than $^1/_{100}$ of the sampling frequency. Thus, in order for the forcing to be able to be "felt" by the flow field we should have $f_c \geq 0.01 f_s$ which justifies the current selection.

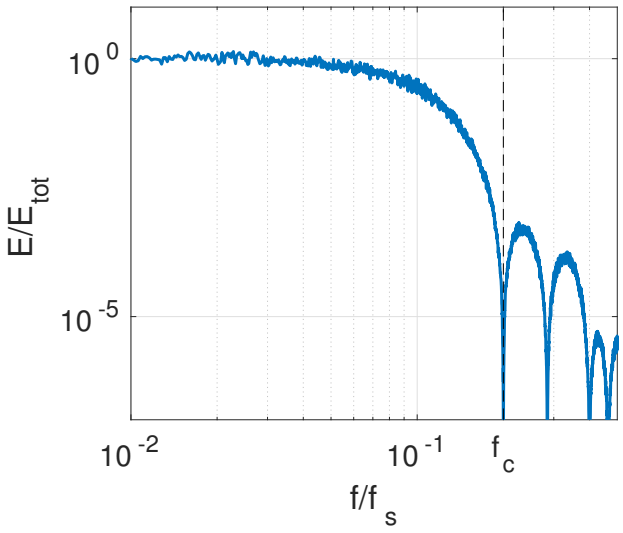


Figure 5.1: Temporal spectrum of the tripping forcing. The frequencies are normalized by the sampling frequency of the simulation (i.e. the inverse of the time-step). As can be seen the spectrum is constant until the user specified cut-off frequency $f_c = 0.2 f_s$, which means that no additional/artifical modes are introduced in the flow field.

Unlike the naturally developing flow, for the tripped boundary layer there are not any previous experimental or numerical results to serve as validation. To check the resolution, we compared the relative size of a characteristic length scale of the computational domain with a characteristic flow length scale (similarly to what was done in chapter 2). The smallest flow length scale is of the order of the Kolmogorov

length scale η defined as:

$$\eta = \left(\frac{\nu^3}{\epsilon}\right)^{1/4}$$

where ν is the kinematic viscosity and ϵ the local dissipation rate. The dissipation rate is calculated using the pseudo-dissipation formula given by

$$\epsilon = \nu\left\langle \frac{\partial u_i}{\partial x_j}\frac{\partial u_i}{\partial x_j}\right\rangle$$

which according to Pope (2001) is a very accurate approximation of the true dissipation[1]. For the characteristic grid length scale, the cubic root of the cell volume has been used. Contours of this ratio are plotted in Figure 5.2 for the straight trailing edge airfoil, and it can be seen that the ratio does not exceed 2.5, which is sufficient for DNS quality data (Pope (2001)).

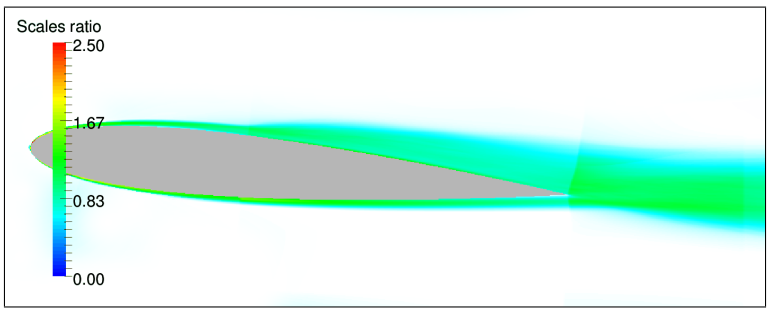


Figure 5.2: Ratio of the local characteristic cell size to the Kolmogorov length scale.

5.2 Time-averaged velocity fields

In this section the effect of the boundary layer tripping on the flow field will be studied for the straight and blunt trailing edge airfoils. In Figure 5.3 the time-

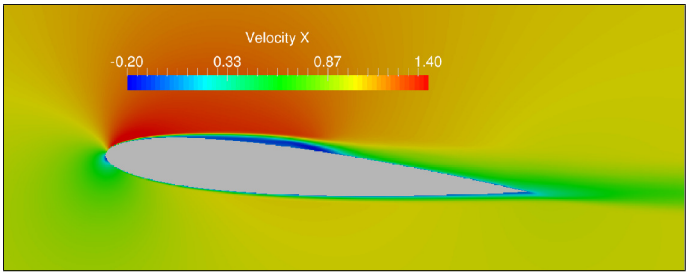
[1]The true dissipation from the turbulent kinetic energy budget is given by $\epsilon_{true} = \nu\left\langle \frac{\partial u_i}{\partial x_j}\frac{\partial u_i}{\partial x_j}\right\rangle - \nu\frac{\partial^2\langle u_i u_j\rangle}{\partial x_i \partial x_j}$. The second term is for most of the cases more than 2 orders of magnitude smaller than the first (Pope (2001)) and can be ignored.

averaged streamwise velocity fields are plotted for the untripped and tripped cases for the straight and blunt trailing edges. The separation bubble which can be seen on the airfoil in Figures 5.3a and 5.3c has been suppressed in Figures 5.3b and 5.3d, giving rise to an attached flow around the airfoil. As can be observed, the tripping affects equally the suction side boundary layer of both airfoils, but it does not seem to have an effect in the recirculation zone right after the trailing edge of the flatback airfoil.

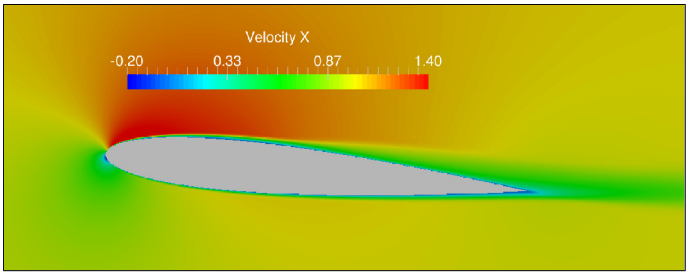
The boundary layers of the two cases are also expected to be modified. In Figure 5.4 the boundary layer profiles at the mid span are plotted for the straight trailing edge airfoil. The profiles streamwise locations are slightly upstream of the trailing edge, from $X/C = 0.83$ to $X/C = 0.97$. It can be observed that close to the wall the untripped airfoil's boundary layer shows higher velocity values (implying higher skin-friction values) while the opposite is true for the outer region. Velocity profiles closer to the tripping location will be presented later.

The suppression of the separated bubble also has a direct effect on the forces exerted on the airfoil. While the lift at the straight trailing edge airfoil drops by a mere 2.2%, from $C_{L,untripped} = 0.589$ to $C_{L,tripped} = 0.576$, the drag drops by 18.5%, from $C_{D,untripped} = 0.027$ to $C_{D,tripped} = 0.022$, leading to a net increase of the lift-to-drag ratio by approximately 20%, from 21.81 to 26.18. The effect of tripping on the forces is aptly demonstrated in Figure 5.5, where time series of the lift and drag coefficients (Figures 5.5a and 5.5b respectively) are plotted for the straight trailing edge and for a time window covering the activation of the tripping. It can be observed that after a short transition period, the separated boundary layer attaches and the force coefficients stabilize around the aforementioned mean values.

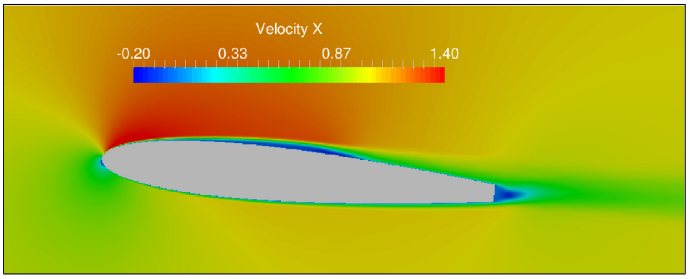
The streamwise and cross-stream velocity fluctuations are shown in Figures 5.6 and 5.7 for the straight and blunt trailing edge airfoils respectively. As can be seen, the suppression of the shear layer shedding has significantly reduced the energy of the turbulent fluctuations. The maximum value of the fluctuations when boundary layer tripping is employed is found to be approximately half of that in the naturally



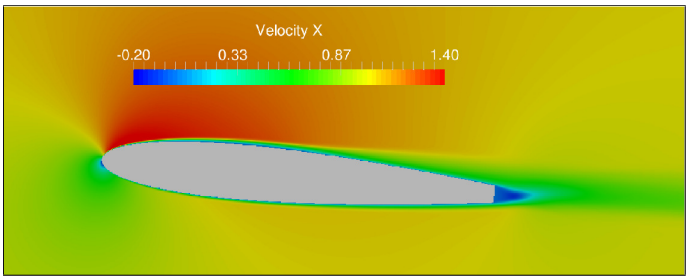
(a) Untripped airfoil - Straight TE.



(b) Tripped airfoil - Straight TE.



(c) Untripped airfoil - Blunt TE.



(d) Tripped airfoil - Blunt TE.

Figure 5.3: Mean streamwise velocity field for the untripped and tripped boundary layers for the straight and blunt trailing edge airfoils.

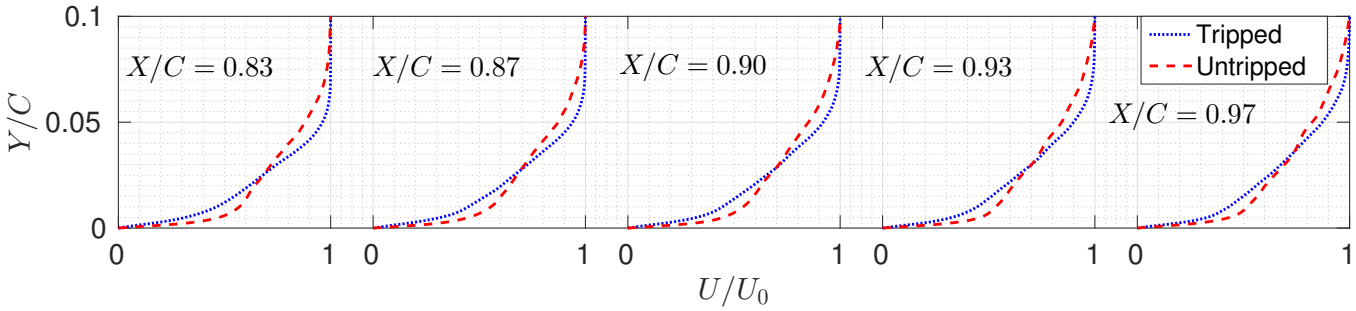
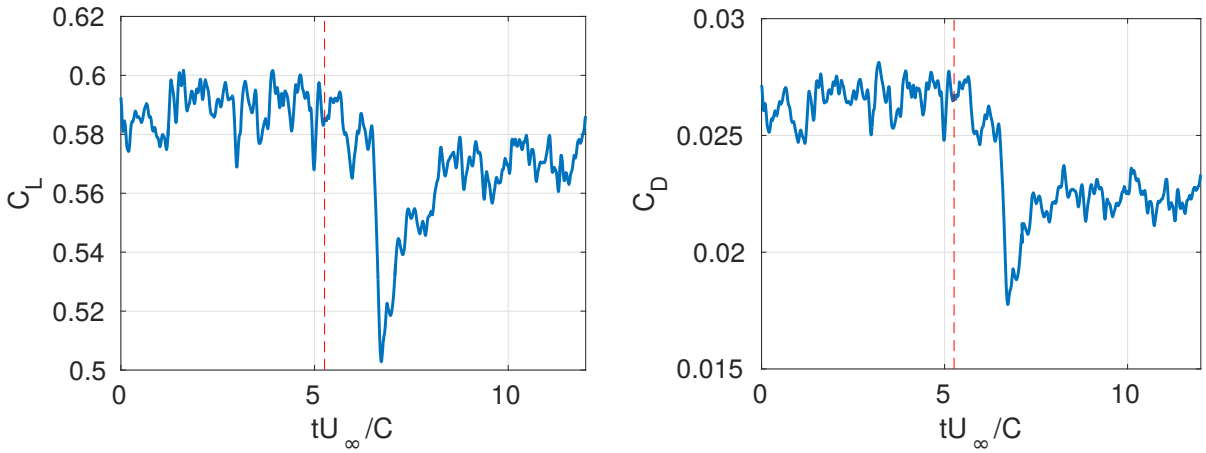


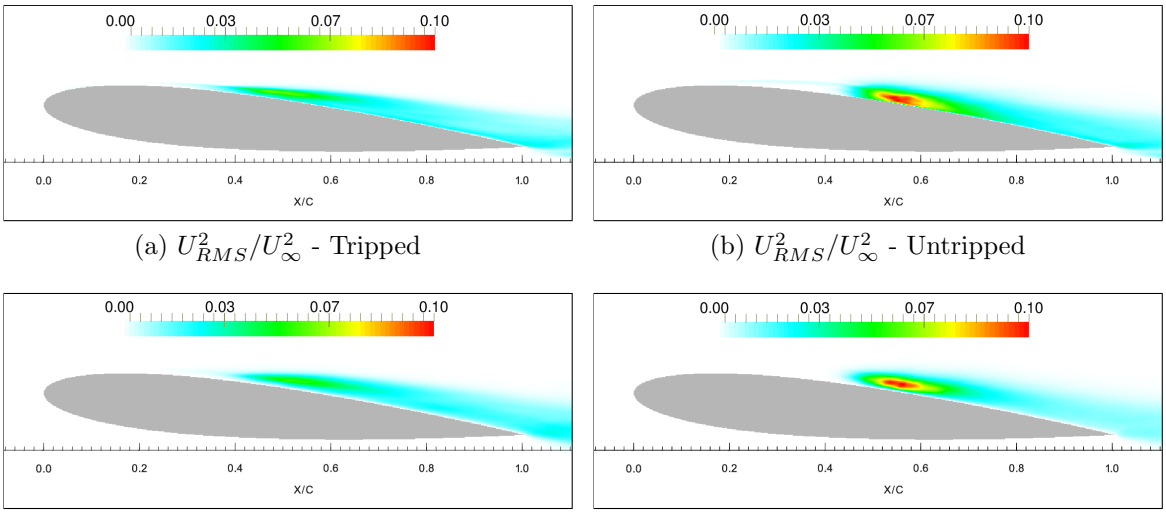
Figure 5.4: Boundary layer profiles at 5 different locations. The profiles have been normalized by the local maximum velocity at the edge of each profile U_0.



(a) Lift coefficient.

(b) Drag coefficient.

Figure 5.5: Lift and drag coefficients time series covering a period before and after the moment tripping is applied (red dashed line).



(a) U^2_{RMS}/U^2_∞ - Tripped

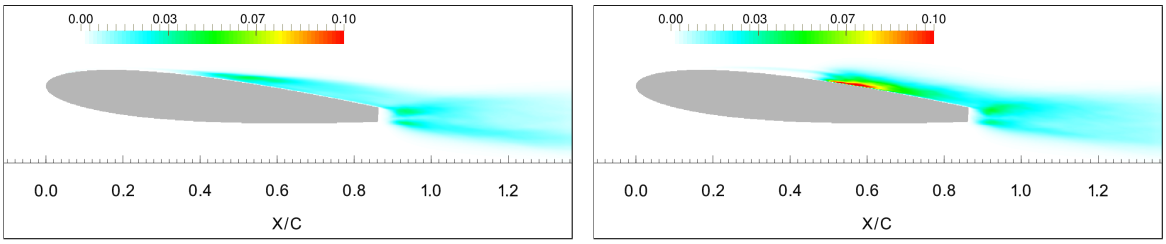
(b) U^2_{RMS}/U^2_∞ - Untripped

(c) V^2_{RMS}/U^2_∞ - Tripped

(d) V^2_{RMS}/U^2_∞ - Untripped

Figure 5.6: Streamwise (1^{st} row of figures) and cross-stream (2^{nd} row) fluctuations for the tripped (1^{st} column) and untripped (2^{nd} column) for the straight trailing edge airfoil.

developing flow field, a direct result of the suppression of the vortices which are shed from the separated shear layer.



(a) U^2_{RMS}/U^2_∞ - Tripped

(b) U^2_{RMS}/U^2_∞ - Untripped

(c) V^2_{RMS}/U^2_∞ - Tripped

(d) V^2_{RMS}/U^2_∞ - Untripped

Figure 5.7: Streamwise (1^{st} row of figures) and cross-stream (2^{nd} row) fluctuations for the tripped (1^{st} column) and untripped (2^{nd} column) for the blunt trailing edge airfoil.

Pressure and skin friction coefficients

The tripping is expected to affect the skin friction and pressure coefficients. In order to study the range of values that the coefficients take and how this range is affected by the tripping, their probability density functions (PDF) were calculated over the top surface. The samples for the calculation of the PDF have been collected in the spanwise direction and over time. In order to calculate the 2D PDFs, the streamwise direction was discretized using 200 points on the airfoil's surface, while 30 bins where used for the corresponding values of C_f and C_P. Due to the large variation of both C_P and C_f from the leading to the trailing edge of the airfoil, using the same bins at each location would not give satisfactory results. For this reason, for each location x, the values of the bins were selected to vary between $-3\sigma(x)$ and $3\sigma(x)$ with respect to the mean value $\mu(x)$ (see Jones (2008)) ($\sigma(x)$ and $\mu(x)$ are the standard deviation and mean values respectively at x). The values of the bins'

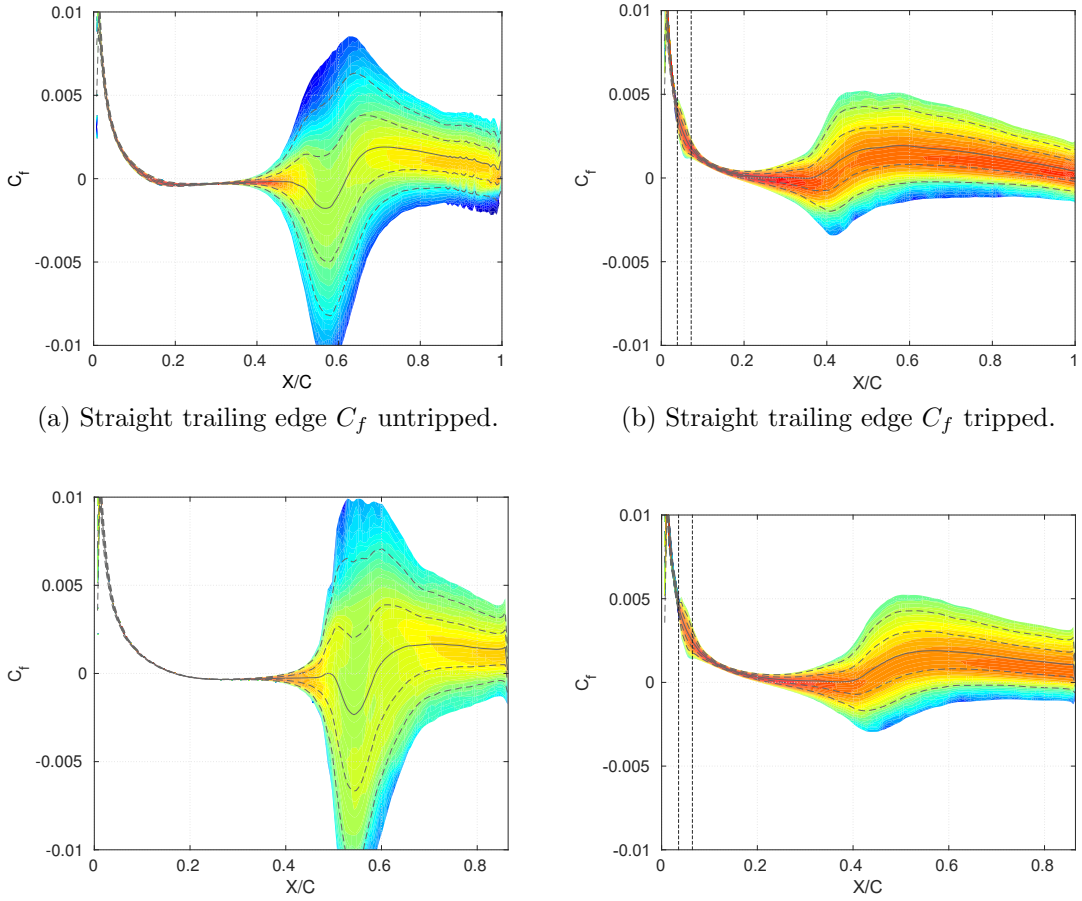
edges are then given by:

$$C_{f,P}(x,i) = \mu(x) - 3\sigma(x) + \frac{i-1}{29}6\sigma(x), \;\; i = 1, 2..., 30 \tag{5.2}$$

The number of data in each bin is then normalised by the bin's area $\delta x \delta C_{f,P}$ and the total number of data. While the bins in the streamwise direction have uniform length, which is equal to $\delta x = C/200$, the length of the bins for the values of $C_{f,P}$ depends on $\sigma(x)$ and is given by $\delta C_{f,P} = \frac{1}{29}\sigma(x)$. Thus a final normalisation of the PDF with $\sigma(x)$ is required to make the PDF integrate to 1.

Figure 5.8 shows the skin friction probability density functions (PDF) for the straight and blunt trailing edge airfoils with and without tripping. The extent along the vertical axis of the PDFs is a measure of their variance, thus the locations where the PDF appears to be a single line are regions of extremely low variance and thus almost steady flow. On the contrary, regions where the values of the PDFs are more spread imply a higher temporal and spanwise variation of the corresponding values. As Figures 5.8a and 5.8c suggest, in the untripped boundary layer the values are to a large extent almost steady, until approximately $X/C = 0.4$, where the shear layer shedding intensity starts to grow rapidly. In the tripped cases, seen in Figures 5.8b and 5.8d, the perturbations introduced close to the leading edge lead to an initially larger spread of the PDF values. As we move, though closer to what would be the separation point, the difference is striking with the variation being much smaller, and the range of values much more clustered around the mean.

An interesting feature in Figures 5.8b and 5.8d is the presence of a region, approximately between $X/C = 0.15 - 0.3$, where the average C_f value is almost zero (it can be seen that the PDF is symmetrically placed around zero). The negative values of C_f which give rise to the zero mean value, imply the presence of instantaneous flow reversal appearing locally, which indicates the presence of incipient separation of the boundary layer. Indeed as Figures 5.9 and 5.10 suggest for the straight trailing edge airfoil, the velocity profile becomes distorted close to the wall (Figure 5.9), and



(a) Straight trailing edge C_f untripped.

(b) Straight trailing edge C_f tripped.

(c) Blunt trailing edge C_f untripped.

(d) Blunt trailing edge C_f tripped.

Figure 5.8: Probability density function of C_f for the untripped (5.8a and 5.8c) and tripped (5.8b and 5.8d) airfoils. The solid line in each plot shows the mean value, while the dashed lines show the $\pm 1\sigma$ and $\pm 2\sigma$ ranges around the mean. The vertical dashed lines in Figures 5.8b and 5.8d indicate the range where the tripping was applied.

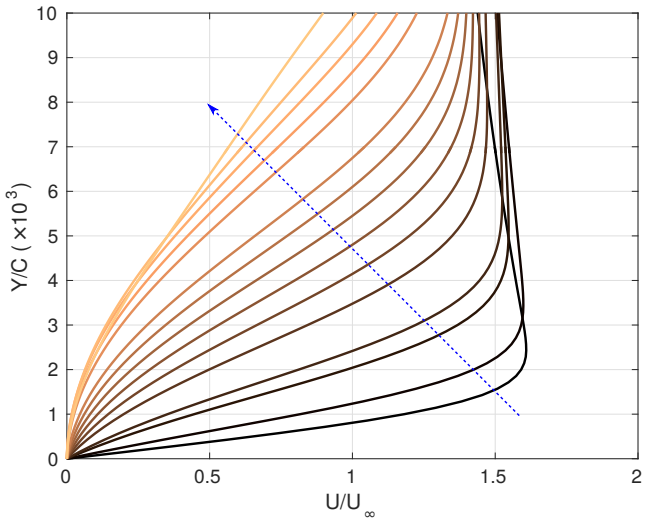


Figure 5.9: Tangential velocity profiles at the airfoil's surface (shown up to $Y/C = 0.01$) for the straight trailing edge case. The darker colours indicate a smaller X/C with $0.01 \leq X/C \leq 0.32$. The dashed blue arrow indicates increasing X/C. The exact locations are $X/C = 0.01, 0.02, 0.05, 0.1, 0.12, 0.14, 0.16, 0.18, 0.22, 0.24, 0.26, 0.28, 0.32$.

at approximately $X/C = 0.32$ it approaches vertically the wall (i.e. $C_f = 0$), but then further downstream it re-accelerates without separating (Figure 5.10). Similar observations were also made for the blunt trailing edge airfoil.

The PDFs of the pressure coefficient C_P are shown in Figure 5.11. It is worth noting that the pressure plateau, which can be seen for the straight trailing edge case in Figure 5.11a between approximately $X/C = 0.2$ and 0.55, has vanished in Figure 5.11b and C_P follows a gradual recovery towards the free stream pressure, with the same being true for the blunt trailing edge airfoil. This is in accordance with the significantly lower drag observed in the tripped boundary layer case. Due to the angle of attack, this negative pressure, when integrated over the surface of the airfoil, creates a significant drag force component, whose effect is mitigated when tripping is applied.

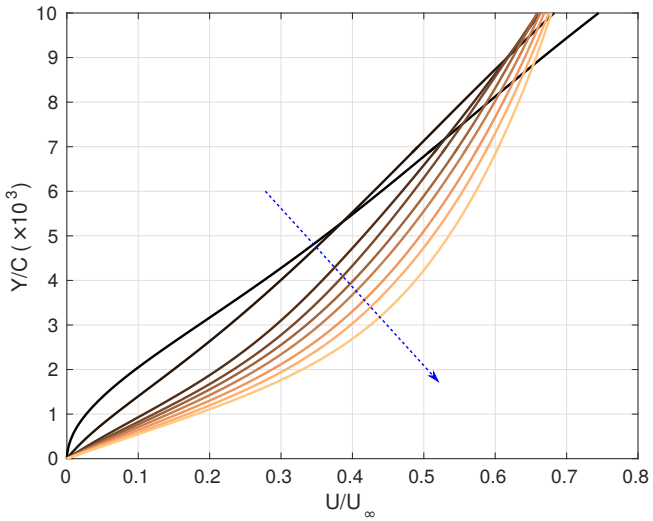
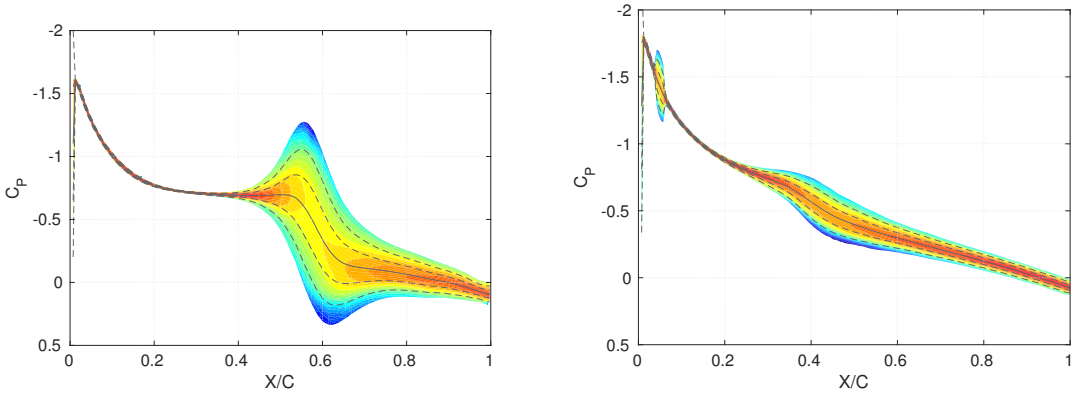


Figure 5.10: Tangential velocity profiles at the airfoil's surface (shown up to $Y/C = 0.01$) for the straight trailing edge case. The darker colours indicate a smaller X/C with $0.40 \leq X/C \leq 0.62$. The dashed blue arrow indicates increasing X/C. The exact locations are $X/C = 0.40,\ 0.44,\ 0.48,\ 0.50,\ 0.52,\ 0.54,\ 0.56,\ 0.58,\ 0.62$.



(a) Straight trailing edge C_P untripped.

(b) Straight trailing edge C_P tripped.

(c) Blunt trailing edge C_P untripped.

(d) Blunt trailing edge C_P tripped.

Figure 5.11: Probability density function of the pressure coefficient fluctuations for the untripped (5.11a and 5.11c) and tripped (5.11b and 5.11d) airfoils.

Dynamic behaviour of the tripped boundary layer

Figure 5.9 suggests the creation of inflectional boundary layer profiles on the suction side of the airfoil, which owing to Rayleigh's theorem (Rayleigh (1879)), provide the inviscid mechanism according to which disturbances may be amplified. In Figure 5.12 we plot an instantaneous snapshot of the streamwise velocity for the straight trailing edge airfoil. The red half-circles on the suction side of the airfoil delineate large-scale structures which appear to originate from the boundary layer. As these structures are very close to the airfoil's wall, they are expected to affect the pressure on the suction side wall of the airfoil. It is expected that as the low pressure cores of these vortices propagate over the airfoil, the corresponding pressure signal on the wall will show a periodic behaviour with a period $T = \ell/U_v$, where ℓ is the length scale of the vortices and U_v is their propagation velocity.

In Figure 5.13 the spectrum of the spanwise averaged pressure signal is plotted against X/C on the airfoil's suction side, from time series of the pressure at all the wall faces of the airfoil. A clear peak can be observed at approximately $X/C = 0.45$, a location which coincides with the first appearance of the vortical structures in Figure 5.12. The spectral location of the peak is at $f = 9.16$ which corresponds to a period $T = 0.11$.

In order to measure the propagation velocity of the vortices, the spanwise and temporal cross-correlation of the pressure signal on the suction wall was calculated, with the reference signal located at $X/C = 0.45$ (i.e. where the spectrum in Figure 5.13 peaks). The cross-correlation is defined by:

$$\rho(\Delta x, \Delta t) = \frac{\langle p(x,t)p(x+\Delta x, t+\Delta t)\rangle_{t,z}}{\sqrt{\langle p^2(x,t)\rangle_{t,z}}\sqrt{\langle p^2(x+\Delta x, t+\Delta t)\rangle_{t,z}}} \tag{5.3}$$

where the $\langle\cdot\rangle_{t,z}$ indicate averaging in time and in the spanwise direction. The cross-correlation coefficient is plotted in Figure 5.14. Its interpretation is the following: if a vortex is propagating with a speed U_v, then after time Δt it will have travelled

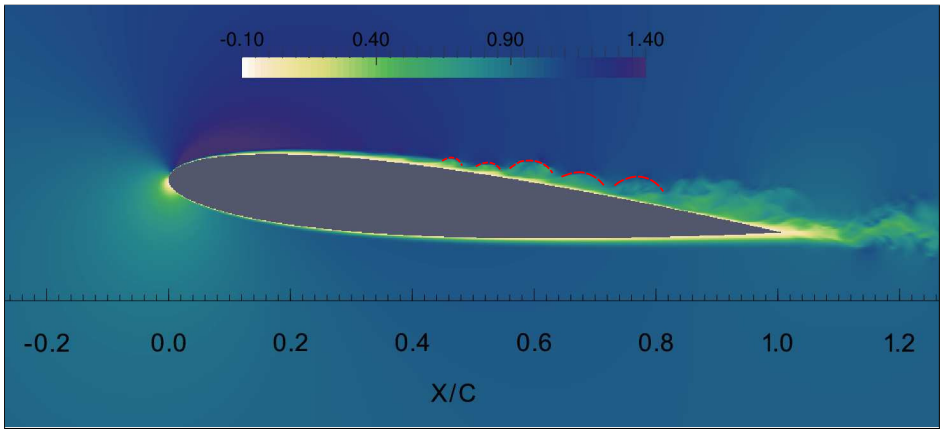


Figure 5.12: Instantaneous streamwise velocity field. The red curves delineate large scale structures.

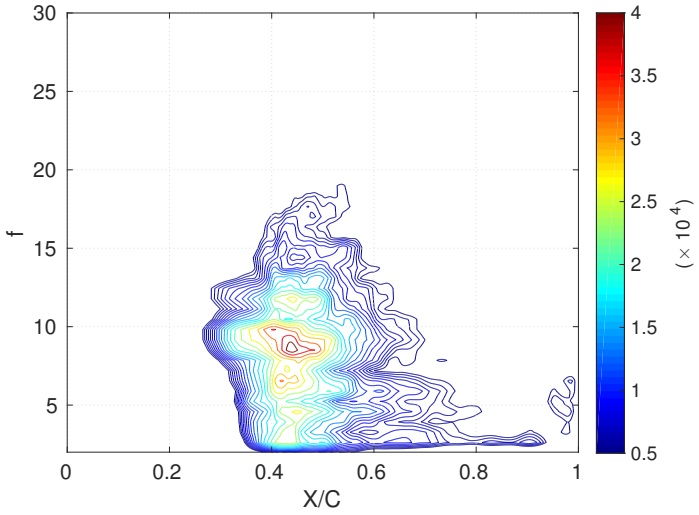


Figure 5.13: Spanwise averaged spectrum of pressure on the suction side.

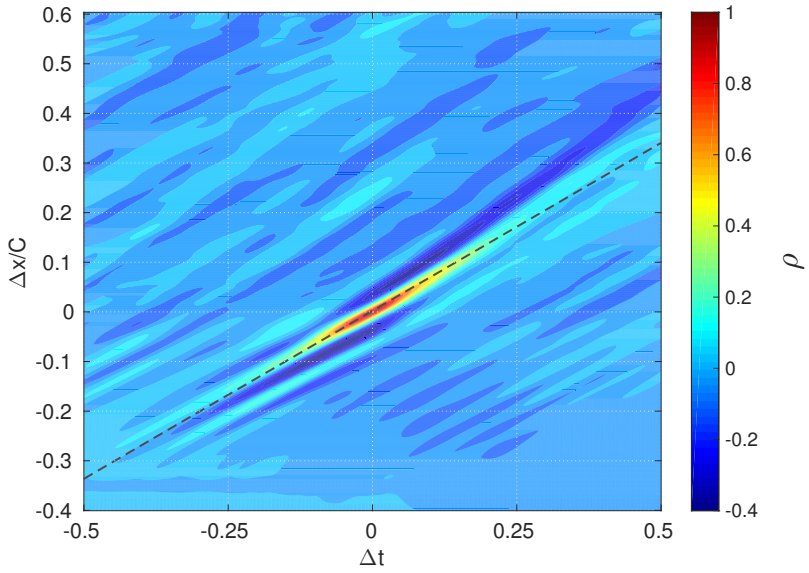


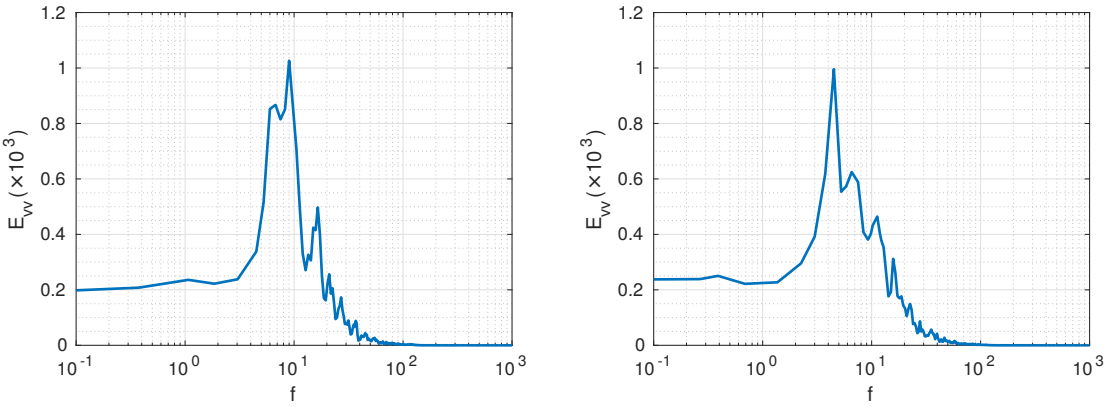
Figure 5.14: Spanwise averaged cross-correlation of the wall pressure on the airfoil's suction side. The reference signal is located at $X/C = 0.37$.

$\Delta x = U_v \Delta t$. Thus, the pressure signal at a point located at a distance Δx from the reference point, will have maximum correlation with it after time Δt. This is exactly what the tilted locus of the maximum values in Figure 5.14 illustrates. The gradient of the dashed line, which is aligned with the maximum values, gives the propagation velocity U_v of the vortical structures. This was found to be $U_v = 0.67$, and the length scale of the vortices is estimated to be $\ell = U_v T = 0.074$, a value which can be corroborated, up to a level of accuracy, by the size of the smaller structures seen in Figure 5.12 close to $X/C = 0.45$. The larger structures, which can be observed further downstream, appear to have higher wavenumbers and, as expected, lower frequencies.

In Figure 5.15 the cross-stream velocity spectra are plotted at two locations on the suction's side boundary layers. The first probe is located at $X/C = 0.47$,$Y/C = 0.035$, which is the location where smaller structures in Figure 5.12 are formed, and the second probe is at $X/C = 0.68$,$Y/C = 0.012$, which is at the location of the larger structures. A clear peak at $f = 9.0$ is also observed in this case (very close to the peak in Figure 5.13) which further downstream, in Figure 5.15b, attenuates and

a peak at its half subharmonic, at $f = 4.5$, appears. This behaviour is in agreement with Figure 5.12, where the initially small vortices, which form at approximately $X/C = 0.45$, evolve further downstream to larger ones at $X/C = 0.6$ with smaller frequency.

From the analysis presented in this section, it seems that a similar dynamic phenomenon is in place here, as the one identified in chapter 3. In that chapter a strong Kelvin-Helmholtz instability, arising from the shear between the reversed flow in the separation bubble and the free stream velocity gave rise to strong fluctuations. In the tripped case the Kelvin-Helmholtz mechanism appears again to be in place, albeit as a result of the inflectional velocity profile (see the profiles in Figure 5.9). As was mentioned in chapter 4 the velocities ratio R across a shear region is directly related to the amplification rate of instabilities in this region. Due to absence of reverse flow in this case, the velocities ratio R is lower now, with its exact value at the point where the velocity profile approaches vertically the wall being $R = 1$ (whereas in the untripped case it exceeded the value of $R = 1.3$). Thus, while the same mechanism gives rise to a dominant frequency and its half subharmonic further downstream, the energies of these frequencies are much lower (the peak in Figure 3.2 is more than an order of magnitude larger compared to the peak in Figure 5.15).



(a) $X/C = 0.47$,$Y/C = 0.035$. (b) $X/C = 0.68$,$Y/C = 0.012$.

Figure 5.15: Cross-stream velocity spectra at two locations on the suction' side boundary layer.

5.3 Resolvent analysis - Straight Trailing Edge

The resolvent analysis presented in the previous chapter, has also been applied in the tripped airfoils. As shown in chapter 4, the presence of the laminar separation bubble in the straight trailing edge airfoil dominates the dynamic characteristics of the flow field. When tripping is applied and the separation bubble is suppressed, the resolvent spectrum is shown in Figure 5.16. Important differences can be observed when the plot is compared with Figure 4.2.

Firstly, the optimal singular mode appears to peak at a value which is more than an order of magnitude smaller. As was shown in the previous section, the absence of reverse flow greatly impedes the amplification characteristics of the Kelvin-Helmholtz mechanism which is in place both in the untripped and in the tripped cases. It it thus expected that this will affect the response characteristics of the flow-field, as was also demonstrated with the significantly lower values of the power spectral density of the velocity signals shown in Figures 5.15a and 5.15b.

Secondly, the location of the peak is different. While in the previous chapter, the peak was located at the natural frequency of the separated shear layer, in the present case it appears to be located at the sub-harmonic frequency (the peak in Figure 5.16 is at $\omega_{P,Trip} = 30$ or $f_{P,Trip} = 4.77$, 6% difference with the sub-harmonic found earlier from processing of DNS time series). As we saw earlier this frequency develops downstream of the airfoil and into the wake.

The latter observation should be made in conjunction with the behaviour of the second singular value (red dashed line in Figure 5.16). In this case, it takes significantly larger values, when compared to the untripped case, implying a higher contribution in the full response. It also shows a clear peak at the frequency of the shedding originating the suction side, at approximately $\omega_{2,Trip} = 56$ or $f_{2,Trip} = 9.0$, found in the previous section. In order to shed more light into this behaviour we need to look at the spatial structure of the responses at these frequencies.

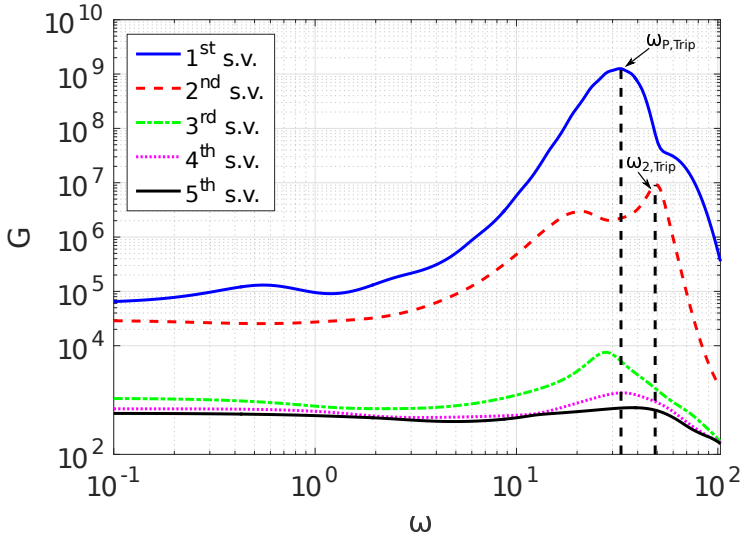
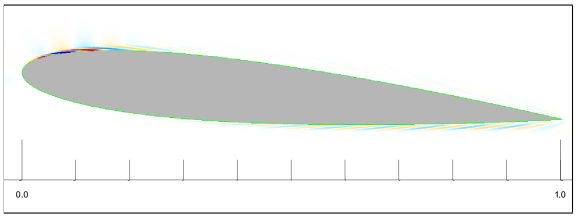


Figure 5.16: Singular value plot of the resolvent operator for the tripped straight trailing edge airfoil.

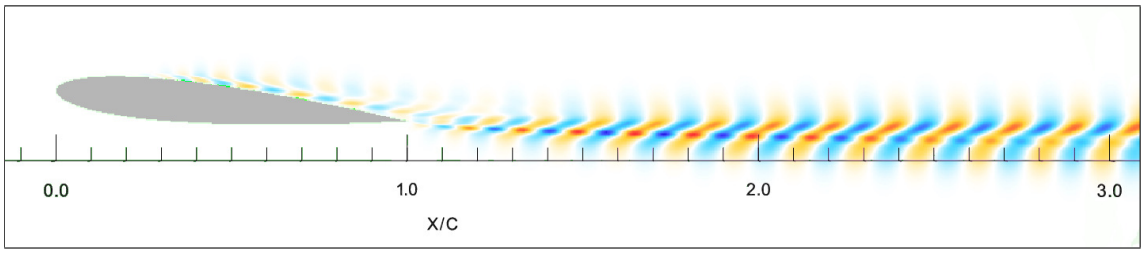
5.3.1 Resolvent modes

The spatial structure of the optimal forcings which correspond to the peak of the blue line in Figure 5.16 (at $\omega_{P,Trip}$) are shown in Figures 5.17a and 4.5a. Their behaviour appears to be identical to their counterparts in chapter 4, without any observable effect of the tripping on their behaviour. The responses on the other hand show a fundamental difference in their spatial distribution. We saw in the previous chapter that the optimal response of the flow field at the peak frequency was dominated by the structures originating from the separated shear layer. In this case though, as Figures 5.17b and 5.18b suggest, the stronger response appears in the wake of the airfoil and not on the boundary layer.

Continuing our analysis, we plot in Figure 5.19 the streamwise (Figure 5.19a) and the cross-stream (Figure 5.19b) components of the response of the first singular value at the frequency $\omega_{2,Trip}$, i.e. the frequency in which the second singular value peaks and the first one shows a sudden change in its slope. A fundamental difference can be observed between the spatial structures of the responses at the two frequencies. While the spatial support of the mode at $\omega_{P,Trip}$, seen in Figures 5.17b and 5.18b,



(a) Optimal forcing (X-component).



(b) Optimal response (X-component).

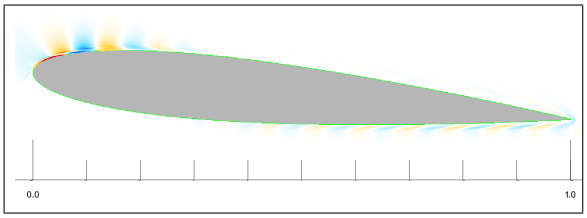
Figure 5.17: Streamwise component of the optimal forcing and response at the frequency $\omega_{P,Trip}$ showing the highest amplification rate.

was concentrated in the wake of the airfoil, in Figures 5.19a and 5.19b it can be seen that the response is mostly dominant on the boundary layer, with a significant attenuation in the wake.

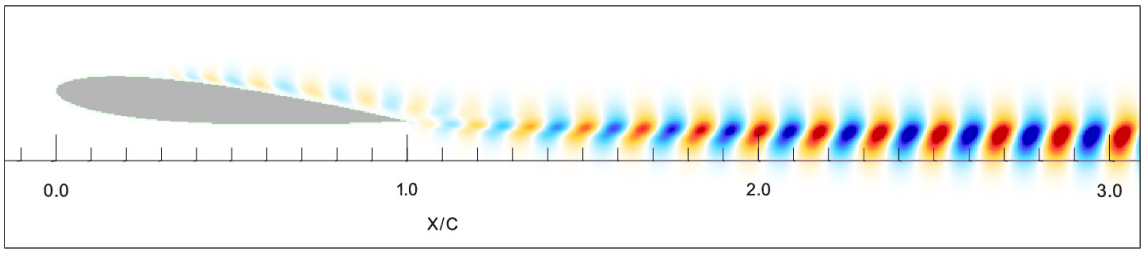
Lastly, in Figures 5.20a and 5.20b, the two components of the response corresponding to the peak of the second singular value, are shown. As can be observed, there are striking similarities between the fields shown in Figure 5.19 and the ones shown in Figure 5.20. Both of these fields appear to capture the shedding which was identified earlier to originate from the boundary layer.

Putting all the observations made hitherto together, the behaviour of the resolvent spectrum in Figure 5.16 can be explained. The behaviour that is being captured by the optimal singular value is related to the sub-harmonic of the shedding which develops in the second half of the airfoil and into the wake. This can be attributed to two factors.

The first one is the significantly reduced intensity of the boundary layer shedding, as demonstrated earlier in this chapter. The second one has to do with the way that the gains (i.e. the singular values) are calculated, which, as was presented in chapter



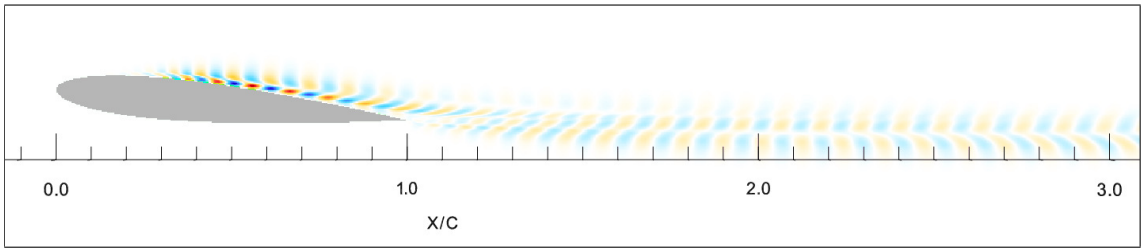
(a) Optimal forcing (Y-component).



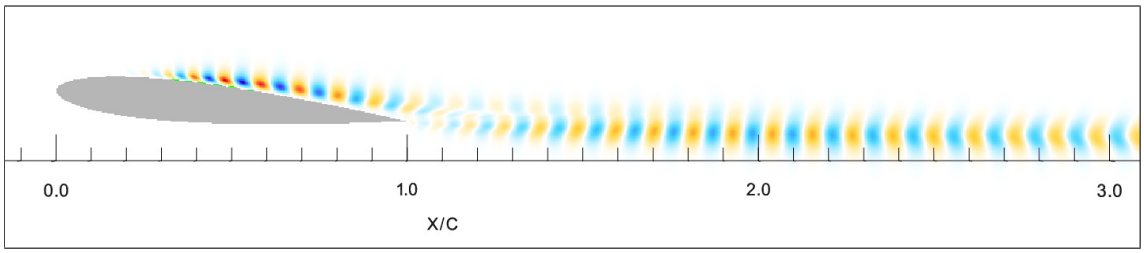
(b) Optimal response (Y-component).

Figure 5.18: Cross-stream component of the optimal forcing and response at the frequency $\omega_{P,Trip}$ showing the highest amplification rate.

4, are the result of the minimization of the ratio of the norm of the response over the norm of the forcing, which results in the singular value decomposition of the resolvent matrix. It is thus important to explicitly state the dependence of the result on the definition of the aforementioned norms. In both this chapter and the previous one, the norm that was used was the integral of the energy of the variable over the whole field. When the boundary layer separates resulting in the strong shedding of the shear layer, this integral is dominated by the shear layer shedding fluctuations and the resolvent spectrum in Figure 4.2 peaks at the shear layer's natural frequency. On the other hand, in the present case, due to the attenuation of the shedding energy and to the larger effect of the wake in the integral (because of its largest size compared to the airfoil), the resolvent peaks at the lower frequency, which characterizes the wake. The shedding of the boundary layer in this case is mostly captured by the second singular value, as the clear peak at $\omega_{2,Trip}$ indicates. Interestingly though, its effect is also captured by the first singular value as evidenced by the kink at $\omega_{2,Trip}$ in Figure 5.16. As we saw in Figures 5.19 and 5.20 the response at this frequency is contained on the suction side of the airfoil, and it captures the



(a) Streamwise component.



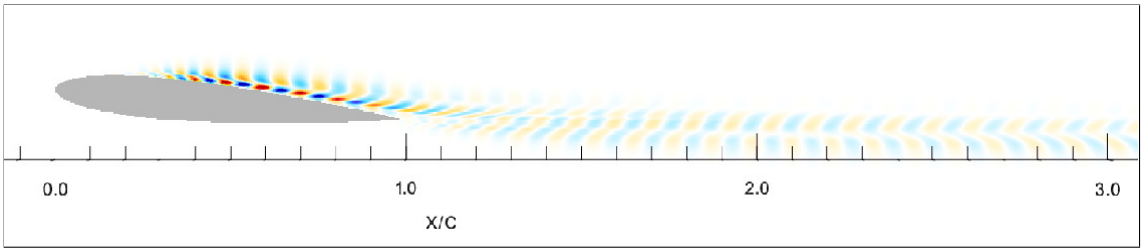
(b) Cross-stream component.

Figure 5.19: Streamwise (5.19a) and cross-stream (5.19b) components of the optimal response at the frequency $\omega_{2,Trip}$.

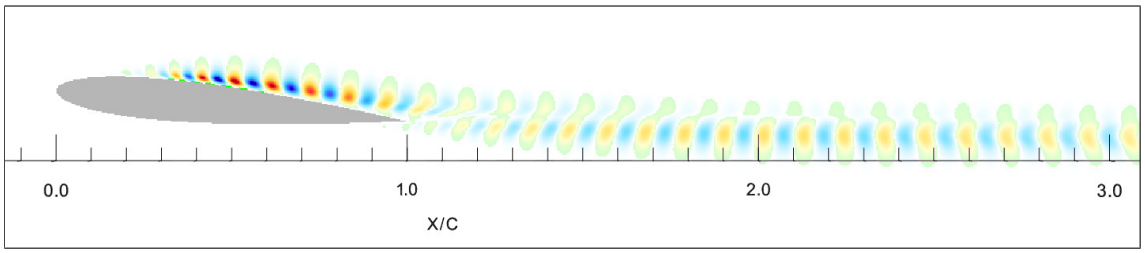
shedding behaviour of the incipient separation of the boundary layer. Thus, in the present case of an attached boundary layer, when the optimization of the gain is performed in the whole domain, there is a notable shift in the location of the most energetic response of the flow field, from the airfoil's suction side to the wake.

To further investigate this behaviour and to strengthen the aforementioned argument, the resolvent analysis was performed again in a smaller optimization domain. The optimization domain (i.e. the domain where Q_u is defined) in this case, shown in Figure 5.21, covered the area on the suction side of the airfoil, in order to find the set of responses that maximise the energy on this specific part of the flow field, and ignore the response energy in the wake.

The resulting spectrum of the resolvent operator is shown in Figure 5.22, overlapped on the spectrum of the resolvent on the whole domain. The dashed line indicates the frequency $\omega_{2,Trip}$. The values of the gains are much smaller as expected from the formulation of the problem in this case. A noticeable difference in Figure 5.22, when compared with Figure 5.16, is that the behaviour of the first two singular values appears to be reversed. The dominant singular value appears



(a) Streamwise component.



(b) Cross-stream component.

Figure 5.20: Streamwise (5.20a) and cross-stream (5.20b) components of the response at the frequency $\omega_{2,Trip}$ corresponding to the second singular value.

to peak at $\omega_{2,Trip}$ whereas the second largest shows the kink that was previously observable in the first singular value. Furthermore as can be seen in Figure 5.23, the spatial distribution of the optimal mode at $\omega_{2,Trip}$ is, in this case, localized at the boundary layer of the airfoil. These observations corroborate the argument made earlier. It is thus important to emphasize the dependence of the resolvent analysis on the optimization domain, which as we saw can significantly affect the results and potentially lead to their misinterpretation.

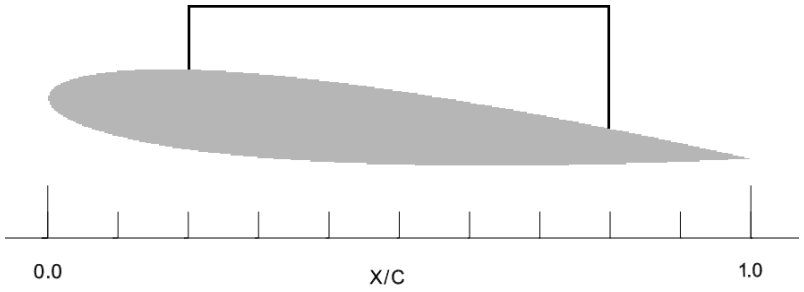


Figure 5.21: Optimization domain for the resolvent analysis focused on the suction side.

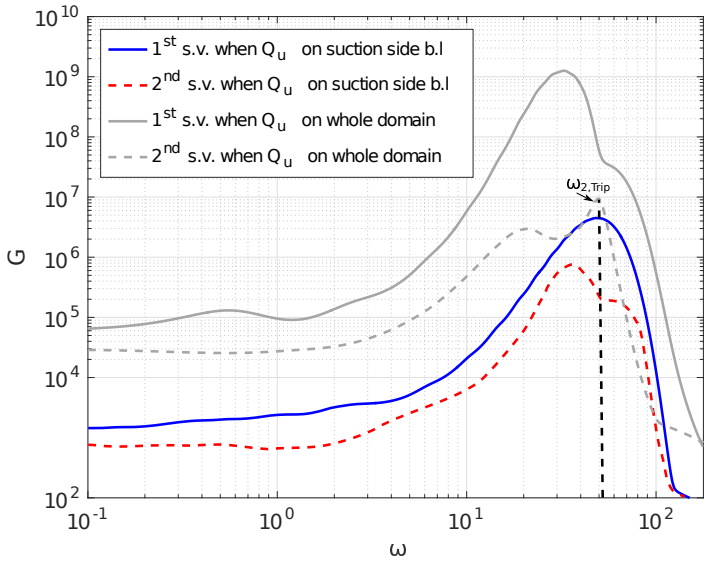


Figure 5.22: Resolvent spectra with different optimization domains Q_u. The grey lines correspond to the previous case where the optimisation was performed on the whole domain, while the coloured lines correspond to the current case where the optimisation covers only the suction side of the airfoil.

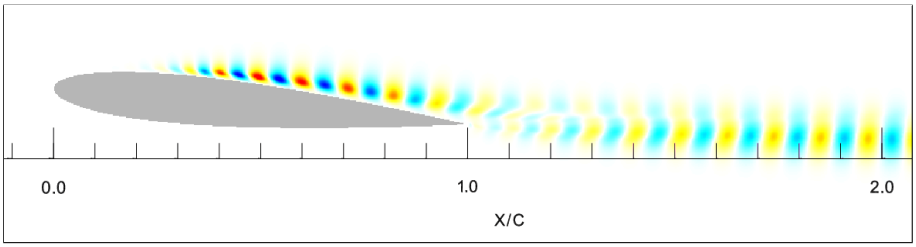


Figure 5.23: Cross-stream component of the optimal response at the frequency $\omega_{2,Trip}$ when the domain shown in Figure 5.21 is used in the optimization process.

5.4 Resolvent analysis - Blunt Trailing Edge

In this section we present the results of the resolvent analysis for the blunt trailing edge airfoil. In Figure 5.24 the spectrum of the resolvent operator is shown, with both Q_u and Q_f defined in the whole domain. The overall behaviour of the spectrum is similar to the one seen earlier, including the irregularity observed close to the peak frequency $\omega_{2,Blunt}$ of the second singular value, which was also observed in the straight trailing edge case. The 1^{st} singular value peaks at $\omega_{P,Blunt} = 28.73$

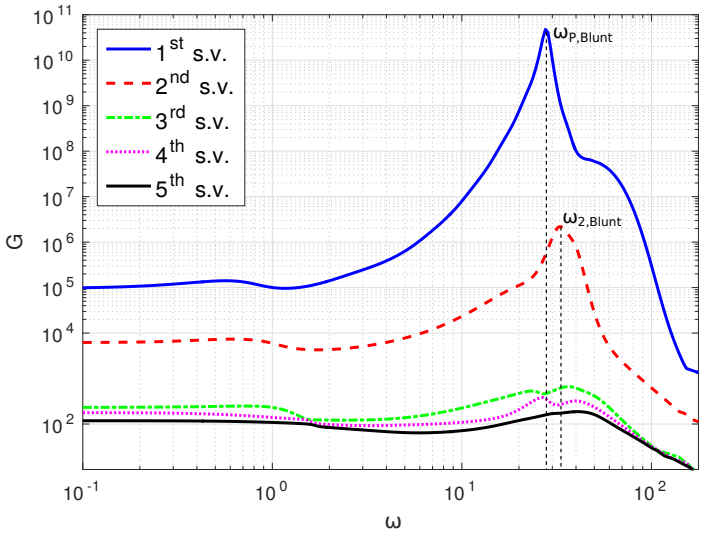


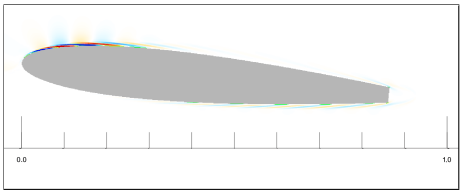
Figure 5.24: Singular value plot of the resolvent operator for the blunt trailing edge airfoil.

or $f_{P,Blunt} = 4.52$ which almost perfectly matches the frequency of the Kárman shedding which originates from the truncated trailing edge.

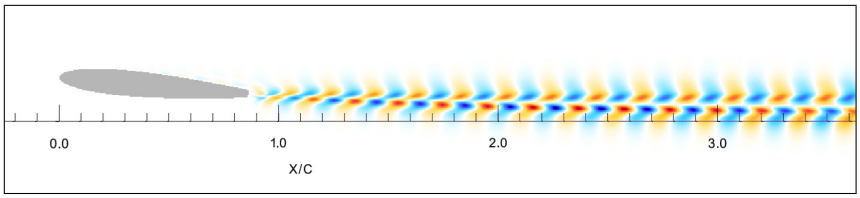
An important difference with the previous cases (both in chapter 4 and in the present chapter) is that the plot in Figure 5.24 shows a much sharper and smoother peak around the dominant frequency $\omega_{P,Blunt}$. This should be contrasted with the highly irregular and concave nature of the peak in the untripped case shown in Figure 4.12. It was postulated there that these irregularities were a direct result of the interaction between the two forms of shedding present in that flow field, one from the separated shear layer and one from the truncated trailing edge. In the current case a very smooth graph can be observed, whose convex behaviour, clearly indicates a resonance effect as we get closer to $\omega_{P,Blunt}$. Furthermore due to the absence of a strong shedding from the boundary layer, the aforementioned interactions are attenuated and the resolvent spectrum plot appears to be much smoother.

5.4.1 Resolvent modes

In Figures 5.25 and 5.26 the modes which correspond to the peak frequency $\omega_{P,Blunt}$ of the optimal gain are shown, with the streamwise forcing and response shown in Figure 5.25 and the corresponding cross-stream components shown in Figure 5.26. Both of these figures, and their corresponding sub-figures show the expected



(a) Optimal forcing $\hat{f}_x$.

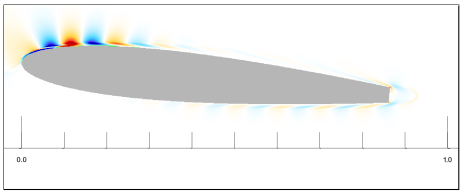


(b) Optimal response $\hat{u}_x$.

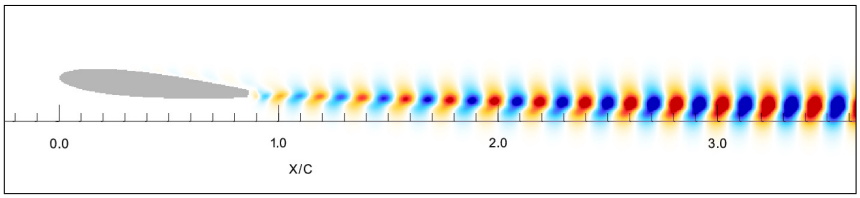
Figure 5.25: Streamwise component of the optimal forcing $\hat{f}_x$ and response $\hat{u}_x$ at the frequency $\omega_{P,Blunt}$ showing the highest amplification rate.

behaviour of the bluff body shedding also seen in the untripped flatback airfoil, with the wake mode dominating the response.

As was mentioned in the beginning of this section, a qualitatively similar behaviour is observed between Figures 5.16 and 5.24, at the point where the second singular value peaks, at $\omega_{2,Blunt}$. The corresponding sub-optimal modes at this frequency are plotted in Figure 5.27. Unlike the modes shown in Figure 5.20, where the response was located, almost in its entirety, on the suction side, in this case the distribution appears to be equally located both in the wake and the suction side of the airfoil. The response originates from the boundary layer and propagates downstream, with its amplitude initially increasing and then starting to attenuate. The likely cause of this behaviour, i.e. the presence of the response in the wake, which didn't exist in the straight trailing edge, is the different stability characteristics of



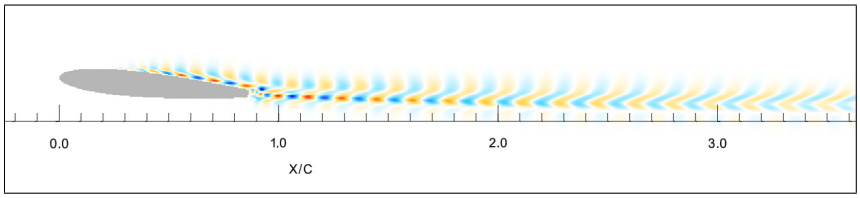
(a) Optimal forcing $\hat{f}_y$.



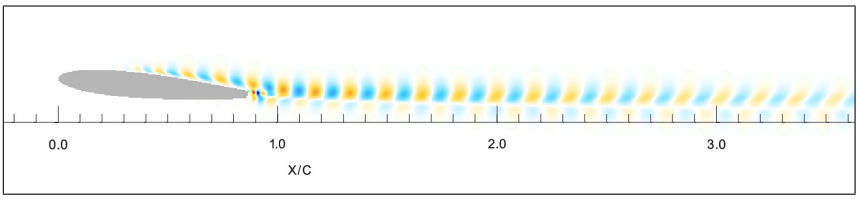
(b) Optimal response $\hat{u}_y$.

Figure 5.26: Cross-stream component of the optimal forcing $\hat{f}_y$ and response $\hat{u}_y$ at the frequency $\omega_{P,Blunt}$ showing the highest amplification rate.

the bluff body wake, which make it more recipient to disturbances, when compared to the wake of the straight trailing edge airfoil (bluff body wake as opposed to a mixing layer in the latter case). Despite the aforementioned difference, it appears that the mechanism causing this apparent interaction between the peak of the second singular value and the "step" of the first is the effect of the optimization domain seen earlier. A last characteristic, regarding Figure 5.27, is the local excitation of the separating shear layer at the point where the suction side boundary layer meets the truncated trailing edge. At this point the response appears to be maximized, nevertheless, its spatial extent is very small to have any significant impact on the gain and to be a major cause of the aforementioned behaviour of the resolvent spectrum at $\omega_{2,Trip}$.



(a) Response (X-component).



(b) Response (Y-component).

Figure 5.27: Streamwise 5.27a and cross-stream 5.27b components of the response $\hat{\boldsymbol{u}}$ at the peak frequency $\omega_{2,Blunt}$ corresponding to the second singular value.

5.5 Conclusions

In this chapter we investigated the dynamic characteristics of the flow fields created around airfoils with straight and blunt trailing edges, when the suction side boundary layer is tripped. The perturbations introduced by an artificial forcing were able to promote transition to turbulence earlier, which, due to the increased transfer of momentum to the wall, forced the boundary layer to remain attached, thus suppressing the formation of the separation bubble. This has a direct effect on the behaviour of the pressure and skin-friction coefficients on the airfoil,which as we saw have much steadier behaviour and weaker fluctuations. Furthermore, the pressure coefficient was found to gradually increase towards the free-stream pressure, with the pressure plateau observed in the separated case having vanished. This had a direct effect on the lift and drag coefficients leading to a net increase of the lift-to-drag ratio by about 20%.

Despite the absence of a separated flow, the pressure gradient was still strong enough to slow the flow down, causing incipient separation at certain locations on the wall. In these locations, which are located around $X/C = 0.35$, the time-averaged skin-friction close to the wall locally becomes zero. Further downstream

the flow accelerates but the profile is still distorted compared to the untripped case. The direct effect of this incipient separation is the creation of inflectional velocity profiles on the boundary layer, which provide the physical mechanism for instabilities to develop. Thus, despite the absence of the separated flow shedding seen in the previous chapters, we still get vortex shedding from the suction side boundary layer, albeit significantly attenuated. This then gives rise to the wake shedding at its first sub-harmonic frequency, following the same mechanism found in chapter 3.

The resolvent analysis of the two airfoils revealed different response characteristics compared to the previous chapter. In the straight trailing edge case, the resolvent spectrum appears to peak at the shedding frequency $\omega_{P,Trip}$ of the wake rather than the dominant frequency found on the boundary layer, with the corresponding spatial mode showing a clustering of its energy mostly in the wake region. The shear layer frequency is found to be the location where the second singular value peaks, having though a noticeable effect on the first singular value, in the form of a localized "step". This behaviour motivated a further study where the optimization domain was limited on the suction side of the airfoil. It was found that if the latter optimization domain is used, the optimal response shows indeed a peak at the suction side shedding frequency, and its corresponding mode is located on the suction side, with almost no presence in the wake. This behaviour is a direct effect of the much less energetic shedding from the suction side boundary layer, which makes the result dependent on the optimization area. The blunt trailing edge shows a much more pronounced resonance behaviour as the input frequency approaches the wake shedding frequency, as well as a similar behaviour regarding the second singular value.

Chapter 6

Conclusions

In this thesis the flow field around the NACA-0012 airfoil with 3 different trailing edges, has been numerically studied. The chord based Reynolds number was $50,000$ and the angle of attack was 5^o. The three different trailing edges were: the original straight trailing edge, a truncated blunt trailing edge and a trailing edge formed by cut-in triangular serrations. The topics that were investigated include:

- The time-averaged statistics of the flow-field with the different trailing edges.
- The spectral characteristics of the separation bubble, the wake and their interactions.
- A detailed study of the ability to apply mode extraction methods to investigate the spatial behaviour of the flow at the different frequencies of interest.
- The stability and sensitivity characteristics of the flow fields were thoroughly investigated using the dynamic mode decomposition and the analysis of the resolvent operator.
- The effect of the suppression of the separation bubble on the flow and on its dynamical characteristics.

6.1 Major findings

6.1.1 The flow-field around the airfoils

At the simulated Reynolds number and angle of attack the suction side boundary layer separates after the leading edge, at approximately 15% of the chord. A separated shear layer forms, which subsequently undergoes transition and reattaches shortly after the mid point of the chord as a turbulent boundary layer. At the flatback airfoil, the interaction of the boundary layer with the exposed bluntness at the trailing edge, results in a Von Kárman shedding at the wake. The length of the separation bubble was also found to be affected, albeit not to a significant extent. The turbulent fluctuations in the streamwise and cross-stream directions are, for the straight trailing edge, maximised at the mid-chord point due to the shear layer shedding, whereas for the blunt trailing edge an additional, larger, maximum exists downstream of the trailing edge, as a result of the Karman shedding.

When the serrated trailing edge is used, a non-uniform bluntness is created at the trailing edge, ranging from zero at the peak to a maximum value at the trough. This was found to create a highly complex and three-dimensional flow field. The tapering bluntness creates low pressure cores which are located downstream of the troughs, inside the serrations. These cores create an upstream and spanwise effect, most noticeable on the pressure side of the airfoil, according to which the streamlines bend in order to be entrained inside the troughs. As the flow enters the space between the serrations, it travels a small distance upstream, before entering in the wake from the location of the trough. This phenomenon was found to have a direct effect on the wake deficit shortly downstream of the trailing edge, which was found to be smaller downstream of the troughs than downstream of the peaks. This local re-energization of the wake has been also found in experimental results in a very similar flow configuration (Prigent et al., 2016). The streamwise and cross-stream fluctuations for the serrated trailing edge show a similar behaviour with the other

cases. A difference, though, is observed in the spanwise component, which now shows higher values on the suction side and a local maximum downstream of the trough. The latter are again a strong indication of the highly three dimensional nature of the flow-field which is created both upstream and downstream of the serrated trailing edge.

6.1.2 Frequency content of the flow fields

The inflectional profile of the separated shear layer leads to the development of a Kelvin-Helmholtz instability and the creation of two-dimensional structures elongated along the span of the airfoil. These structures then break-down and lead to a turbulent flow field which causes the separated layer to reattach. For the straight trailing edge case, the dominant frequency of the KH instability was found to be $f_2 = 7.4$, attenuating significantly downstream of the shear layer, whereas its subharmonic amplifies and becomes the dominant frequency in the wake. The frequency f_2 was found to be in very good agreement with previously observed results when normalized by the length-scale of the KH instabilities and the velocity at the edge of the boundary layer at the separation point, taking the value $f_2^* = 0.44$.

When the blunt trailing edge was introduced, a strong mode resulting from the truncated trailing edge was identified in the wake at $f_{bl,1} = 4.5$, which corresponds to Strouhal number $St = 0.17$ and which is well within the observed range of Strouhal values for Kárman shedding. The frequency content of the shear layer in this case, though, dramatically changed. Several probes were placed on the suction side of the airfoil, all of which identified a single dominant frequency: the shedding frequency $f_{bl,1}$, with the aforementioned natural frequency of the shear layer f_2 being significantly attenuated. This observations suggests a lock-in mechanism was in place for the flatback airfoil.

The presence of the serrated trailing edge lead to a mixture of the aforementioned behaviours. Both in the boundary layer and in the wake, the natural frequency of the shear layer and the frequency from the trailing edge shedding were observed.

More specifically, at their most pronounced point at $X/C = 0.53$, all three of the shear layer frequency, its subharmonic and the shedding frequency are present with comparable energy levels. Further downstream and in the wake only the latter two remain, while maintaining comparable levels of energy.

6.1.3 Spatial behaviour of the dominant modes

The application of the dynamic mode decomposition allowed the detailed study of the spatial structures beating at the most dominant frequencies in the flow field. The method was applied for the straight and blunt trailing edges on a XY-plane at the mid-span location. Although attempts were made to apply the method on various planes at the serrated trailing edge airfoil, we weren't able to derive conclusive results, due to the aforementioned significant three-dimensional effects of the flow field.

For the straight trailing edge the KH instability was clearly captured. The spatial structure of the mode revealed a cluster of vortical structures at the location of the roll-up of the separated shear layer. The sub-harmonic was also captured, albeit with a less clear spatial distribution.

In the flatback airfoil a very clear dominant mode was identified in the wake and the shear layer, which is another indication of the aforementioned lock-in between the wake and the shear layer. In an attempt to separate the effect of the wake on the results, the method was applied on a small window covering only the suction side of the airfoil. Again in this case though the dominant mode was found to oscillate at the wake shedding frequency and have an almost identical spatial structure with before. From the results of the DMD analysis and from the spectral content of the flow field it was postulated that the global instability, which results from the strong vortex shedding, has a direct upstream effect on the separated shear layer. The ratio between the shedding frequency, which assumes the role of an external forcing, and the natural frequency of the shear layer was found to be approximately 0.5. According to previous studies in perturbed free shear layers, when the ratio

between the two frequencies takes the aforementioned value, the response of the shear layer peaks at the frequency of the applied forcing. This observation provided the mechanism for the observed lock-in, in the case of the blunt trailing edge.

6.1.4 Resolvent analysis

A relatively new analysis method was applied to the same data as the dynamic mode decomposition. The resolvent analysis has the benefit of not being reliant on any approximation, its only assumption being that the mean flow-field is known. Then the non-linear part is treated as an external forcing applied on the linear dynamics of the Navier-Stokes equations. This analysis, when applied in the configurations studied in this thesis, revealed very important information regarding the nature of the separation bubble, and its frequency selection mechanism.

By applying harmonic modes of varying frequencies we were able to study the response of the flow field to its own inherent non-linear dynamics for the spectrum of applied frequencies. A band-pass like behaviour was indeed identified, with a range of frequencies, centred at the oscillating frequency of the shear layer, being significantly amplified. It must be pointed out that the peak frequency varied between the straight and blunt trailing edge airfoils, with the peak for the latter airfoil being located at the Kárman shedding frequency. This result can be expected since we already saw that the shear layer frequency locks-in with the shedding frequency when the truncated trailing edge is used. It is important though to realize that in the resolvent analysis the only known result is the time-averaged flow field, which allowed us to identify this important difference with the straight trailing edge, without any additional dynamic information. The observed lock-in was also found to have an important effect in the range of frequencies around the natural frequency of the unperturbed shear layer, which were attenuated by approximately an order of magnitude, a fact that indicates a reduction in the receptivity of the separation bubble for this range of frequencies, an important result with potential applications if the modification of the resonance behaviour of the airfoil is sought (in a wind

turbine for example).

Finally the power of the resolvent analysis as an estimation tool was also illustrated. The dominance of the first singular value in both cases allowed a low-order reconstruction of the spectra and RMS values of the flow field in a set of locations where the flow shows the most energetic response. This was achieved using only the time-averaged flow field and velocity data from 10 points, which were used to calibrate the weighting function.

6.1.5 Analysis of the attached boundary layer

In an attempt to mitigate the overwhelming effect of the separation bubble shedding on the flow field we applied an artificial forcing at the leading edge of the airfoil which prevented full separation of the boundary layer. Nevertheless, incipient separation was observed. The created inflectional profile of the boundary layer led to the formation of spanwise elongated structures which consequently broke down leading to a turbulent boundary layer. The spectrum of these structures at the area where they appeared to be forming was found to peak at $f = 9.0$, whereas further downstream it peaked at half of that frequency $f_{1/2} = 4.5$, suggesting that, despite the absence of a fully developed shear layer, a similar mechanism was in place, as in the unforced cases. The impact of the separation bubble was also aptly illustrated in the significantly modified values of the RMS and aerodynamic behaviour of the airfoil. The RMS values of both the streamwise and cross-stream components were found to be reduced by approximately 50%, whereas the lift-to-drag ratio increased by 20%.

The resolvent analysis revealed a peak of the spectrum at the frequency $f_{1/2}$, with the spatial structure of the corresponding modes being mostly located in the wake. This was in stark difference with the same result for the untripped airfoil, where the peak was at the shear layer frequency and the mode was predominantly located at the suction side of the airfoil. This result was found to be caused by a combination of the absence of the separation bubble and the effect of the optimization domain,

which due to the lack of significant dynamic behaviour on the airfoil's suction side, in combination with the larger size of the wake, led to more amplified responses when the flow was forced at the wake frequency $f_{1/2}$. The results for the blunt airfoil were as expected from the previous analysis, with the peak appearing at the shedding frequency. A notable difference was the much smoother curve of the spectrum (when compared with the highly irregular curve of the unforced cases) and the appearance of a clearly resonant behaviour which was absent when the separation bubble was in place. In both cases the effect of the attenuated shedding on the suction side of the airfoil appeared on the resolvent's spectrum as a localized "kink" at the corresponding frequency.

6.2 Suggestions for future studies

As previously mentioned, the three dimensional effects of the serrated trailing edge case made it impossible to apply the DMD and resolvent analysis methods in 2D planes, as it was done for the other two airfoil configurations. An interesting study would be to see what will these methods give when applied in the full 3D data. Such attempts were made in this study, but due to the high resolution of the grid, the resulting matrices where preclusively large. Nevertheless, if data are provided from LES simulations, which can lead to more manageable matrices, these methods could reveal the full dynamical behaviour of the flow field, both in the area of the separation bubble and in the area inside the serrations. As we saw there is a shedding originating from the troughs of the serrations, whose presence is also noticeable in the suction side of the airfoil. It would thus be an interesting study to see where exactly this shedding comes from, since the sides of the serrations can also have an effect due to their bluntness, and how it interacts with the incoming vortices from the separated shear layer.

Furthermore, an extension of the spectra estimation process can be studied to asses whether the inclusion of a larger number of modes can improve the accuracy.

As it was shown in chapter 4, when the first singular value is several orders of magnitude larger than the others, it can be used as an estimator for several points in the flow field. When the same method was applied in the tripped airfoil the estimations were not that accurate and they were not included in this work. A possible explanation is the fact that the difference between the first and second singular values was not as pronounced as in the untripped case. Thus, it could be argued on the basis of the analysis presented in chapter 4, that if the first two modes are used, instead of just the first, the accuracy would be highly improved.

Another topic of interest would be the resolvent analysis of three-dimensional modes. As it was shown, in order to arrive to the final equation for the resolvent matrix it was assumed that the variables in the equation (velocity, pressure and non-linear forcing) had a harmonic form $f'(x, y, t) = \hat{f}(x, y)e^{i\omega t}$ (i.e. the temporal Fourier transform was applied in the equation). A generalization of this method would be to assume that the variables have the form $f'(x, y, z, t) = \hat{f}(x, y)e^{i(\omega t+\beta z)}$, i.e. to apply the Fourier transform both in time and in the spanwise direction. This will effectively assume that the applied forcing has a spanwise undulation with a wavelength equal to $L_z = \frac{2\pi}{\beta}$. Previous similar studies, such as that by McKeon and Sharma (2010) in a turbulent pipe where the forcing was allowed to vary in the temporal, streamwise and azimuthal directions, have been proven able to reveal a much more detailed view of the flow field's constituent modes. It can thus be expected that if a similar approach is used for the airfoils studies of this thesis, we could get a clearer insight of the underlying 3D dynamics both in the separation bubble and in the wake.

Lastly, another future direction with potential application in the wind turbine industry, would be the study of the separation bubble in pitching motions with different trailing edges. It was demonstrated in the present work that there is a clear effect of the airfoil's trailing edge geometry on its dynamic behaviour. This dynamic behaviour is mostly dominated by the separation bubble with the latter being very sensitive to the angle of attack. It would be of great interest, in the

author's opinion, to apply the mode extraction methods presented here, while the dynamic characteristics of the separation bubble change and also to see whether these changes are somehow mitigated (or maybe aggravated) with a blunt or serrated trailing edge. It could for example be the case that the lock-in that is caused by the flatback airfoil adds more "inertia" to the separation bubble, making it more difficult to alter its shedding frequency and thus making it more stable and more controllable.

Bibliography

Åkervik, E., Ehrenstein, U., Gallaire, F., and Henningson, D. S. (2008). Global two-dimensional stability measures of the flat plate boundary-layer flow. *European Journal of Mechanics-B/Fluids*, 27(5):501–513.

Alam, M. and Sandham, N. (2000). Direct numerical simulation of short laminar separation bubbles with turbulent reattachment. *Journal of Fluid Mechanics*, 403:223–250.

Alizard, F., Cherubini, S., and Robinet, J. (2009). Sensitivity and optimal forcing response in separated boundary layer flows. *Physics of Fluids*, 21(6):064108.

Allen, T. and Riley, N. (1995). Absolute and convective instabilities in separation bubbles. *The Aeronautical Journal*, 99(990):439–449.

Amestoy, P., Duff, I., L'Excellent, J., and Koster, J. (2001). A fully asynchronous multifrontal solver using distributed dynamic scheduling. *SIAM Journal on Matrix Analysis and Applications*, 23(1):15–41.

Bagheri, S. (2012). Computational hydrodynamic stability and flow control based on spectral analysis of linear operators. *Archives of Computational Methods in Engineering*, 19(3):341–379.

Baj, P., Bruce, P., and Buxton, O. (2015). The triple decomposition of a fluctuating velocity field in a multiscale flow. *Physics of Fluids (1994-present)*, 27(7):075104.

Baker, J., Mayda, E., and Van Dam, C. (2006). Experimental analysis of thick blunt trailing-edge wind turbine airfoils. *Journal of Solar Energy Engineering*, 128(4):422–431.

Barkley, D. (2006). Linear analysis of the cylinder wake mean flow. *EPL (Europhysics Letters)*, 75(5):750.

Bearman, P. W. and Tombazis, N. (1993). The effects of three-dimensional imposed disturbances on bluff body near wake flows. *Journal of Wind Engineering and Industrial Aerodynamics*, 49(1-3):339–349.

Beneddine, S., Sipp, D., Arnault, A., Dandois, J., and Lesshafft, L. (2016). Conditions for validity of mean flow stability analysis. *Journal of Fluid Mechanics*, 798:485–504.

Beneddine, S., Yegavian, R., Sipp, D., and Leclaire, B. (2017). Unsteady flow dynamics reconstruction from mean flow and point sensors: an experimental study. *Journal of Fluid Mechanics*, 824:174201.

Berkooz, G., Holmes, P., and Lumley, J. L. (1993). The proper orthogonal decomposition in the analysis of turbulent flows. *Annual review of fluid mechanics*, 25(1):539–575.

Bouhadji, A. and Braza, M. (2003). Organised modes and shock–vortex interaction in unsteady viscous transonic flows around an aerofoil: Part i: Mach number effect. *Computers & fluids*, 32(9):1233–1260.

Bourdet, S., Bouhadji, A., Braza, M., and Thiele, F. (2003). Direct numerical simulation of the three-dimensional transition to turbulence in the transonic flow around a wing. *Flow, turbulence and combustion*, 71(1):203–220.

Boutilier, M. and Yarusevych, S. (2012). Separated shear layer transiton over an airfoil at a low Reynolds number. *Physics of Fluids (1994-present)*, 24:084105.

Butler, K. M. and Farrell, B. F. (1992). Three-dimensional optimal perturbations in viscous shear flow. *Physics of Fluids A: Fluid Dynamics*, 4(8):1637–1650.

Cai, J., Chng, T. L., and Tsai, H. M. (2008). On vortical flows shedding from a bluff body with a wavy trailing edge. *Physics of Fluids (1994-present)*, 20(6):064102.

Chen, X. and Agarwal, R. (2012). Optimization of flatback airfoils for wind-turbine blades using a genetic algorithm. *Journal of Aircraft*, 49(2):622–629.

Chow, R. and van Dam, C. (2013). Computational investigations of blunt trailing-edge and twist modifications to the inboard region of the NREL 5MW rotor. *Wind Energy*, 16:445–458.

Desquesnes, G., Terracol, M., and Sagaut, P. (2007). Numerical investigation of the tone noise mechanism over laminar airfoils. *Journal of Fluid Mechanics*, 591:155–182.

Donzis, D., Yeung, P., and Sreenivasan, K. (2008). Dissipation and enstrophy in isotropic turbulence: Resolution effects and scaling in direct numerical simulations. *Physics of Fluids*, 20(4):045108.

Dovgal, A., Kozlov, V., and Michalke, A. (1994). Laminar boundary layer separation: instability and associated phenomena. *Progress in Aerospace Sciences*, 30(1):61–94.

Drela, M. and Youngren, H. (2001). Xfoil 6.94 user guide.

Dunne, R. and McKeon, B. (2015). Dynamic stall on a pitching and surging airfoil. *Experiments in Fluids*, 56(8):1–15.

Ferziger, J. H. and Peric, M. (1996). *Computational Methods for Fluid Dynamics*. Springer-Verlag Berlin Heidelberg.

Gai, S. and Sharma, S. (1981). Experiments on the reduction of base drag of a blunt trailing edge aerofoil in subsonic flow. *Aeronautical Journal*, 85(844):206–210.

Garnaud, X., Lesshafft, L., Schmid, P., and Huerre, P. (2013). The preferred mode of incompressible jets: linear frequency response analysis. *Journal of Fluid Mechanics*, 716:189–202.

Gaster, M. (1963). *On the stability of parallel flows and the behaviour of separation bubbles*. PhD thesis, Queen Mary, University of London.

Gaster, M. (1968). Growth of disturbances in both space and time. *The Physics of Fluids*, 11(4):723–727.

Gómez, F., Blackburn, H., Rudman, M., Sharma, A., and McKeon, B. (2016a). A reduced-order model of three-dimensional unsteady flow in a cavity based on the resolvent operator. *Journal of Fluid Mechanics*, 798.

Gómez, F., Sharma, A., and Blackburn, H. (2016b). Estimation of unsteady aerodynamic forces using pointwise velocity data. *Journal of Fluid Mechanics*, 804.

Greenblatt, D. and Wygnanski, I. (2000). The control of flow separation by periodic excitation. *Prog. Aerosp. Sci.*, 36:487–545.

Hammond, D. and Redekopp, L. (1998). Local and global instability properties of separation bubbles. *European Journal of Mechanics-B/Fluids*, 17(2):145–164.

Hecht, F. (2012). New development in freefem++. *J. Numer. Math.*, 20(3-4):251–265.

Ho, C.-M. and Huang, L.-S. (1982). Subharmonics and vortex merging in mixing layers. *Journal of Fluid Mechanics*, 119:443–473.

Ho, C.-M. and Huerre, P. (1984). Perturbed free shear layers. *Annual Review of Fluid Mechanics*, 16(1):365–422.

Hoarau, Y., BRAZA, M., Ventikos, Y., Faghani, D., and Tzabiras, G. (2003a). Organized modes and the three-dimensional transition to turbulence in the incompressible flow around a naca0012 wing. *Journal of Fluid Mechanics*, 496:63–72.

Hoarau, Y., Faghani, D., Braza, M., Perrin, R., Anne-Archard, D., and Ruiz, D. (2003b). Direct numerical simulation of the three-dimensional transition to turbulence in the incompressible flow around a wing. *Flow, turbulence and combustion*, 71(1):119–132.

Horton, H. (1968). *Laminar separation bubbles in two and three dimensional incompressible flow*. PhD thesis, Queen Mary, University of London.

Hosseini, S., Vinuesa, R., Schlatter, P., Hanifi, A., and Henningson, D. (2016). Direct numerical simulation of the flow around a wing section at moderate reynolds number. *International Journal of Heat and Fluid Flow*, 61:117–128.

Huang, L.-S. and Ho, C.-M. (1990). Small scale transition in a plane mixing layer. *Journal of Fluid Mechanics*, 210:475–500.

Huerre, P. and Monkewitz, P. (1985). Absolute and convective instabilities in free shear layers. *Journal of Fluid Mechanics*, 159:151–168.

Huerre, P. and Monkewitz, P. (1990). Local and global instabilities in spatially developing flows. *Annual review of fluid mechanics*, 22(1):473–537.

Issa, R. (1986). Solution of the implicitly discretised fluid flow equations by operator-splitting. *Journal of computational physics*, 62(1):40–65.

Jeong, J. and Hussain, F. (1995). On the identification of a vortex. *Journal of Fluid Mechanics*, 285:69–94.

Jolliffe, I. (2002). *Principal component analysis*. Wiley Online Library.

Jones, L. (2008). *Numerical studies of the flow around an airfoil at low Reynolds number*. PhD thesis, University of Southampton.

Jones, L. and Sandberg, R. (2012). Acoustic and hydrodynamic analysis of the flow around an aerofoil with trailing-edge serrations. *Journal of Fluid Mechanics*, 706:295–322.

Jones, L., Sandberg, R., and Sandham, N. (2008). Direct numerical simulations of forced and unforced separation bubbles on an airfoil at incidence. *Journal of Fluid Mechanics*, 602:175–207.

Jones, L., Sandberg, R., and Sandham, N. (2010). Stability and receptivity characteristics of a laminar separation bubble on an aerofoil. *Journal of Fluid Mechanics*, 648:257–296.

Jovanović, M., Schmid, P., and Nichols, J. (2014). Sparsity-promoting dynamic mode decomposition. *Physics of Fluids (1994-present)*, 26(2):024103.

Kato, T. (2013). *Perturbation theory for linear operators*, volume 132. Springer Science & Business Media.

Kim, J. and Moin, P. (1985). Application of a fractional-step method to incompressible navier-stokes equations. *Journal of computational physics*, 59(2):308–323.

Kitsios, V., Kotapati, R., Mittal, R., Ooi, A., Soria, J., and You, D. (2006). Numerical simulation of lift enhancement on a naca 0015 airfoil using znmf jets. In *Proceedings of the Summer Program*, page 457.

Kitsios, V., Rodríguez, D., Theofilis, V., Ooi, A., and Soria, J. (2008). Biglobal instability analysis of turbulent flow over an airfoil at an angle of attack. *AIAA Paper*, 4384:2008.

Kotapati, R., Mittal, R., Marxen, O., Ham, F., You, D., and LN, C. I. (2010). Nonlinear dynamics and synthetic-jet-based control of a canonical separated flow. *Journal of Fluid Mechanics*, 654:65–97.

Krentel, D. and Nitsche, W. (2013). Investigation of the near and far wake of a bluff airfoil model with trailing edge modifications using time-resolved particle image velocimetry. *Experiments in fluids*, 54(7):1–16.

Lehmkuhl, O., Rodríguez, I., Baez, A., Oliva, A., and Pérez-Segarra, C. (2013a). On the large-eddy simulations for the flow around aerodynamic profiles using unstructured grids. *Computers & Fluids*, 84:176–189.

Lehmkuhl, O., Rodríguez, I., Baez, A., Oliva, A., and Pérez-Segarra, C. (2013b). On the large-eddy simulations for the flow around aerodynamic profiles using unstructured grids. *Computers & Fluids*, 84:176–189.

Lehoucq, R., Sorensen, D., and Yang, C. (1998). *ARPACK users' guide: solution of large-scale eigenvalue problems with implicitly restarted Arnoldi methods*. SIAM.

Lissaman, P. (1983). Low-Reynolds-number airfoils. *Annual Review of Fluid Mechanics*, 15(1):223–239.

Lu, L. and Papadakis, G. (2014). An iterative method for the computation of the response of linearised navier–stokes equations to harmonic forcing and application to forced cylinder wakes. *International Journal for Numerical Methods in Fluids*, 74(11):794–817.

Lumley, J. (1970). *Stochastic tools in turbulence*. Elsevier, 1st edition.

Mariappan, S., Gardner, A., Richter, K., and Raffel, M. (2014). Analysis of dynamic stall using dynamic mode decomposition technique. *AIAA journal*, 52(11):2427–2439.

Marxen, O. and Henningson, D. (2011). The effect of small-amplitude convective disturbances on the size and bursting of a laminar separation bubble. *Journal of Fluid Mechanics*, 671:1–33.

Marxen, O., Kotapati, R., Mittal, R., and Zaki, T. (2015). Stability analysis of separated flows subject to control by zero-net-mass-flux jet. *Physics of Fluids*, 27(2):024107.

Marxen, O., Lang, M., and Rist, U. (2013). Vortex formation and vortex breakup in a laminar separatiomn bubble. *Journal of Fluid Mechanics*, 728:58–90.

Marxen, O. and Rist, U. (2010). Mean flow deformation in a laminar separation bubble: separation and stability characteristics. *Journal of Fluid Mechanics*, 660:37–54.

McKeon, B. and Sharma, A. (2010). A critical-layer framework for turbulent pipe flow. *Journal of Fluid Mechanics*, 658:336–382.

Mittal, S. (2008). Global linear stability analysis of time-averaged flows. *International journal for numerical methods in fluids*, 58(1):111–118.

Moarref, R., Sharma, A. S., Tropp, J. A., and McKeon, B. J. (2013). Model-based scaling of the streamwise energy density in high-reynolds-number turbulent channels. *Journal of Fluid Mechanics*, 734:275–316.

Moin, P. and Mahesh, K. (1998). Direct numerical simulation: a tool in turbulence research. *Annual review of fluid mechanics*, 30(1):539–578.

Muzaferija, S. (1994). *Adaptive finite volume method for flow prediction using unstructured meshes and multigrid approach*. PhD thesis, University of London UK.

Nedić, J. and Vassilicos, J. (2015). Vortex shedding and aerodynamic performance of airfoil with multiscale trailing-edge modifications. *AIAA Journal*, 53(11):3240–3250.

O'Meara, M. and Mueller, T. (1987). Laminar separation bubble characteristics on an airfoil at low Reynolds numbers. *AIAA Journal*, 25(8):1033–1041.

Park, J., Witherden, F., and Vincent, P. (2017). High-order implicit large-eddy simulations of flow over a naca0021 aerofoil. *AIAA Journal*.

Patankar, S. (1980). *Numerical heat transfer and fluid flow*. CRC press.

Pope, S. B. (2001). *Turbulent flows*. Cambridge University Press.

Portela, F. (2017). *Turbulence Cascade in an Inhomogeneous Turbulent Flow*. PhD thesis, Imperial College London.

Postl, D., Balzer, W., and Fasel, H. (2011). Control of laminar separation using pulsed vortex generator jets: direct numerical simulations. *Journal of Fluid Mechanics*, 676:81–109.

Prigent, S. L., Buxton, O., and Bruce, P. J. (2016). Experimental investigation of the wake of a lifting wing with cut-in sinusoidal trailing edges. In *54th AIAA Aerospace Sciences Meeting*, page 0852.

Pröbsting, S. and Yarusevych, S. (2015). Laminar separation bubble development on an airfoil emitting tonal noise. *Journal of Fluid Mechanics*, 780:167–191.

Rayleigh, L. (1879). On the stability, or instability, of certain fluid motions. *Proceedings of the London Mathematical Society*, 1(1):57–72.

Rhie, C. and Chow, W. L. (1983). Numerical study of the turbulent flow past an airfoil with trailing edge separation. *AIAA journal*, 21(11):1525–1532.

Rist, U. and Augustin, K. (2006). Control of laminar separation bubbles using instability waves. *AIAA Journal*, 44(10):2217–2223.

Rist, U. and Maucher, U. (2002). Investigations of time-growing instabilities in laminar separation bubbles. *European Journal of Mechanics-B/Fluids*, 21(5):495–509.

Rodríguez, D., Gennaro, E., and Juniper, M. (2013). The two classes of primary modal instability in laminar separation bubbles. *Journal of Fluid Mechanics*, 734.

Rodríguez, D. and Theofilis, V. (2009). Massively parallel solution of the biglobal eigenvalue problem using dense linear algebra. *AIAA Journal*, 47(10):2449.

Rodriguez, D. and Theofilis, V. (2010). Structural changes of laminar separation bubbles induced by global linear instability. *Journal of Fluid Mechanics*, 655:280–305.

Rodriguez, O. (1991). Base drag reduction by control of the three-dimensional unsteady vortical structures. *Experiments in Fluids*, 11(4):218–226.

Rowley, C., Mezić, I., Bagheri, S., Schlatter, P., and Henningson, D. (2009). Spectral analysis of nonlinear flows. *Journal of Fluid Mechanics*, 641:115–127.

Sandberg, R. and Jones, L. (2011). Direct numerical simulations of low reynolds number flow over airfoils with trailing-edge serrations. *Journal of Sound and Vibration*, 330:3818–3831.

Sartor, F., Mettot, C., and Sipp, D. (2014). Stability, receptivity, and sensitivity analyses of buffeting transonic flow over a profile. *AIAA Journal*, 53(7):1980–1993.

Schlatter, P. and Örlü, R. (2012). Turbulent boundary layers at moderate reynolds numbers: inflow length and tripping effects. *Journal of Fluid Mechanics*, 710:5–34.

Schmid, P. (2010). Dynamic mode decomposition of numerical and experimental data. *Journal of Fluid Mechanics*, 656:5–28.

Schmid, P. and Brandt, L. (2014). Analysis of fluid systems: Stability, receptivity, sensitivity. lecture notes from the flow-nordita summer school on advanced instability methods for complex flows, stockholm, sweden, 2013. *Applied Mechanics Reviews*, 66(2):024803.

Schmid, P. and Sipp, D. (2016). Linear control of oscillator and amplifier flows. *Physical Review Fluids*, 1(4):040501.

Schmid, P. J., Li, L., Juniper, M., and Pust, O. (2011). Applications of the dynamic mode decomposition. *Theoretical and Computational Fluid Dynamics*, 25(1-4):249–259.

Shan, H., Jiang, L., and Liu, C. (2005a). Direct numerical simulation of flow separation around a naca 0012 airfoil. *Computers & Fluids*, 34(9):1096–1114.

Shan, H., Jiang, L., and Liu, C. (2005b). Direct numerical simulation of flow separation around a naca 0012 airfoil. *Computers & Fluids*, 34(9):1096–1114.

Sharma, A. S., Mezić, I., and McKeon, B. (2016). Correspondence between koopman mode decomposition, resolvent mode decomposition, and invariant solutions of the navier-stokes equations. *Physical Review Fluids*, 1(3):032402.

Sipp, D. and Lebedev, A. (2007). Global stability of base and mean flows: a general approach and its applications to cylinder and open cavity flows. *Journal of Fluid Mechanics*, 593:333–358.

Sipp, D. and Marquet, O. (2013). Characterization of noise amplifiers with global singular modes: the case of the leading-edge flat-plate boundary layer. *Theoretical and Computational Fluid Dynamics*, 27(5):617.

Sipp, D., Marquet, O., Meliga, P., and Barbagallo, A. (2010). Dynamics and control of global instabilities in open-flows: a linearized approach. *Applied Mechanics Reviews*, 63(3):030801.

Sirovich, L. (1987). Turbulence and the dynamics of coherent structures. i. coherent structures. *Quarterly of applied mathematics*, 45(3):561–571.

Smith, H. and Schaefer, R. (1950). Aerodynamic characteristics at Reynolds numbers of $3.0 \cdot 10^6$ and $6.0 \cdot 10^6$ of three airfoil sections formed by cutting off various amounts from the rear portion of the naca 0012 airfoil section. NACA Technical Note TN 2074, NACA.

Spalart, P. and Strelets, M. (2000). Mechanisms of transition and heat transfer in a separation bubble. *Journal of Fluid Mechanics*, 403:329–349.

Standish, K. and Van Dam, C. (2003). Aerodynamic analysis of blunt trailing edge airfoils. *Journal of Solar Energy Engineering*, 125(4):479–487.

Strykowski, P. and Niccum, D. (1992). The influence of velocity and density ratio on the dynamics of spatially developing mixing layers. *Physics of Fluids A: Fluid Dynamics*, 4(4):770–781.

Tam, C. K. and Ju, H. (2006). Numerical simulation of the generation of airfoil tones at a moderate reynolds number. *AIAA Paper*, 2502:2006.

Tanner, M. (1970). A method for reducing the base drag of wings with blunt trailing edge. Technical report, DTIC Document.

Tombazis, N. (1993). *Effects of three-dimensional disturbances on bluff body near wakes*. PhD thesis, University of London Library.

Tombazis, N. and Bearman, P. (1997). A study of three-dimensional aspects of vortex shedding from a bluff body with a mild geometric disturbance. *Journal of Fluid Mechanics*, 330(1):85O112.

Trefethen, L. (1991). Pseudospectra of matrices. *Numerical analysis*, 91:234–266.

Versteeg, H. and Malalasekera, W. (2007). *An introduction to computational fluid dynamics: the finite volume method*. Pearson Education.

Wan, Z., Zhou, L., Wang, B.-B., and Sun, D. (2015). Dynamic mode decomposition of forced spatially developed transitional jets. *European Journal of Mechanics-B/Fluids*, 51:16–26.

Williamson, C. (1996). Vortex dynamics in the cylinder wake. *Annual review of fluid mechanics*, 28:477–539.

Xu, H., Shen, W., Zhu, W., Yang, H., and Liu, C. (2014). Aerodynamic analysis of trailing edge enlarged wind turbine airfoils. In *Journal of Physics: Conference Series*, volume 524(1).

Yarusevych, S., Sullivan, P., and Kawall, J. (2006). Coherent structures in an airfoil booundary layer and wake at low Reynolds numbers. *Physics of Fluids (1994-present)*, 18:044101.

Yarusevych, S., Sullivan, P., and Kawall, J. (2009). On vortex shedding from an airfoil in low-Reynolds-number flows. *Journal of Fluid Mechanics*, 632:245–271.

You, D. and Moin, P. (2006). Large-eddy simulation of flow separation over an airfoil with synthetic jet control. *Center for Turbulence Research Annual Research Briefs*, pages 337–346.

Zhang, W. and Samtaney, R. (2015a). A direct numerical simulation investigation of the synthetic jet frequency effects on separation control of low-re flow past an airfoil. *Physics of Fluids*, 27(5):055101.

Zhang, W. and Samtaney, R. (2015b). A direct numerical simulation investigation of the synthetic jet frequency effects on separation control of low-re flow past an airfoil. *Physics of Fluids (1994-present)*, 27(5):055101.

Zhang, W. and Samtaney, R. (2016a). Assessment of spanwise domain size effect on the transitional flow past an airfoil. *Computers & Fluids*, 124:39–53.

Zhang, W. and Samtaney, R. (2016b). Biglobal linear stability analysis on low-re flow past an airfoil at high angle of attack. *Physics of Fluids*, 28(4):044105.